Torbjørn Hergum

3D ultrasound for quantitative echocardiography

Thesis for the degree of philosophiae doctor

Trondheim, June 2009

Norwegian University of Science and Technology
Faculty of Medicine
Department of Circulation and Medical Imaging

NTNU

Norwegian University of
Science and Technology

NTNU
Norwegian University of Science and Technology

Thesis for the degree of Philosophiae Doctor

Faculty of Medicine
Department of Circulation and Medical Imaging

ISBN 978-82-471-1656-2 (printed version)
ISBN 978-82-471-1658-6 (electronic version)
ISSN 1503-8181

Doctoral theses at NTNU, 2009:135

Printed by Tapir Uttrykk

Klaffelekkasjer i hjertet målt med tredimensjonal ultralyd

I hjertet er det fire klaffer som sørger for at blodet strømmer den riktige veien gjennom hjertet og ut i kroppen. Hvis disse klaffene ikke er helt tette, vil en del av blodet klemmes tilbake gjennom hullet slik at kroppen får for lite blod. Dermed må hjertet pumpe hardere for at kroppen skal få dekt oksygenbehovet. Hvis lekkasjen er stor og ikke blir behandlet i tide vil hjertemuskelen etter hvert svekkes på grunn av at den hele tiden er overarbeidet, og hjertepumpa vil til slutt stoppe.

Vi har derfor utviklet en ny tredimensjonal ultralydmetode for å måle størrelsen på hullet i utette hjerteklaffer, og vi kan også måle hvor mye blod som strømmer tilbake feil vei. Metoden benytter seg av Doppler-prinsippet til å måle farten til blodet. Ultralydsignalet som sendes inn i kroppen vil reflekteres med en litt endret frekvens avhengig av om det treffer blod som beveger seg eller vev som står stille, og denne endringen i frekvens kan vi måle. I tillegg utnytter vi fenomener en ser i væskestrøm som passerer gjennom en åpning. I det smaleste området i væskestrømmen nedenfor åpningen, kalt vena contracta, strømmer alt blodet med samme fart og det egner seg godt til måling med ultralyd Doppler. Størrelsen på vena contracta samsvarer godt med størrelsen på lekkasjen.

Den nye metoden har først blitt testet med simuleringer i en datamaskin. Deretter har vi klipt hull i hjerteklaffer fra en gris og studert dem i et kunstig hjerte i laboratoriet. Til slutt har vi sammenlignet målingene våre med magnetisk-resonans-avbildning i 27 pasienter med varierende lekkasjegrad. For mellomstore og store lekkasjer fungerer vår nye metode fint, men de små lekkasjene er vanskelig å måle helt riktig. Dette er imidlertid ikke så viktig, siden disse pasientene enkelt lukes ut med standard farge-Doppler avbildning.

I tillegg har vi utviklet nye simuleringsmetoder for 3D ultralyd, samt at vi har funnet en ny metode til fjerning av artefakter som stammer fra parallel stråleforming, både for vanlig avbildning og Doppler-metoder. Dette gjør det mulig å kombinere høy bildekvalitet ved høyere bilderate enn før. Siden god bildekvalitet er en avgjørende faktor ved all medisinsk avbildning vil dette gjøre det lettere å stille riktig diagnose.

Torbjørn Hergum
Institutt for Sirkulasjon og Bildediagnostikk, NTNU
Hovedveileder: Prof. Hans Torp
Biveileder: Prof. Knut Matre
Finansieringskilde: Samarbeidsorganet mellom Helse Midt-Norge RHF og NTNU

Ovennevnte avhandling er funnet verdig til å forsvares offentlig for graden Philosophiae Doctor (PhD) i medisinsk teknologi. Disputas finner sted i Seminarrommet i 1902-bygget, fredag 16. oktober kl. 12:15.

Abstract

Medical ultrasound imaging is widely used to diagnose cardiac diseases. The recent availability of real time 3D ultrasound poses several interesting challenges and opportunities, and the work of this thesis is devoted to both challenges and opportunities.

One of the key benefits of ultrasound imaging is that its images are real time. This has been challenged with the recent introduction of 3D images, where the number of ultrasound beams is squared compared to traditional 2D images. One common way to alleviate this is by receiving several closely spaced ultrasound beams from each pulse transmission, which increases acquisition speed but affects the image quality. Specifically, B-mode images are irregularly sampled and lose spatial shift invariance while a bias in the Doppler velocity estimates causes a discontinuity in the velocity estimates in color flow images. We have found that these artifacts can be reduced significantly by interpolation of the beamformed data from overlapping beams, with the limitation of requiring at least twice the number of beamformers.

We have also found that valvular regurgitation is one of the cardiac diseases that can benefit greatly from quantification of severity using 3D ultrasound. We have devised a modality that uses high pulse repetition frequency 3D Doppler to isolate the backscattered signal power from the vena contracta of a regurgitant jet. This measure is calibrated with a narrow reference beam inside the jet to estimate the cross-sectional area of the vena contracta. We have validated this method with computer simulations, with an in vitro study and finally in vivo with 27 patients who had mitral regurgitation. We found that the cross-sectional area and regurgitant volume of the vena contracta could be quantified without bias as long as the orifice was sufficiently large for a calibration beam to fit inside it. The severity of smaller regurgitations will be overestimated, but this does not pose a clinical problem, as these patients can easily be identified by standard 2D Doppler examination and do not typically need further quantification.

Finally, we have developed a new, fast 3D ultrasound simulation method that can incorporate anisotropic scattering from cardiac muscle cells. This approach is three orders of magnitude faster than the most commonly used simulation methods, making it well suited for the simulation of dynamic 3D images for development and testing of quantitative diagnostic methods such as 3D speckle tracking and volumetric measurements.

Preface

This thesis has been submitted in partial fulfillment of the requirements for the degree *Philosophiae Doctor* (PhD) at the Faculty of Medicine of the Norwegian University of Science and Technology (NTNU). The research was funded by the *Liaison Committee between the Central Norway Regional Health Authority and the Norwegian University of Science and Technology*, and was carried out under the supervision of Professor Hans Torp in the Department of Circulation and Medical Imaging, NTNU and co-supervised by Professor Knut Matre at the Institute of Medicine, University of Bergen.

Acknowledgments

First of all, I want to express my gratitude to Hans, for introducing me to the world of medical ultrasound, and for convincing me to pursue a PhD degree. (I am still waiting for that Nobel Prize you promised me.) This thesis would never have come to be without you sharing your enthusiasm and abundance of ideas with me. Secondly, my gratitude goes to Knut, for letting me come to your lab for a year when I needed to conduct some in vitro validation of my work as well as get within reach of a particular girl from Os. Thank you for numerous discussions, for sharing your ample experience with in vitro studies, and for allowing me to rebuild your heart model to my liking.

Furthermore, I would like to thank all the co-authors who contributed to the papers included in my thesis for sharing your knowledge and time and making this work possible. Also, I would like to thank all my good colleagues at the department for discussions both on and off-topic and for making the work here enjoyable. I would particularly like to mention Tore for helping me deal with synthetic beamforming and photography, Jonas for the fun of slicing and dicing hearts, Thomas and Bjørn Olav for enthusiastically implementing our emerging ideas into clinical trials, Svein Erik for bird-facts and bird-feasts, Lasse for playing in the lab and for being Hans when Hans was not there, Svein Arne for exciting river canoeing and lots of discussions, which oddly resulted in no common papers, Marco for being an entertaining office mate, and Kjell for your encouraging enthusiasm and technical creativity. I have also enjoyed our excellent collaboration with GE Vingmed, in particular Vidar, Kjetil and Tor Arne, who appeared to never tire from my questions, and Svein, for invaluable computer support, great hiking and numerous free lunches together with Ditlef, Rune and Olve from the late Bergen branch.

Saving the best for last, I want to thank my wonderful family, in particular my fabulous wife Åshild, for your love and encouragement.

Contents

Introduction

Ultrasound is a popular medical imaging modality. It is relatively cheap, highly available, examinations can be performed bedside, and no negative biological effects have been reported as long as the guidelines are followed [1]. Furthermore it provides the user with imaging and quantitative data from soft tissue and blood flow. Finally, ultrasound imaging is the only non-invasive medical imaging modality that can acquire true real-time images.

With the recent introduction of commercially available 3D ultrasound scanners, the ability of ultrasound to deliver real time imaging has been challenged due to the large amount of data that needs to be acquired for each volume, and it is common to use data from several heart cycles to obtain good quality images [2]. This is particularly true when combined with color flow imaging. To speed up the acquisition of ultrasound data it is common to use parallel receive beamforming [3, 4]. Typically, this parallel receive beamforming will introduce artifacts in the images that should be compensated for [5–7].

To be able to compensate for these artifacts it is important to understand their underlying cause. Being able to simulate the ultrasound imaging process is an invaluable tool in this regard, and there are numerous computer software packages available - from the very computationally demanding, non-linear simulations tools like *Abersim* [8] through the linear, industry standard *Field II* [9, 10] to software solutions like *Cole* [11], where additional approximations are made to speed up the execution time. Apart from providing insight into the physics of ultrasonic imaging, another important use of simulations is to create synthetic data sets to facilitate and validate novel quantitative methods like 3D speckle tracking [12, 13].

Ultrasound is already used extensively to quantify the various diseases of the heart. As an example, the global function of the heart is well quantified by measuring the ejection fraction with the modified Simpson's rule, using two orthogonal B-mode images from end systole and end diastole [14]. Excursion of the mitral annulus is another parameter for global function that is readily measured with M-mode [15]. Diagnosing cardiomyopathies can also be done using M-mode, by measuring the dimensions of the ventricle and the wall thickness [14], while regional function can be quantified with tissue Doppler techniques like strain and strain rate [16]. The severity of aortic stenosis can be quantified well by measuring the opening area of the valve using the continuity equation, and the pressure drop across the stenotic valve can be found from the simplified Bernoulli's equation relating jet velocity measured with CW Doppler

with the pressure gradient [17, 18].

The availability of 3D data sets provides an opportunity for better quantitative evaluations of cardiac diseases. For instance, it is no longer necessary to estimate the left ventricular volume from 2D images and several assumptions regarding the geometry of the ventricle [14], as the whole ventricle can now be imaged and the volume quantified in real time [19]. It is also possible to quantify volume blood flow through large openings such as the mitral annulus by integrating the velocity found from 3D color flow over a surface covering the opening [20, 21].

Severe mitral regurgitation is a life-threatening condition [22]. The only established treatment for the condition is surgery, and the best short- and long-term outcomes are obtained if surgery is performed on asymptomatic patients [22, 23]. This means that accurate assessment of the disease is crucial for timing the intervention before the heart remodels and the outcome gets worse.

In addition to determining the severity of valvular regurgitation, echocardiography may discover the underlying cause of the problem. This is important to know before surgery, as organic valvular disease, caused by conditions such as ruptured chordae, papillary muscles or flailed leaflets, requires different surgical procedures from functional valvular regurgitations caused by abnormal ventricle geometry [24].

Real time 3D echocardiography is a good tool for evaluating mitral valve diseases such as stenosis and prolapse [25], but the resolution is not yet good enough for direct planimetry of the regurgitant orifice. Instead of planimetry of the orifice itself, it is possible to measure the width or area of the vena contracta, which is the narrowest part of the jet just downstream from the orifice itself, using 2D or 3D color flow [26]. The strength of this method is its simplicity, because it requires just one measurement. However, it does not handle multiple jets, it is dependent on gain settings, and it is dependent on the poor resolution of cardiac ultrasound at typical imaging depths of 8-10 cm [27]. This results in small values in the measurement, where a small error gives a large fractional error. Also, the Nyquist velocity is typically too low to separate the high-speed core of the jet from the entrained fluid around it. It has been shown that the maximum vena contracta width, which is listed in the current guidelines as a good measure of the mitral regurgitation severity, is significantly different when measured with 3D instead of 2D color flow [28, 29], which indicates that mitral regurgitation should be evaluated in 3D.

Another suggestion for quantification of mitral regurgitation is the proximal isovelocity surface area method (PISA) [30], which seems to work well in some studies [31]. It does, however, underestimate functional mitral regurgitation [32] and overestimates the regurgitant volume for patients with prolapse showing non-optimal flow convergence regions [33], and it assumes circular orifices, while the majority of patients have non-circular orifices as imaged by 3D color flow [28]. An extension of PISA that allows the system to handle hemielliptic instead of hemispheric inflow regions avoids some of these problems, but it involves complicated measurements in several image planes [28, 34, 35].

1.1 Aims of study

The overall aim of this thesis is to enable better quantification of cardiac function. Many of the quantitative tools available to assess cardiac function are based on ultrasound images, be it B-mode tissue images or color flow images of blood flow. To extract quantitative information from these images, such as by speckle tracking or volume measurements, *image quality* is a key to success. It is also necessary to have an adequate frame rate to capture the dynamics of the heart. Unfortunately there is an inherent trade-off between image quality and frame rate, as the time needed to acquire one beam is limited by the speed of sound, and good image quality requires narrow, densely spaced ultrasound beams. The first aim of this study was therefore to minimize this trade-off, by using parallel beams to increase the frame rate without degrading image quality.

The recent availability of 3D cardiac ultrasound imaging has started the development of a whole new range of quantitative methods applicable to 3D data sets, be it speckle tracking to obtain torsion and twist values or volumetric measurements of the chambers of the heart. The availability of dynamic, 3D simulated ultrasound images is important for testing and validation of these new quantitative tools. To be useful in a practical sense, the simulations should be as realistic as possible but still fast enough for large, dynamic data sets and iterative work. These parameters form the core of the second aim of this study, which was to create such a simulation framework.

Clinicians have several echocardiographic methods available to quantify the severity of cardiac diseases. But there is currently no quantitative method for valvular regurgitations that has managed to win common clinical acceptance. For example, the failure to assess the severity of mitral regurgitation is crucial, as delaying the decision for surgery can have adverse effects on the outcome. The third aim was thus to develop methods for the quantification of valvular regurgitation.

To summarize: the **three aims** of this work was to

- Improve the frame rate of tissue and color flow images without reducing image quality,
- develop methods for fast simulations of dynamic, realistic 3D ultrasound images, and
- use 3D Doppler ultrasound to quantify valvular regurgitation.

1.2 Summary of contributions

Good image quality with high frame rate

The heart moves quickly, and to resolve all movement a high frame rate is necessary. Parallel beams is commonly used to increase the frame rate of ultrasound images by receiving several closely spaced beams from each transmitted pulse. Unfortunately, the image quality is reduced with the use of parallel beams, due to several artifacts caused by misalignment of the transmit- and receive-beams. We have analyzed these

artifacts and have separated them into three effects: *warping*, *skewing* and *Doppler bias*.

Warping is the effect that the two-way beam will not necessarily follow a straight line, as the transmitted beam will "pull" the receive-beam closer, particularly near the focal point. This makes the pulse-echo beams follow curved lines, while the instrument assumes that they are straight, which results in uneven sampling. *Skewing* is distortion of the beam, also caused by misalignment of transmit- and receive-beams. Think of it by an example: the side-lobes of the receive beam closest to the center of the transmit beam will be weighted higher than the sidelobes on the other side, and in this way it makes the two-way beam skewed. *Doppler bias* is caused by the curved wavefronts of focused beams, which gives a different Doppler-shift depending on where along the curvature the receive beam samples the sound field. Since this bias shows odd symmetry about the center of the transmitted beam the receive beams on the edges of the group will experience the same bias, but with opposite signs, which gives an abrupt change in the velocity estimate across neighboring receive beams from different transmit events.

The net result of these three effects is that the images, be it B-mode or color flow or other imaging modalities, are not spatially shift invariant. This means that a slight shift of the transducer does not just cause a slight shift in the image, but the image changes as well.

Since all of these problems are caused by misalignment of the transmitted and received beams we have proposed a solution which consists of interpolating the transmitted beams to generate *Synthetic Transmit Beams* (STB) so that each received beam can align with a transmit beam - synthetic or real - which ideally will remove all artifacts caused by misalignment.

The interpolation can be performed before or after beamforming, but currently it is most practical to perform it after beamforming by interpolating between overlapping receive beams from different transmit events. Linear interpolation is most practical since it requires only two overlapping receive beams. This minimizes problems with motion artifacts and needs least additional hardware.

For Doppler modalities we have found that STB interpolation works well in combination with interleaving, which minimizes the time lag between the overlapping receive beams. Across interleaving groups or in the elevation direction of 3D scans this will in general not work due to the excessive time delay. In these cases the STB interpolation should be performed on the auto-correlation function instead of on IQ data.

Two papers are concerned with this topic: *"Parallel Beamforming using Synthetic Transmit Beams"*, which was a joint work with Tore Bjåstad, and *"Reducing Color Flow Artifacts caused by Parallel Beam Acquisition"*.

Fast but realistic 3D ultrasound simulations

Simulated ultrasound images are important for several tasks, for example in testing new beamforming strategies and evaluating the accuracy of quantitative methods. We have developed such an ultrasound simulation tool, called *Fusk* – Fast Ultrasound Simulation in K-space.

Fusk uses several approximations to ensure that it is fast – it assumes that the point spread function (PSF) remains constant in Cartesian or polar coordinates, and the images are simulated as the convolution of the PSF and the object. This is a reasonably valid approximation for constant f-number or constant aperture imaging respectively. Additionally, the point scatterers in the object are anti-aliased and positioned on a beam-space grid before simulation, meaning that the sub-resolution movement of scatterers is maintained even with a coarse simulation grid. The PSF is generated directly in K-space using the Fraunhofer approximation, and the image is found through an inverse Fourier transformation of the product of the PSF and the K-space object.

Ultrasound imaging is an anisotropic process, where only the frequency components of an object that intersects with the K-space region of support for the PSF are visible. Muscular fibers are also anisotropic, as they absorb sound when insonified parallel to the fibers and have increased backscatter when the fibers are perpendicular to the beam. We have modeled this by directional filtering of the scattering amplitudes of the object, and have shown that this corresponds well with the anisotropic backscattering seen in the septum of the heart. The varying fiber direction through the septum and thus varying backscatter properties are responsible for the "bright line" in the center of the septum that can be seen in some projections.

Two papers address simulating realistic 3D ultrasound images: *"Fast Ultrasound Imaging Simulation in K-space"* and *"The Effect of Including Myocardial Anisotropy in Simulated Ultrasound Images of the Heart"*, which was a joint effort with Jonas Crosby.

Quantification of mitral regurgitation

Quantification of valvular regurgitation is important to determine the necessity and timing of surgery. We have combined the well-known idea of "the attenuation compensated volume flowmeter" with the recently available 2D matrix array probes to make a new method for quantification of valvular regurgitation. We have called the method MULDO, which is an acronym for "Multibeam hprf Doppler".

The use of a high pulse repetition frequency enabled the backscattered Doppler power from the core of high-velocity regurgitant jet to be isolated. The total power of the jet was found by summing the contribution from a grid of beams spread across the orifice. This measure is known to be proportional to the volume of moving blood within the sample volume, as long as the blood flow is laminar. The factor of proportionality was found from a reference measurement in the jet orifice in combination with a computer model of the width of the ultrasound beam.

The vena contracta just downstream from the orifice is known to have laminar flow, and it is known to be a good measure of the size of the actual orifice. The cross-sectional area (CSA) of the vena contracta is calculated based on the total Doppler power, the reference measurement, and a scaling factor that takes the position and beam profiles of the beams into account. In addition to providing estimates of the CSA, the power measurements from the multiple beams are shown as an estimate of the geometry of the orifice. An estimate of the regurgitant volume is obtained from multiplying the VCA with the velocity-time integral (VTI).

Muldo has been validated in simulations, *in vitro* in a pulsatile flow model with porcine prosthetic heart valves, and *in vivo* in a patient study with 27 individuals who had mitral regurgitation. These tests show that Muldo is able to quantify the severity of mitral regurgitation as long as the orifice is larger than the size of the reference beam. If the reference beam cannot fit inside the vena contracta, Muldo will overestimate the vena contracta cross-sectional area.

1.3 Discussion

This thesis contributes to three topics that are related to improve the quantification of cardiac function using 3D ultrasound imaging. The first topic is concerned with improving the image quality for high frame rate and 3D applications of B-mode and color flow imaging. This was done by using a method dubbed *STB – Synthetic Transmit Beams* which significantly reduces the artifacts from using multiple parallel receive beams. Quantitative methods such as speckle tracking are dependent on both a high frame rate and spatially shift invariant images which is made possible with STB.

The second topic is the development of fast but realistic simulated dynamic 3D ultrasound images. This was partly achieved by developing the simulator *Fusk – Fast Ultrasound Simulation in K-space*, which was shown to be three orders of magnitude faster than the industry standard Field II. We have also shown how the anisotropic scattering from skeletal muscle can be included in the simulations by directional filtering of the scatterers in the object to be simulated. These tools are used to generate test datasets for quantitative ultrasound methods.

The third topic concerns the development of *Muldo – Multibeam HPRF Doppler* – to quantify the severity of valvular regurgitation, in particular to assess the cross-sectional area of the vena contracta and the regurgitant volume of mitral regurgitation. These measures correspond well with the reference measurements both in computer simulations as well as *in vitro* and *in vivo*.

STB

The quality of an ultrasound imaging apparatus is given by its *image quality*, which is determined by a few key traits: spatial shift invariance, spatial resolution and penetration. Parallel receive beams are used to increase the frame rate at the cost of reduced spatial shift invariance, which means that the image quality is reduced with increasing frame rate.

The first aim of this work was to improve the frame rate of tissue and color flow images without reducing image quality, and the first step to achieve this was to characterize the artifacts caused by parallel receive beamforming. Since all artifacts were found to stem from the misalignment of transmit- and receive-beams, we suggested that the field of transmitted beams be interpolated to get "Synthetic Transmit Beams", so that each received beam could be aligned with a transmitted beam.

To be able to interpolate the transmitted field, it is necessary to have access to channel data from several transmits, which is a large amount of data to handle before beam formation. Fortunately, we found that the interpolation could be done after

beam formation, as long as the interpolation filters were linear and shift invariant (linear meant as a filter property, not filter type), which reduces the amount of data to be processed by several orders of magnitude.

In addition to the amount of data that must be available, the length of the interpolation filter is also determined by the susceptibility to motion artifacts. Higher order filters require more transmits with a longer acquisition time, which means that coherent interpolation is more likely to be influenced by the motion of the object. In this respect the two-tap linear filter is preferable. On the other hand, non-linear artifacts such as the Doppler bias cannot be completely restored by a linear filter, and the lateral frequency response of a linear filter is twice the width of an ideal filter, meaning that it requires some additional over-sampling for reconstruction without aliasing.

Even a linear filter can be affected by motion artifacts with fast moving objects like a regurgitant jet. These motion artifacts can be removed by conducting the STB interpolation incoherently on the power values for B-mode images or on the auto-correlation function with lag one for Doppler-based methods. This will give a speckle-reduce effect for B-mode images, and enable Doppler images to be reconstructed even with large time delays across interleave groups or in the elevation direction of 3D scans. One limitation of incoherent interpolation is that the lateral bandwidth of the data is increased for the second order data of the auto-correlation function, so to avoid aliasing it is necessary to increase the transmit beam density.

The hardware requirements for STB on beamformed data are also a limiting factor for the size of the interpolation filter. Since one beamformer is needed for each overlapping beam, the number of beamformers relative to the number of STB-processed beams equals the filter length. A linear interpolation filter thus needs twice the number of beamformers compared to regular parallel beamforming. This limitation is however about to disappear with the recent introduction of software beamforming in some commercially available systems. With a sufficiently capable and relatively cheap CPU or GPU, an arbitrary number of parallel beams can be generated.

To benefit from an increasing number of parallel receive beams spread over a larger area, the transmitted beam must be wider. This is typically done by limiting the transmit aperture, which increases the side lobe level and limits the penetration. It will also reduce the generation of 2. harmonic content in the received signals.

Fusk

Simulating realistic medical ultrasound images is a complex task which is solved with numerical methods, meaning that accurate simulations will require a high computational load. However, there are some applications where the simulation accuracy can be relaxed somewhat in exchange for increased processing speed. Our simulator *Fusk* is designed for this niche, where it is used for tasks such as simulating dynamic, realistic images of large objects like the heart.

The point spread function is calculated in the focal point of the transmitted beam, and approximated to be spatially shift invariant in the whole image, in polar or Cartesian coordinates. This means that the images appear as if dynamic focusing is used both with transmission and reception, and the errors in the simulation increases with

distance from the transmission focal point. In the special case where the aperture used for reception is significantly larger than the transmit aperture, the point spread function will be dominated by the reception beamforming, making the approximation better.

Even if the accuracy of *Fusk* is reduced away from the focal point as compared to approaches such as Field II, the simulated images can still be useful, since they are realistic and exhibit the traits of ultrasound images, such as speckle generation and anisotropy.

The use of a spatially shift invariant point spread function is the primary reason for the speed of *Fusk*, as the imaging is performed as a convolution that is executed efficiently in the spatial frequency domain, *a.k.a.* K-space. In addition to this, the simulation grid can be very coarse, since sub-resolution positioning of the scatterers is handled by an antialising filter. Finally, performing the simulation in the base-band requires a lower scatterer density radially compared to full-band simulations, and fewer scatterers result in faster processing.

We have included the anisotropy of ultrasound imaging as a directional filter for the scattering strength in the point scatterers. This modification of a cloud of scatterers enabled us to reconstruct the "bright line" that is seen in the septum for some projections. This implies that the line is not a structure in the septum, but merely an effect of the varying fiber direction through the septum. Including this effect in simulations can be important for the validation of edge-detecting methods. The lateral wall is typically imaged poorly from an apical view, which is probably due to the muscle fibers being parallel to the beam in this projection, and neglecting this effect will give unrealistically fine images.

Another way to add anisotropy to the objects is to approximate smooth surfaces with lines and triangles. The Fourier transforms of arbitrarily shaped and positioned lines and triangles are known analytically, meaning that these structures can be inserted directly into K-space by superimposing the K-space response for numerous lines or triangles. This is currently a work in progress and further details is not given in this thesis.

In addition to simulating dynamic 3D B-mode images, *Fusk* can be used to simulate 3D Doppler images very efficiently, as the full 3D auto-correlation function can be simulated from the same number of simulated volumes as the packet size. In reality the scatterers will move slightly between the acquisition of each ultrasound beam, meaning that the hemodynamics will change slightly within an image, particularly within 3D color flow images where the volume rate can be quite low. With *Fusk* the images are simulated as a 3D convolution, meaning that there will be no such timing differences between the ultrasound beams.

Muldo

The current common practice of grading valvular regurgitation is semi-quantitative, which makes it harder to establish and follow guidelines for thresholds and treatment, as well as determining how to follow up on patients. With the recent introduction of real time 3D Doppler ultrasound, we have revisited some old principles for the

quantification of volume flow to see if they can benefit from the added dimension. "The attenuation compensated volume flowmeter" proposed by Hottinger and Meindl some 30 years ago [36] did not succeed in gaining popularity, probably due to the inability to measure volume flow in large arteries with an inhomogeneous measurement beam. More recently Buck *et. al.* proposed using the method to quantify the regurgitant volume at the vena contracta, and showed good results in vivo when compared to magnetic resonance imaging [37–39]. Buck used one wide beam for measuring the Doppler power and one narrow beam as a reference measurement, and calculated the Doppler power with the help of tracing the Doppler spectrum.

Several enhancements are possible when the measurements are done with multiple beams and scanned electronically with a 2D matrix array, as we have done with *Muldo*. First of all, the reference beam is selected as the beam that most likely intersects the vena contracta. In contrast to current practice, where the operator has to steer a single beam into the core of a moving jet stream, our approach requires less operator skill and precision to make a valid reference measurement.

Using the sum of multiple beams as the composite Doppler power measure also ensures a homogeneous sensitivity and increases the signal-to-noise ratio compared to the single-beam method, as can be seen from Fig. F.2. Transmitting a single, wide beam requires a small aperture, with less penetration compared to using the full aperture, and the resulting wide beam will not be homogeneous, but will have a nearly parabolic sensitivity. Another benefit of using multiple power measurements is that they can be used to make estimates of the geometry of the cross-sectional area of the orifice.

A high pulse repetition frequency (HPRF) is used to acquire the multiple Doppler signals to be able to separate the high velocity core of the regurgitant jets from the entrained fluid surrounding it. With HPRF acquisition several pulses are transmitted before the deep echoes from the first pulse has returned to the probe, meaning that the received echoes from multiple sample volumes along the beam are mixed together. This range ambiguity introduced by HPRF acquisition is not important for measuring the velocity of regurgitant jets, as the signals received from the ambiguous sample volumes are removed by a clutter filter as long as the beam only intersects one jet. This is normally the case for transthoractic imaging.

HPRF acquisition separates the geometry estimates of *Muldo* from what can be obtained from normal 3D color flow, as the Nyquist velocity will be close to the peak velocity of the jet, and the jet velocities are resolved without aliasing. Transmitting the pulses so quickly also increases the frame rate, but not sufficiently to obtain a reasonable frame rate for 3D Doppler imaging. Since the volume rate with a reasonably sized 3D region of interest (ROI) was typically just 10Hz, we wanted to apply parallel receive beams to increase it. However, it proved difficult to obtain power measures that were not riddled with severe parallel beam artifacts, which spurred our interest and led to the paper "Reducing Color Flow Artifacts caused by Parallel Beam Acquisition".

With pulsed Doppler acquisition it is impossible to transmit and receive simultaneously, and it takes some time to switch from transmission to reception. Together with the pulse length and the radial length of the ROI, this gives the minimal time delay between pulses. This means that the pulse repetition frequency has to be selected in a

trade-off with the axial size of the region of interest (ROI), and with a desired Nyquist velocity of above $3m/s$, the ROI has to be made very small axially. Along with the movement of the mitral plane, this can make it a challenge to position the ROI around the vena contracta of mitral regurgitation.

With *Muldo* no assumptions are made about the geometry of the lesion, and it should be possible to measure the area of multiple jets, eccentric jets and asymmetric jets as long as one beam can fit inside the orifice to serve as the reference beam – otherwise the cross-sectional area will be overestimated. For very large orifices, on the other hand, the estimates will be underestimated. When several beams are inside the orifice, the beam with the highest power is selected as the reference beam. Due to the stochastic nature of the Doppler signal, this overestimates the reference beam, which in turn makes the area estimate too low.

In vivo comparisons of *Muldo* with magnetic resonance imaging (MRI) show good correlations, particularly for medium and large orifices. Organic mitral regurgitation showed better correlation with MRI than functional mitral regurgitation, which is probably due to the fact that functional mitral regurgitation is usually asymmetric, as opposed to organic mitral regurgitation, meaning that it is less likely that a valid reference measurement has been made despite a large cross-sectional area.

Muldo is currently a semiautomatic method, where the only operator interaction apart from acquisition is to confirm which frames are valid measurements. This approach is necessary to make sure that the vena contracta is indeed inside the ROI, but the manual selection can be automated further to make *Muldo* fully automatic.

There are also a few drawbacks of *Muldo*, one of which is the need for a computer model of the ratio of the composite measurement beam and the reference beam. Aberrations and reverberations will surely invalidate all assumptions about the shape of the beam profiles, but nevertheless it seems to work well. This is probably due to the division of the reference beam profile and the sum of beam profiles of the composite measurement beam, such that any common terms will cancel out. This is the beauty of "the attenuation compensated volume flowmeter"!

1.4 Conclusion

Real time three dimensional ultrasound scanners are making their way into the hospitals. To be truly useful in clinical practice, the third dimension should provide additional quantitative information compared to standard 2D echocardiography, and this thesis addresses how 3D quantitative echocardiography can be improved.

The image quality for high frame rate applications is improved with *STB – Synthetic Transmit Beamforming*, and image quality is among the most important features for quantitative measurements. In this thesis only results for two-dimensional imaging is shown, although it is straight forward to extend STB to three dimensions, particularly with incoherent synthetization of the beams. Further, three-dimensional dynamic simulated ultrasound images are important for validation of emerging 3D quantitative methods like 3D speckle tracking and measurements of ventricular volume. Such simulated images of large and complex geometries can readily be obtained with *Fusk* –

Fast Ultrasound Simulation in K-space. Finally, quantification of the severity of valvular regurgitation is performed with 3D Doppler data using *Muldo – Multibeam HPRF Doppler*. As long as a single ultrasound beam can fit inside the orifice to obtain a reference measurement, the cross sectional area can be quantified *in vitro*. Mild regurgitations are significantly overestimated when *in vivo* measurements are compared to magnetic resonance imaging, but this condition can easily be identified as such by standard 2D Doppler examinations, making further efforts unnecessary. For moderate and severe mitral regurgitation the estimated regurgitant volume correlates well with magnetic resonance imaging.

1.5 List of publications

What follows is a list of the papers and patent applications where I have made significant contributions during my time as a PhD candidate.

Peer reviewed papers

1. **Torbjørn Hergum**, Tore Bjåstad, Kjell Kristoffersen and Hans Torp, "Parallel Beamforming using Synthetic Transmit Beams", *IEEE Transactions on Ultrasonics, Ferroelectrics and Frequency Control*, vol. 54, no. 2, pp. 271–80, 2007.

2. Jonas Crosby, Brage H. Amundsen, **Torbjørn Hergum**, Espen W. Remme, Stian Langeland and Hans Torp, "3-D Speckle Tracking for Assessment of Regional Left Ventricular Function", *Ultrasound in Medicine and Biology*, vol. 35, no. 3, pp. 458–71, 2009.

3. Jonas Crosby, **Torbjørn Hergum**, Espen W. Remme and Hans Torp, "The effect of including myocardial anisotropy in simulated ultrasound images of the heart", *IEEE Transactions on Ultrasonics, Ferroelectrics and Frequency Control*, vol. 56, no. 2, pp. 326–33, 2009.

4. **Torbjørn Hergum**, Thomas Renhult skaug, Knut Matre, and Hans Torp, "Quantification of Valvular Regurgitation Area and Geometry Using HPRF 3D Doppler", *IEEE Transactions on Ultrasonics, Ferroelectrics and Frequency Control*, vol. 56, no. 5, pp. 975–82, 2009.

5. **Torbjørn Hergum**, Stian Langeland, Espen W. Remme, and Hans Torp, "Fast Ultrasound Imaging Simulation in K-space", *IEEE Transactions on Ultrasonics, Ferroelectrics and Frequency Control*, vol. 56, no. 6, pp. 1159–67, 2009

Submitted for publication

1. **Torbjørn Hergum**, Tore Bjåstad, Lasse Løvstakken, Kjell Kristoffersen and Hans Torp, "Reducing Color Flow Artifacts caused by Parallel Beam Acquisition", submitted to *IEEE Transactions on Ultrasonics, Ferroelectrics and Frequency Control*.

2. Thomas Renhult Skaug, **Torbjørn Hergum**, Brage Amundsen, Terje Skjærpe, Hans Torp and Bjørn Olav Haugen, "Quantification of Mitral Regurgitation using HPRF 3D Color Doppler", submitted to *Circulation*.

Patent applications

1. **Torbjørn Hergum** and Hans Torp, "Methods and Devices for Estimating Blood Flow Characteristics", WO2009031034.

2. Kjell Kristoffersen, Hans Torp, Tore Bjåstad, Lasse Løvstakken, **Torbjørn Hergum** and Johan Kirkhorn "Suppression of multiline artifacts in color flow imaging"

Conference proceedings

1. **Torbjørn Hergum**, Tore Bjåstad and Hans Torp, "Parallel Beamforming using Synthetic Transmit Beams", *Proc. IEEE Ultrason. Symp.*, vol. 2, pp. 1401–04, 2004.

2. **Torbjørn Hergum**, Jonas Crosby, Marit Jordet Langhammer and Hans Torp, "The Effect of Including Fiber Orientation in Simulated 3D Ultrasound Images of the Heart", *Proc. IEEE Ultrason. Symp.*, pp. 1991–94, 2006.

3. **Torbjørn Hergum**, Thomas Renhult Skaug, Knut Matre and Hans Torp, "Quantification of Valvular Regurgitation Area and Geometry using HPRF 3D Doppler", *Proc. IEEE Ultrason. Symp.*, pp. 1179–82, 2008.

4. Hang Gao, **Torbjørn Hergum**, Jan D'hooge and Hans Torp "Comparison of the Performance of Different Tools for Fast Simulation of Ultrasound Data", *Proc. IEEE Ultrason. Symp.*, pp. 1318–21, 2008.

References

[1] S. B. Barnett, G. R. T. Haar, M. C. Ziskin, H. D. Rott, F. A. Duck, and K. Maeda, "International recommendations and guidelines for the safe use of diagnostic ultrasound in medicine," *Ultrasound in medicine & biology*, vol. 26, no. 3, pp. 355–366, 2000.

[2] S. Brekke, S. I. Rabben, A. Støylen, A. Haugen, G. U. Haugen, E. N. Steen, and H. Torp, "Volume stitching in Three-Dimensional echocardiography: Distortion analysis and extension to real time," *Ultrasound in Medicine & Biology*, vol. 33, pp. 782–796, May 2007.

[3] D. P. Shattuck, M. D. Weinshenker, S. W. Smith, and O. T. von Ramm, "Explososcan: A parallel processing technique for high speed ultrasound imaging with linear phased arrays," *Journal of the Acoustical Society of America*, vol. 75, no. 4, pp. 1273–1282, 1984.

[4] O. T. von Ramm, S. W. Smith, and H. G. Pavy, "High-speed ultrasound volumetric imaging system – part ii: Parallel processing and image display," *IEEE Transactions on Ultrasonics, Ferroelectrics, and Frequency Control*, vol. 38, March 1991.

[5] L. J. Augustine, "High resolution multiline ultrasonic beamformer." United States Patent 4.644.795, 1987.

[6] N. Wright, S. H. Maslak, D. J. Finger, and A. Gee, "Method and apparatus for coherent image formation." United States Patent 5.623.928, 1997.

[7] B. S. Robinson, "Ultrasonic diagnostic imaging systems with blended multiline for 2d and 3d applications." United States Patent 6.482.157, 2001.

[8] T. Varslot and S.-E. Måsøy, "Forward propagation of acoustic pressure pulses in 3D soft biological tissue," *Modeling, Identification and Control*, vol. 27, no. 3, pp. 181–200, 2006.

[9] J. Jensen and N. B. Svendsen, "Calculation of pressure fields from arbitrarily shaped, apodized, and excited ultrasound transducers," *IEEE Transactions on Ultrasonics, Ferroelectrics, and Frequency Control*, vol. 39, pp. 262–267, 1992.

[10] J. A. Jensen and S. I. Nikolov, "Fast simulation of ultrasound images," in *IEEE International Ultrasonics Symposium Proceedings*, pp. 1721–1724, 2000.

[11] H. Gao, H. F. Choi, P. Claus, S. Boonen, S. Jaecques, G. H. V. Lenthe, G. V. D. Perre, W. Lauriks, and J. D'hooge, "A fast convolution-based methodology to simulate 2-Dd/3-D cardiac ultrasound images," *IEEE Transactions on Ultrasonics, Ferroelectrics and Frequency Control*, vol. 56, no. 2, pp. 404–409, 2009.

[12] F. Orderud, G. Kiss, S. Langeland, E. Remme, H. Torp, and S. Rabben, "Combining edge detection with speckle-tracking for cardiac strain assessment in 3D echocardiography," in *IEEE International Ultrasonics Symposium Proceedings*, pp. 1959–1962, 2008.

[13] J. Crosby, B. H. Amundsen, T. Hergum, E. W. Remme, S. Langeland, and H. Torp, "3-D speckle tracking for assessment of regional left ventricular function," *Ultrasound in Medicine & Biology*, vol. 35, pp. 458–71, Mar. 2009.

[14] R. M. Lang, M. Bierig, R. B. Devereux, F. A. Flachskampf, E. Foster, P. A. Pellikka, M. H. Picard, M. J. Roman, J. Seward, J. Shanewise, S. Solomon, K. T. Spencer, M. S. J. Sutton, and W. Stewart, "Recommendations for chamber quantification," *European Journal of Echocardiography*, vol. 7, pp. 79–108, Mar. 2006.

[15] A. Støylen and T. Skjaerpe, "Systolic long axis function of the left ventricle. global and regional information," *Scandinavian Cardiovascular Journal*, vol. 37, no. 5, pp. 253–258, 2003.

[16] C. B. Ingul, E. Rozis, S. A. Slordahl, and T. H. Marwick, "Incremental value of strain rate imaging to wall motion analysis for prediction of outcome in patients undergoing dobutamine stress echocardiography," *Circulation*, vol. 115, no. 10, p. 1252, 2007.

[17] H. Baumgartner, J. Hung, J. Bermejo, J. B. Chambers, A. Evangelista, B. P. Griffin, B. Iung, C. M. Otto, P. A. Pellikka, and M. Quinones, "Echocardiographic assessment of valve stenosis: EAE/ASE recommendations for clinical practice," *Journal of the American Society of Echocardiography*, 2008.

[18] M. A. Quiñones, C. M. Otto, M. Stoddard, A. Waggoner, and W. A. Zoghbi, "Recommendations for quantification of doppler echocardiography: a report from the doppler quantification task force of the nomenclature and standards committee of the american society of echocardiography," *Journal of the American Society of Echocardiography*, vol. 15, no. 2, pp. 167–184, 2002.

[19] F. Orderud and S. Rabben, "Real-time 3D segmentation of the left ventricle using deformable subdivision surfaces," in *Computer Vision and Pattern Recognition, 2008. CVPR 2008. IEEE Conference on*, pp. 1–8, 2008.

[20] B. O. Haugen, S. Berg, K. M. Brecke, S. O. Samstad, T. Skjaerpe, S. A. Slordahl, and H. Torp, "Measurement of volumetric mitral and aortic blood flow based on a new freehand three-dimensional colour flow imaging method. an in vivo validation," *European Journal of Echocardiography*, vol. 1, pp. 204–212, Sep 2000.

[21] B. O. Haugen, S. Berg, K. M. Brecke, H. Torp, S. A. Slordahl, T. Skaerpe, and S. O. Samstad, "Blood flow velocity profiles in the aortic annulus: a 3-dimensional freehand color flow doppler imaging study," *Journal of the American Society of Echocardiography*, vol. 15, pp. 328–333, Apr 2002.

[22] M. Enriquez-Sarano, J. Avierinos, D. Messika-Zeitoun, D. Detaint, M. Capps, V. Nkomo, C. Scott, H. V. Schaff, and A. J. Tajik, "Quantitative determinants of the outcome of asymptomatic mitral regurgitation," *The New England Journal of Medicine*, vol. 352, pp. 875–883, Mar. 2005.

[23] M. Enriquez-Sarano, C. W. Akins, and A. Vahanian, "Mitral regurgitation," *The Lancet*, vol. 373, no. 9672, pp. 1382–1394, 2009.

[24] M. I. Ahmed, D. C. McGiffin, R. A. O'Rourke, and L. J. Dell'Italia, "Mitral regurgitation," *Current Problems in Cardiology*, vol. 34, pp. 93–136, Mar. 2009.

[25] L. Sugeng, P. Coon, L. Weinert, N. Jolly, G. Lammertin, J. E. Bednarz, K. Thiele, and R. M. Lang, "Use of real-time 3-dimensional transthoracic echocardiography in the evaluation of mitral valve disease," *Journal of the American Society of Echocardiography*, vol. 19, no. 4, pp. 413–421, 2006.

[26] B. J. Roberts and P. A. Grayburn, "Color flow imaging of the vena contracta in mitral regurgitation: technical considerations," *Journal of the American Society of Echocardiography*, vol. 16, pp. 1002–1006, September 2003.

[27] W. A. Zoghbi, M. Enriquez-Sarano, E. Foster, P. A. Grayburn, C. D. Kraft, R. A. Levine, P. Nihoyannopoulos, C. M. Otto, M. A. Quinones, H. Rakowski, W. J. Stewart, A. Waggoner, and N. J. Weissman, "Recommendations for evaluation of the severity of native valvular regurgitation with two-dimensional and doppler echocardiography," *Journal of the American Society of Echocardiography*, vol. 16, pp. 777–802, Jul 2003.

[28] P. Kahlert, B. Plicht, I. M. Schenk, R.-A. Janosi, R. Erbel, and T. Buck, "Direct assessment of size and shape of noncircular vena contracta area in functional versus organic mitral regurgitation using real-time three-dimensional echocardiography," *Journal of the American Society of Echocardiography*, vol. 21, pp. 912–921, Aug 2008.

[29] L. Sugeng, L. Weinert, and R. M. Lang, "Real-time 3-Dimensional color doppler flow of mitral and tricuspid regurgitation: Feasibility and initial quantitative comparison with 2-Dimensional methods," *Journal of the American Society of Echocardiography*, vol. 20, pp. 1050–1057, Sept. 2007.

[30] F. Recusani, G. Bargiggia, A. Yoganathan, A. Raisaro, L. Valdes-Cruz, H. Sung, C. Bertucci, M. Gallati, V. Moises, and I. Simpson, "A new method for quantification of regurgitant flow rate using color doppler flow imaging of the flow convergence region proximal to a discrete orifice. an in vitro study," *Circulation*, vol. 83, pp. 594–604, Feb. 1991.

[31] P. Vandervoort, J. Rivera, D. Mele, I. Palacios, R. Dinsmore, A. Weyman, R. Levine, and J. Thomas, "Application of color doppler flow mapping to calculate effective regurgitant orifice area. an in vitro study and initial clinical observations," *Circulation*, vol. 88, pp. 1150–1156, Sept. 1993.

[32] Y. Matsumura, G. Saracino, K. Sugioka, H. Tran, N. L. Greenberg, N. Wada, M. Toyono, S. Fukuda, T. Hozumi, and J. D. Thomas, "Determination of regurgitant orifice area with the use of a new Three-Dimensional flow convergence geometric assumption in functional mitral regurgitation," *Journal of the American Society of Echocardiography*, vol. 21, no. 11, pp. 1251–1256, 2008.

[33] M. Enriquez-Sarano, F. A. Miller, S. N. Hayes, K. R. Bailey, A. J. Tajik, and J. B. Seward, "Effective mitral regurgitant orifice area: clinical use and pitfalls of the proximal isovelocity surface area method," *Journal of the American College of Cardiology*, vol. 25, no. 3, pp. 703–709, 1995.

[34] T. Buck, C. H. P. Jansen, A. P. Yoganathan, R. A. Levine, and M. D. Handschumacher, "Hemisphere versus hemiellipse: when is each most accurate for proximal isovelocity calculation of regurgitant flows," *Journal of the American College of Cardiology*, vol. 31, no. 1002, pp. 385–385, 1998.

[35] C. Yosefy, R. Levine, J. Solis, M. Vaturi, M. Handschumacher, and J. Hung, "Proximal flow convergence region as assessed by real-time 3-dimensional echocardiography: Challenging the hemispheric assumption," *Journal of the American Society of Echocardiography*, vol. 20, no. 4, pp. 389–96, 2007.

[36] C. F. Hottinger and J. D. Meindl, "Blood flow measurement using the attenuation-compensated volume flowmeter," *Ultrasonic Imaging*, vol. 1, pp. 1–15, January 1979.

[37] T. Buck, R. A. Mucci, J. L. Guerrero, G. Holmvang, M. D. Handschumacher, and R. A. Levine, "The power-velocity integral at the vena contracta, a new method for direct quantification of regurgitant volume flow," *Circulation*, vol. 102, pp. 1053–1061, 2000.

[38] T. Buck, B. Plicht, P. Hunold, R. A. Mucci, R. Erbel, and R. A. Levine, "Broad-beam spectral doppler sonification of the vena contracta using matrix-array technology," *Journal of the American College of Cardiology*, vol. 45, 2005.

[39] T. Buck, R. A. Mucci, J. L. Guerrero, G. Holmvang, M. D. Handschumacher, and R. A. Levine, "Flow quantification in valvular heart disease based on the integral of backscattered acoustic power using doppler ultrasound," in *IEEE International Ultrasonics Symposium Proceedings*, March 2000.

Paper A

Parallel Beamforming using Synthetic Transmit Beams

Torbjørn Hergum[1], Tore Bjåstad[1], Kjell Kristoffersen[2] and Hans Torp[1]
[1]Department of Circulation and Medical Imaging, NTNU, Trondheim, Norway
[2]GE Vingmed Ultrasound, Horten, Norway

Abstract

Parallel beamforming is frequently used to increase the acquisition rate of medical ultrasound imaging. However, such imaging systems will not be spatially shift invariant due to significant variation across adjacent beams. This paper investigates a few methods of parallel beamforming who aims at eliminating this flaw and restore the shift invariance property. The beam-to-beam variations occur because the transmit and receive beams are not aligned. The underlying idea of the main method presented here is to generate additional synthetic transmit beams (STB) through interpolation of the received, unfocused signal at each array element prior to beamforming. Now each of the parallel receive beams can be aligned perfectly with a transmit beam - synthetic or real - thus eliminating the distortion caused by misalignment.

The proposed method was compared to the other compensation methods through a simulation study based on the ultrasound simulation software Field II. The results have been verified with in vitro experiments. The simulations were done with parameters similar to a standard cardiac examination with two parallel receive beams and a transmit-line spacing corresponding to the Rayleigh criterion, wavelength times f-number ($\lambda \cdot f\#$).

From the results presented it is clear that straightforward parallel beamforming reduces the spatial shift invariance property of an ultrasound imaging system. The proposed method of using synthetic transmit beams seems to restore this important property, enabling higher acquisition rates without loss of image quality.

IEEE Transactions on UFFC, vol. 54, no. 2, pp. 271-280, 2007

A.1 Introduction

When performing ultrasound imaging of moving structures there is a demand to increase the rate of the image acquisition. This is particularly true for 3D imaging of the moving heart. A common way to increase the frame-rate of ultrasound imaging without compromising the number of scan lines is to use multiple beamformers [1][2]. With this approach several parallel receive-beams from closely spaced regions can be acquired simultaneously for each transmit-beam. The image acquisition rate is thus increased proportionally to the number of beamformers. However, as the transmit- and receive-beams are misaligned such a technique will result in spatial shift variance due to considerable beam-to-beam variation across adjacent beams. The shift variance is manifested as stationary stripes in the ultrasound image, and becomes more distinctive with increasing number of parallel receive beams.

Some methods have been proposed to solve this problem. One of them is to use a *sinc*-apodization on the transmit aperture, which theoretically will generate a square transmit beam profile, thus providing an uniform two-way response regardless of where the receive beam is positioned inside the transmit beam [3].

Another proposal is found in an U.S. patent submitted by J. N. Wright *et al.* [4]. The patent formulates a general method for reducing parallel beam artifacts based on creating synthetic scan lines through interpolation on combinations of existing scan lines. However, there is no obvious way of selecting the optimum beam spacing and interpolation filter coefficients when the 2-way beamprofiles are skewed or have irregular spacing.

In contrast to synthetic scan lines the idea introduced in this paper is to create synthetic transmit beams through interpolation on the unfocused signal at each element. However, with a proper choice of interpolation filter the interpolation can be performed on beamformed data instead of element data, making it easy to implement in real-time.

To begin with the inherent problems with parallel processing will be addressed. Then the general theory of the proposed method is examined, followed by one specific implementation of it. Next this is compared to other parallel processing compensation methods. Finally results from comparing the various compensation methods through simulations and in vitro experiments will be presented and discussed.

A.2 Background and Problem Statement

The geometric distortions due to misalignment of the transmit- and receive beams can be separated into two underlying effects; “warping” and “skewing”. Beam warping, sometimes called “beam wander”, is the effect that the two-way beam will in general not follow a straight line. When a transmit- and receive beam is not perfectly aligned, the transmit beam will ’pull’ the receive beam toward its center, making the center of the two-way beam different from that of both the transmit- and receive beams. For the following argument the beam profiles will be assumed to have a Gaussian shape. The depth-dependent beam width is given by $\sigma_t(r)$ and $\sigma_r(r)$ for the transmit- and

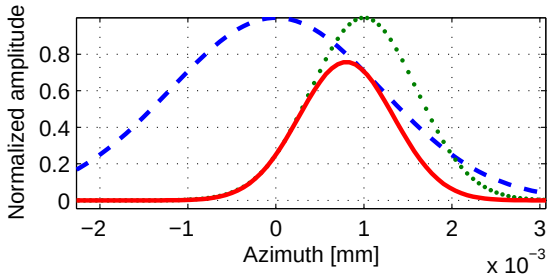

Figure A.1: The warping effect of misaligned ultrasound Gaussian-shaped transmit (dashed) and receive (dotted) beams. Notice that the two-way beam (solid), the product of the transmit and receive beams, is centered in-between the peaks of the two one-way functions.

receive beam respectively, giving the two-way beam profile $g_{tr}(x)$ as

$$\begin{aligned} g_{tr}(x,r) &= g_t(x-x_t,r)g_r(x-x_r,r) \\ &\Downarrow \\ g_{tr}(x,r) &= e^{-\frac{(x-x_t)^2}{2\sigma_t(r)^2}} e^{-\frac{(x-x_r)^2}{2\sigma_r(r)^2}} \end{aligned} \tag{A.1}$$

where subscript t indicates "transmit", r indicates "receive" and tr indicates "transmit-receive". An example of $g_{tr}(x)$ is plotted with $g_t(x)$ and $g_r(x)$ in Fig. A.1, showing the warping.

The peak position $x = x_p$ of this function is found where $\partial g_{tr}/\partial x = 0$. The origin of the coordinate system is then positioned at the center of the transmit beam, that is, $x_t = 0$, yielding the following equation for the position of the peak:

$$\begin{aligned} x_p &= \frac{\sigma_t^2 x_r + \sigma_r^2 x_t}{\sigma_t^2 + \sigma_r^2} \\ &\Downarrow x_t = 0 \\ x_p &= \frac{\sigma_t^2 x_r}{\sigma_t^2 + \sigma_r^2} \end{aligned} \tag{A.2}$$

The peak position of the two-way beams resulting from three transmit events using two parallel receive beams each is plotted in Fig. A.2. The left part of the figure is simulated using Field II [5]. Although only the peak position of the pulse-echo field is plotted here, the full 2D transmit- and receive profiles were calculated. The $-3dB$ contour of these profiles were used as the depth-dependent beam widths $\sigma_t(r)$ and $\sigma_r(r)$ of (A.2). The peak position using the Gaussian beam profiles with depth dependent beam widths provided by Field II simulation is displayed in the right part of Fig. A.2. Note that the received signal is assumed to follow straight lines. Due to the warping effect the samples are acquired from along curved lines, making the lateral

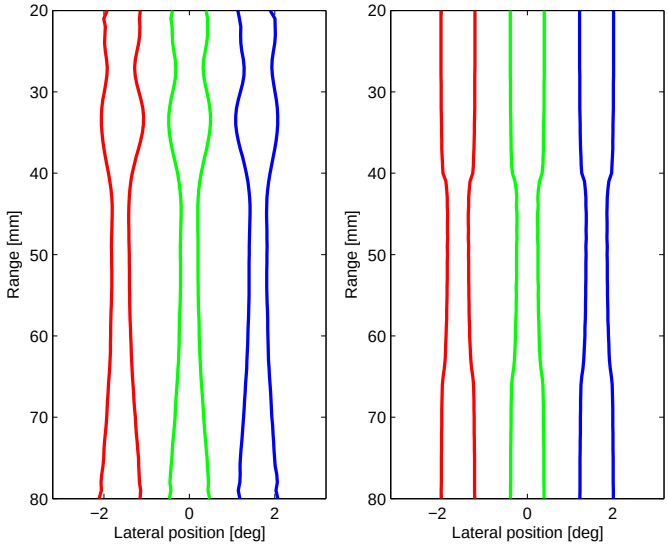

Figure A.2: The lateral *peak position* of two-way beams as a function of depth. The left figure is simulated using Field II. The right figure is a plot of (A.2), which uses the Gaussian beam approximation. The two-way beams are the result of three transmit beams with two parallel receive beams each. Note the uneven sampling resulting from the curved scan lines, particularly the lack of samples at some locations around the focal depth at 5 cm. See text for details.

sampling non-regular. If the beams are distributed according to the Nyquist criterion, this non-regular sampling will lead to under-sampling, aliasing and thus loss of spatial invariance and image quality.

The simulation settings for both simulations can be found in Table A.1. As can be seen by comparing the left and right part of the figure, the Gaussian beam approximation is only valid in the vicinity of the focal depth. In the near- and far-field this simple model is not sufficient to describe the field.

The second part of the geometric distortions are due to "skewing", since the beam profiles are in fact not Gaussian as assumed above. A skew (non-symmetric) two-way RMS beam profile resulting from offsetting a symmetric receive beam and a symmetric transmit beam is shown in Fig. A.3. The RMS beam profile is found by calculating the root mean square along the time/radial direction of the transmit-, receive- and two-way field simulated using Field II.

Yet another effect of parallel beamforming is the loss of energy caused by misaligning the transmit- and receive beams. Using two parallel receive beams positioned symmetrically around the transmit beam will decrease the signal-to-noise ratio (SNR). However, using more than two parallel receive beams will give beams with varying gain. Compensating for this varying gain loss through amplification (*i.e.* by using (A.1)) will give beams with varying SNR and variance, further degrading the spatial invariance.

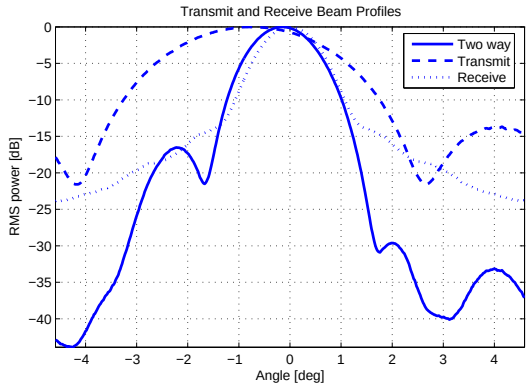

Figure A.3: Beam profiles of transmit-, receive-, and two-way response. The transmit f# is twice that of the receive f#. Note the skewness of the two-way profile.

A.3 Shift Invariance through Coherent Interpolation

The goal of the proposed method in this article is to overcome the geometrical distortions caused by misaligned transmit- and receive-beams by creating synthetic transmit-beams in-between the real transmit-beams. The first step on the way to achieve this is to transmit beams with a spacing of no more than the Nyquist sampling criterion for ultrasound, $f\#\lambda$, which is also called the Rayleigh criterion [6]. Assume for the sake of the argument that the signal received on each element of the aperture and for all transmit events are stored separately and coherently in the ultrasound scanner. The sampling theorem states that the value from any intermediate beam can be found from these data through interpolation. Next these interpolated data can be passed through a receive beamformer, adding appropriate focusing delays to steer in the direction of the synthetic transmit beam. Since the receive beams are steered to the same point in space as the synthetic transmit beams, there will be no geometrical distortions of the two-way beams due to misalignment.

Let us now state this more formally. Fig. A.4 puts some of the symbols into a sketch showing the elements of a simple transducer and the signals received from two consecutive excitation events. The aperture consists of N elements transmitting M beams into the imaging sector. To transmit beam number k, $1 < k < M$, the aperture is focused on the point x_k at the depth $d = ct_0/2$. The received signal at aperture element n after focusing at point x_k is denoted $S_n(x_k, t_0)$, where $1 < n < N$. The signal originating from an intermediate position x_i can be found through interpolation after collecting data from the desired amount of beams k. For each element n on the aperture the recorded signals $S_n(x_k)$ are used to find the synthetic signal $\tilde{S}_n(x_i)$ using the interpolation filter $h(x_i, k)$:

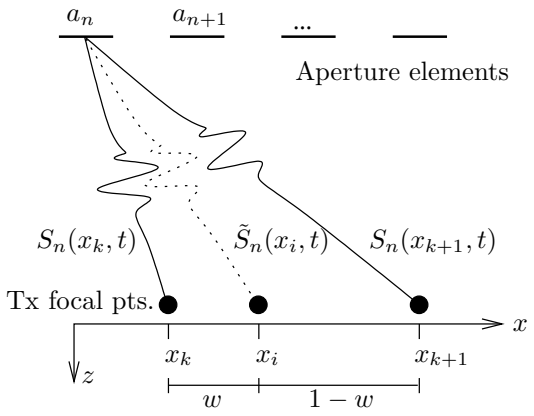

Figure A.4: Illustration of the received signals on aperture element a_n when transmit focus is set at the points x_k and x_{k+1}. The interpolated signal $\tilde{S}_n(x_i,t)$ from the synthetic transmit beam focused at the point x_i is also indicated. The normalized distances between the three points of interest is shown at the bottom.

$$\tilde{S}_n(x_i,t) = \sum_k h(x_i,k) S_n(x_k,t). \tag{A.3}$$

The total synthetic receive signal $\tilde{S}(x_i,t)$ from the point x_i in space is found by focusing the synthetic receive- signals electronically to the point x_i by adding time delays $\tau_n(x_i)$, and summing the signal from all elements on the aperture:

$$\begin{aligned}
\tilde{S}(x_i,t) &= \sum_n \tilde{S}_n(x_i, t-\tau_n(x_i)) && \text{(A.4)}\\
&= \sum_n \sum_k h(x_i,k) S_n(x_k, t-\tau_n(x_i)) && \text{(A.5)}\\
&= \sum_k h(x_i,k) \sum_n S_n(x_k, t-\tau_n(x_i)) && \text{(A.6)}\\
&= \sum_k h(x_i,k) S_k(x_i,t) && \text{(A.7)}
\end{aligned}$$

where the interchange of the order of the summations from (A.5) to (A.6) can be done if the interpolation filter is linear, shift invariant and independent of n (linear meant as a filter property, not filter type). The last sum in (A.6) is the mathematical expression for the signal $S_k(x_i,t)$ from a beam transmitted toward the point x_k and then focused at the point x_i while receiving. Instead of interpolating the received samples from each aperture element the same result can be achieved from steering the receive-beam toward the same point in subsequent transmit-events and then find the synthetic scan

line through interpolation of these signals, as is seen from (A.7). This will be denoted as parallel beamforming with STB (Synthetic Transmit Beams) throughout the text.

Changing the order of summation in (A.6) facilitates the practical implementation of STB as only the output data from the beamformer has to be buffered, which is a fraction of the size of the received signal from all aperture elements.

It is worth noting that STB like all coherent lateral interpolation methods assumes negligible object movement between subsequent transmit beams. If not, the phase difference between the interpolated signals might induce artifacts due to destructive interference. The maximum wall velocity in the left ventricle is typically $12cm/s$ [7] and a typical pulse repetition frequency for cardiac imaging is $4kHz$. The maximum wall displacement between subsequent beams is then found as $\frac{12cm/s}{4kHz} = 30\mu m$, which for a typical cardiac transmit frequency of $2.5MHz$ is less than one twentieth of a wavelength. A commonly used limit for coherent summation is $\lambda/8$ [6], so the STB method will sum coherently for fast cardiac movements as long as the interpolation filter is short.

For a rectangular aperture the Nyquist sampling requirement for beam density can be found from the Fraunhofer approximation to be one beam per $f_{\#}\lambda$, where $f_{\#} = F/a$ is the f-number, F is the transmit focus depth, and a is the aperture size on transmit or receive [8]. This is called the Rayleigh criterion. After including the oversampling factor p^t and rearranging terms the lateral sampling frequency is found as

$$f_s^t = \frac{1}{p^t} \cdot \frac{a^t}{F \cdot \lambda} \qquad p^t \leq 1. \tag{A.8}$$

Again according to the Fraunhofer approximation the lateral bandwidth of the pulse-echo field is given by the convolution of the transmit- and receive apertures. Thus the two-way sampling frequency is found as

$$f_s^{tr} = \frac{1}{p^{tr}} \cdot \frac{(a^t + a^r)}{F \cdot \lambda} \qquad p^{tr} \leq 1 \tag{A.9}$$

where a^t and a^r is the aperture size on transmit and receive respectively, λ the wavelength of the center frequency and p^t and p^{tr} oversampling factors on transmit and two-way respectively. The number of necessary parallel beams is now found as the ratio between f_s^{tr} and f_s^t:

$$N_{pb} = \frac{p^t}{p^{tr}} \cdot (1 + \frac{a^r}{a^t}) \tag{A.10}$$

For marginal sampling and equal aperture on transmit and receive it follows that two parallel beams are required to keep within the requirements of the sampling theorem. This case is treated experimentally in the next Section.

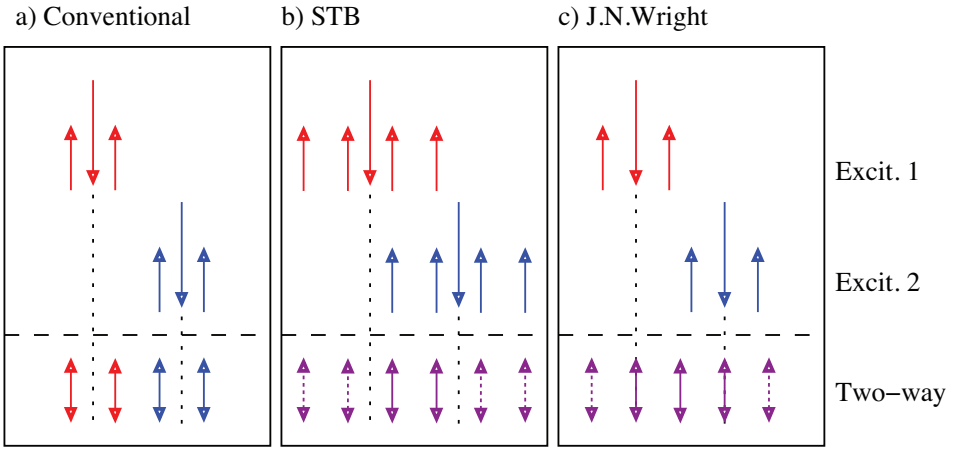

Figure A.5: Sketch of the origin of scan lines.
Part *a)* of the figure shows two transmit beams (pointing down) with 2 parallel receive beams each, pointing up. The resulting scan lines are showed beneath the horizontal dashed line. The vertical dotted line extends the transmit beam direction to make it easier to see the alignment with the two-way beams.
Part *b)* of the figure shows the corresponding STB case. Here 4 parallel receive beams are acquired for each transmitted beam. These are aligned in pairs as shown, yielding the interpolated, synthesized beams showed beneath the dashed line. The solid arrows indicate the receive beams successfully generated from the two shown excitation events, while the dashed arrows represent scan lines that need another transmit event to be complete.
Part *c)* shows the origin of scan lines with the synthetic beam setup proposed by J. N. Wright.

A.4 Compensation Methods

A.4.1 Synthetic Transmit Beams

In Fig. A.5*a)* an example of the conventional parallel beamforming approach is sketched, represented with two transmit beams and their corresponding two parallel receive beams. Beneath the dashed line the resulting 4 scan lines from these two excitations are shown.

Part *b)* of the figure sketches the corresponding practical implementation of the proposed STB method using a linear interpolation filter and two parallel receive beams. Note that twice the number of beamformers are necessary to form the synthetic transmit beams through interpolating the two receive beams at each position using the

two-point linear interpolation filter

$$h(x_i, k) = [1 - w, w] \tag{A.11}$$
$$= [0.75, 0.25] \tag{A.12}$$

for the regularly spaced receive beams shown in Fig. A.5. For a more general receive beam positioning w is found as $w = \frac{x_i - x_k}{x_{k+1} - x_k}$, with reference to Fig. A.4. Note that the STB principle can easily be extended to an arbitrary number of parallel receive beams, only limited by the number of available receive beamformers.

Choosing a linear interpolation filter is the simplest implementation of STB, as only two receive beams has to be steered toward each desired scan line position. The impulse response of the linear interpolation filter is triangular, making it a sinc^2-function in the frequency domain [9]. This means that some of the high-frequency content of the signal will be attenuated, and there will be some noise due to aliasing from the wide transition band. The maximum error will appear for a marginally sampled white-noise process, where the reduction of power without aliasing compared to ideal interpolation is found from

$$P_{err} = 20 \log_{10} \left(\int_{-f_s/2}^{f_s/2} \left(\frac{\sin(\pi f / f_s)}{\pi f / f_s} \right)^2 \mathrm{d}f \right) = -2.2\text{dB} \tag{A.13}$$

where f_s is the sampling frequency and f is the lateral frequency variable.

The error will be lower for a band-limited signal, and is further reduced with oversampling, that is, using a higher density of transmit beams. However this is not wanted as the purpose of parallel beam processing is to obtain a high frame rate, which necessitates as scarce positioning of transmit beams as possible.

Higher order interpolation can be used if the necessary number of beamformers are available. Each scan line requires the same number of beamformers as the number of taps in the interpolation filter. Using an ideal interpolation filter in (A.7) will give perfect reconstruction with no artifacts from parallel processing. Unfortunately this requires an infinitely long interpolation filter, and the same number of beamformers.

A.4.2 Dynamic steering

Most modern (digital) beamformers are using different focusing delays for each depth when receiving, ensuring appropriate geometrical focus. This is called dynamic *focusing*. If the beamformer also updates the steering delays for each depth, this is called dynamic *steering*. Such a beamformer can focus along any line - straight or curved, upon reception.

If the beamformer is capable of such dynamic steering, another intuitive way of compensating for the warping effect is by deliberately offsetting the receive-direction for each depth in the opposite direction of the warping [10]. To make this work well a reasonably accurate beam model must run on the scanner. From Fig. A.2 it can be seen that the Gaussian model presented in Section A.2 can serve this purpose close to

Table A.1: Some common parameters for simulations and experiments.

Parameter	Value
Center frequency f_0	2.5MHz
Focal point	5cm
$f-$number transmit	2.3 in focal point
$f-$number receive	2.3 until the focal point, then increasing
Transmit line spacing	$1 \cdot \lambda f_{\#t}$ in focal point
Display interpolation	RF

the focal depth, where it can be argued that a good image is most important. In other words, offsetting the receive focal direction with the inverse of (A.2) should reduce warping artifacts significantly.

If dynamic steering is not available, a fixed steering offset can be applied to eliminate warping at a desired depth, often chosen as the focal depth. However, this approach might lead to poor performance at other depths.

A.4.3 US patent by J. N. Wright

One version of the preferred embodiment in the US patent of J. N. Wright has been implemented both in simulations and experiments. It uses two parallel receive beams, and the synthetic beams are found by interpolating between these as given by Fig. 3 in the patent [4]. The position of transmit-, receive- and synthetic scan lines are indicated in part *c)* of Fig. A.5.

The synthetic scanlines that align with the transmit *(tx)* beam are made by calculating the average of the two parallel receive *(rx)* beams originating from this transmit event. The synthetic beam halfway between the *tx* beams is calculated as the average between the two nearest *rx* beams, originating from two different *tx* events, as described in the patent. This is the same as running a two-point lateral averaging filter on the received RF data, meaning this method is expected to reduce the lateral resolution of the imaging system.

A.4.4 Simulation- and experimental setup

Using the ultrasound simulation software Field II [5] several approaches to parallel beamforming have been investigated: uncompensated, steering offset in focus, dynamically steered, the J. N. Wright method, and with synthetic transmit beams. Additionally the standard, focus offset, the J. N. Wright method and STB methods have been tested experimentally using a custom GE Vingmed Vivid 7 ultrasound scanner with 4 available beamformers.

The experimental image acquisition uses equivalent settings as for the simulations. Some common settings for all simulations and experiments can be found in Table A.1. The effect of frequency dependent attenuation has not been taken into account in the simulations, but are naturally still present in the experiments.

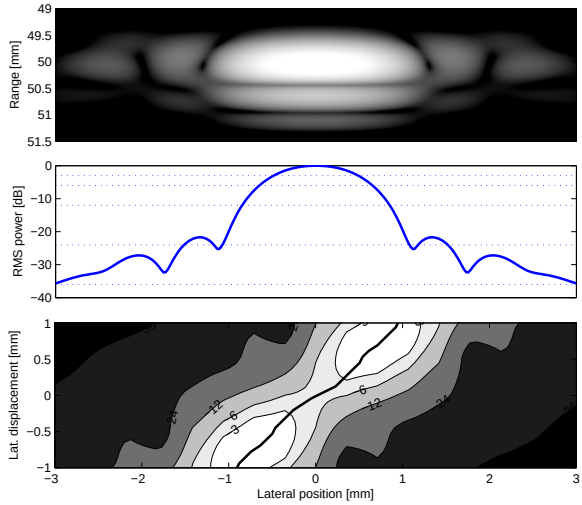

Figure A.6: The top pane shows the image of a point scatterer, a point spread function (PSF). In the middle pane the beam profile (the RMS sum) of this PSF is shown. After obtaining such beam profiles for several lateral positions of the point scatterer the profiles are stacked and displayed in a contour plot in the lower pane. The level of the contours are [-3 -6 -12 -24 -36] dB as is indicated with dashed lines in the middle pane. The thick line indicates the peak position. If the imaging system is completely spatially shift invariant the contour plot should display a set of diagonals.

A.5 Results and Discussion

A display method suitable for showing spatial variance artifacts is shown in Fig. A.6. The top pane of the figure shows a simulated point spread function (PSF), with a corresponding RMS beam profile in the middle pane. By moving the point scatterer laterally and stacking the obtained beam profiles, the contour plot in the bottom pane is obtained. A completely spatially shift invariant imaging system should show a non-varying diagonal structure.

The simulation results are displayed using three such plots each. For all plots the transmit focal depth is 5 cm and both dynamic focus and expanding aperture is used while receiving. The three plots shows the spatial variance resulting from moving a scatterer laterally at a depth of 3, 5 and 7 cm respectively. For a quantitative assessment of all simulation plots please refer to Table A.2.

The reference situation where only one receive beam for each transmit beam is used is shown in Fig. A.7. Note that for all scatterer depths the results are nearly spatially shift invariant, as is seen by the close to invariant diagonals. The nearly shift invariant property can also be seen quantitatively from Table A.2. The right side of the figure shows experimental verification of the spatial variance plots, an image of an ultrasound phantom. In contrast to all the following setups, this simulation and

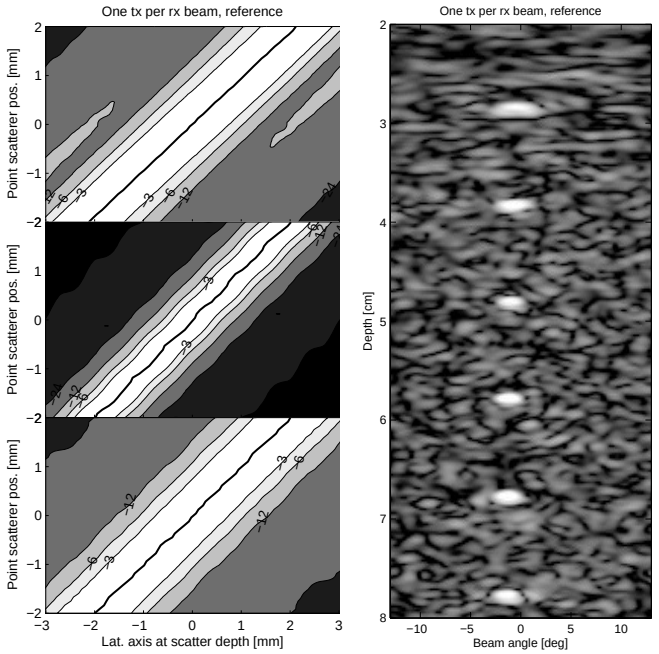

Figure A.7: Reference situation, showing simulated results on the left side and an ultrasound image on the right for validation. The three panes of the simulations correspond to a scatterer depth of 3, 5 and 7 cm respectively. The thick line close to the center of the plot indicates the position of the beam peak value. The phantom image to the right was acquired with an ultrasound scanner using a phased array transducer. The beams are formed in a sector format and are displayed using polar coordinates. The remaining relevant settings are listed in Table A.1, apart from the transmit line spacing, which is $\lambda f_{\#t}/2$ to make the scan line density equal the other simulations. See text for details.

experiment uses a transmit beam spacing of half the Rayleigh criterion, $\lambda f_{\#t}/2$, thus it runs at half the acquisition speed. This is done to give all plots the same scan line density, and can also be seen from (A.10).

Fig. A.8 shows a plot for the case of using two parallel receive beams without any compensation techniques. Note that this results in a considerably more spatially variant imaging system at all depths. This is particularly noticeable around the focal depth. The image to the right displays how these artifacts show up in a recorded image. The lateral gain variation of nearly 5dB (see Table A.2) is particularly noticeable. It is important to recognize that these artifacts are much more prominent in a dynamic image. In the electronic version of this document these artifacts can be seen qualitatively in the left movie of Fig. A.9, showing the bicuspidal valve.

Fig. A.10 was made with the proposed method, STB. Compared to the uncompensated plots and image in Fig. A.8 it is evident that the imaging is more shift invariant

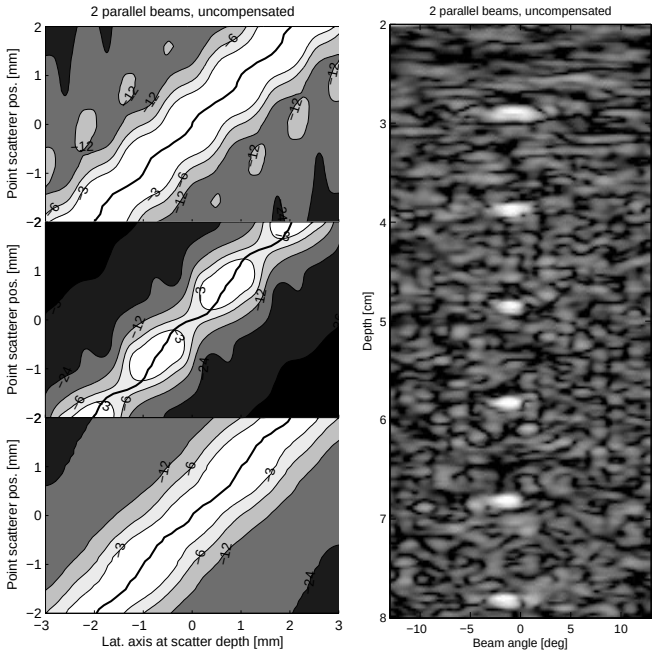

Figure A.8: Imaging using 2 parallel receive beams, without any type of compensation. Note the evident lack of spatial invariance, especially with the scatterer at the focal depth (middle pane). This can also be seen from the ultrasound image to the right, where vertical stripes are apparent in a region around the focal depth of 5 cm.

when STB is applied. The contour plots are better than the uncompensated version at all depths, and the image quality resembles that of the reference situation in Fig. A.7. This can be seen from the right movie in Fig. A.9, which is made from offline processing of the same data set as the left movie. Note that this compensation method does not compromise on spatial resolution, as is seen in Table A.2.

The method proposed by J. N. Wright was found to perform best when the *rx*-beams were shifted further away from the *tx* direction, in the same manner as to compensate for the warping effect at the focal depth, as described in the section on *Dynamic steering*. The additional shift corresponded to a fourth of the receive line spacing. Results from simulations and experiments with these settings are displayed in Fig. A.11, and numerical results from the simulations can be found in Table A.2. Comparing these figures with those of the STB method in Fig. A.10, the J. N. Wright method is seen to display nearly as good spatial shift invariance as the STB method. However, from the numerical results this method it is seen to give a 15% reduction in lateral resolution when compared to the STB method.

If dynamic steering is not available, the warping can only be fully compensated for at one specific depth. Figure A.12 shows the results from warp-compensating at the

Table A.2: Numerical results from comparison of parallel beamforming techniques.

Method	Depth	Mean beam width [mm]	Width var.	Gain var. [dB]	Offset
Reference,					
	30 mm	2	3%	0.3	2%
	50 mm	1.2	15%	0.64	11%
	70 mm	2.1	7%	0.32	5%
Uncomp.,					
	30 mm	2	5%	0.32	11%
	50 mm	1.3	37%	4.8	29%
	70 mm	2.1	18%	1.4	13%
Focus comp.,					
	30 mm	2.1	76%	0.89	50%
	50 mm	1.2	13%	0.76	12%
	70 mm	2.3	115%	3.66	48%
Dyn. steered,					
	30 mm	2	4%	0.48	15%
	50 mm	1.2	13%	0.72	11%
	70 mm	2.1	12%	0.92	9%
STB,					
	30 mm	1.9	2%	0.29	6%
	50 mm	1.3	16%	1.97	16%
	70 mm	2.1	10%	0.79	6%
J.N.Wright method,					
	30 mm	2	7%	0.91	23%
	50 mm	1.5	15%	2.12	16%
	70 mm	2.4	18%	1.06	13%
Undersampled,					
	30 mm	2.2	25%	0.51	9%
	50 mm	1.6	86%	7.09	89%
	70 mm	2.6	57%	3.49	41%

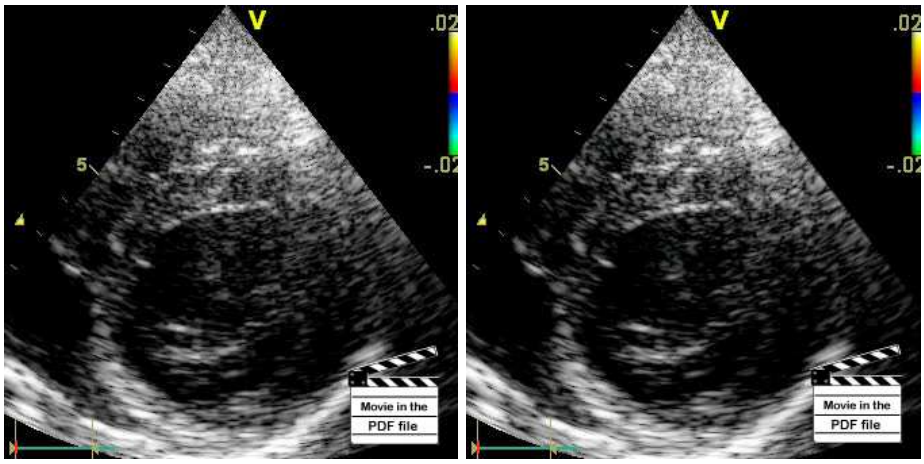

Figure A.9: Left: movie showing the bicuspidal valve, acquired with 2 parallel receive beams without any compensation for parallel beam artifacts. Right: the same raw data processed with STB. The electronic version of this document, containing the above movies, can be found at http://urn.kb.se/resolve?urn=urn:nbn:no:ntnu:diva-5937.

focal depth. The middle left pane shows that offsetting the steering angle to eliminate warping at the focal depth successfully eliminates warping in focus. However the spatial invariance is significantly reduced below and above the focal point.

The left pane of Fig. A.13 shows simulated results from using dynamic steering to compensate for warping at all depths. Unfortunately no experimental results are available due to limitations in the available ultrasound scanner. When the steering compensation is done dynamically, warping is eliminated at all depths up until the accuracy of the Gaussian beam approximation. Note that the skewing artifact is left uncompensated with this approach. This is particularly noticeable in the top pane where the spatial invariance is poor despite the steering compensation efforts.

For completeness the right pane of Fig. A.13 shows the simplest option when it comes to increasing the acquisition rate, simply decreasing the scan line density. From the two bottom panes it is seen that this approach suffers from under-sampling. It important to remember that the sampling criterion has to be credited at both transmit, receive and two-way. Even if this simple method has sufficient sampling on transmit and receive, the two-way situation is under-sampled.

Some numerical results from the simulation study are summarized in Table A.2. The results of the first two columns are calculated with normalized beams, that is, the peak value is zero for all lateral scatter positions. The first column lists the mean -6dB beam width. The “Width var.” and “Gain var.” columns quantifies the difference between the min. and max. -6dB beam width and the peak gain difference respectively. The “Offset” column is computed to give a measure of the meandering movement of the peak position. It is given as the ratio of the two-sided lateral peak position error and the mean beam width at each depth.

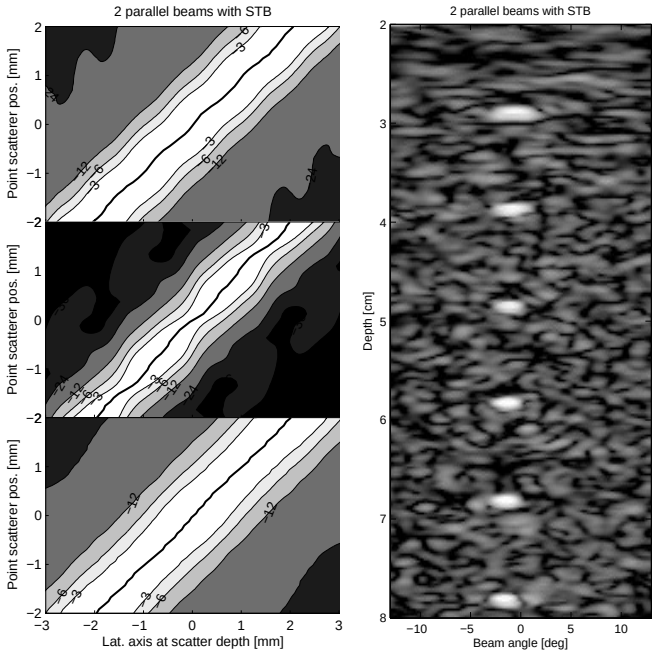

Figure A.10: Much of the artifacts originating from parallel receive beams can be eliminated by using STB imaging, as is shown here. Note the difference from the uncompensated images in Fig. A.8. Both experimental images were made with the same parameters and the same transmit- and scan line density. They differ only in the number of beamformers used. The axes show depth and angle increment, where the center line is chosen as zero degrees. Note how the STB image shows no signs of the easily noticeable vertical stripes of the image without STB. Also note that there is still some ripple left at the focal depth of the contour plot. This is probably caused by the non-ideal linear interpolation filter used.

Investigating the first column of the Table, it is seen that the mean beam width of the J. N. Wright method is slightly larger than for the other imaging methods. This can be contributed to the lateral filtering performed in this method. Apart from that, the mean beam width at at each depth is quite constant for each imaging method, with the exception of the undersampled method. Note that this is the case even when steering compensation methods are applied. Using a Gaussian beam profile approximation it can easily be shown that this is as expected. Looking at mean beam widths does not tell anything about the shift invariance property of the methods. This is better seen in the next column, displaying the difference between the maximum and minimum beam width as the scatterer is moved laterally. It can here be observed that all methods, except for the focus compensation method, perform best before and after the focal depth. This is due to the wider transmit beam at these depths. At the focal depth

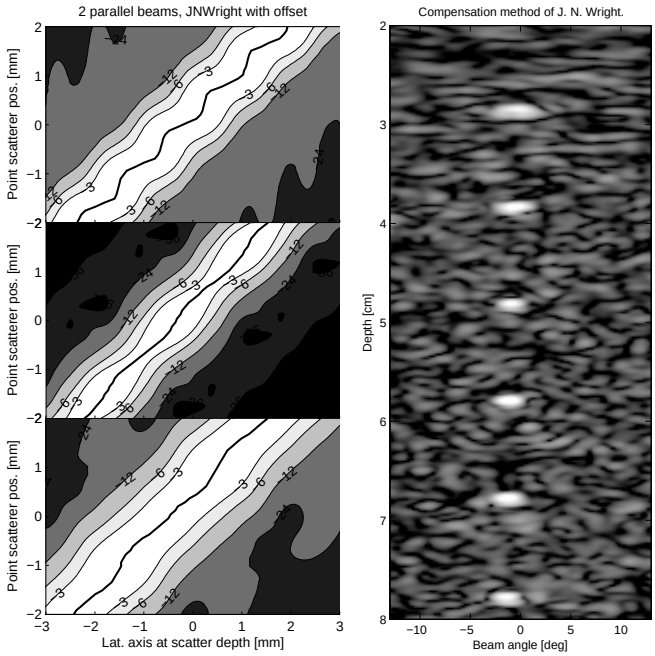

Figure A.11: The J. N. Wright method with a static receive beam offset. No easily noticeable vertical stripes can be seen in the image. The image is however more blurred than the corresponding STB image. Also notice the more variable peak position (thick solid line) at all depths compared to STB.

the -6dB beam width vary with 37% when no compensation is done. When applying either dynamic steering, the J. N. Wright method, or STB, all of which have similar performance here, the width variation is greatly reduced to around 15%, the same as in the reference situation. Looking at the next column, the gain variation, the dynamic steering method performs best, reducing the variation from 4.88dB uncompensated to 0.72dB at focal depth. That is only slightly higher than the reference situation and then as good as one can expect it to be with the applied beam density. An interesting number is the 2dB gain variation at the focal depth for the STB method. This variation is most likely due to linear interpolation of marginally sampled data. The applied two point linear interpolation filter is not sufficient to fully correct for the beam warping, hence some under-sampling artifacts remains. This can also be seen from the STB offset at focal depth, which is a bit larger than the dynamic steering offset. Higher order interpolation would be required to correct for this.

In the remaining column, tabulating the peak value offset from the expected position, it is interesting to notice that the STB method performs better than dynamic steering both before and after focus. This can probably be contributed to two things. Firstly the ability of the STB method to correct for skewness in the beam profiles,

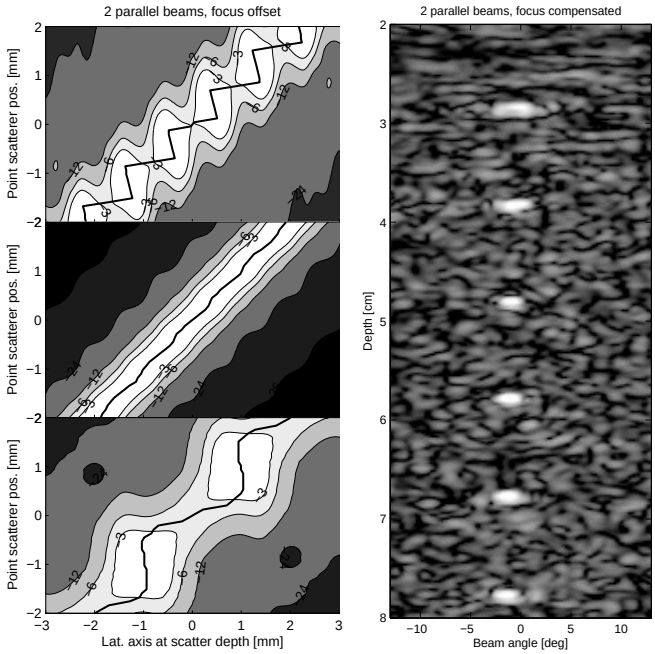

Figure A.12: Here the results from warp compensation by statically offsetting the receive beam is shown. The offset is calculated to eliminate warping at the focal depth, resulting in poor performance at other depths.

which will be a prominent cause of artifacts in these regions. Secondly the Gaussian beam approximation used for estimating beam warping will be poor at depths outside the focal zone, causing the dynamic steering method to fail at these depths. The STB method will correct for warping at all depths independent of beam approximations. The J. N. Wright method is seen to yield results not quite as good as the STB method outside the focal depth.

A.6 Concluding Remarks

From the results presented above it is clear that straightforward parallel beamforming reduces the spatial shift invariance of an ultrasound imaging system. Some compensation approaches have been investigated, and the proposed method of using synthetic transmit beams seems to give a more spatial shift invariant imaging system, with the benefit of increased acquisition rate. However this comes at the cost of additional beamformers.

Dynamic steering also seems like a promising technique, even though it does not compensate for all parallel beam artifacts as the STB method does. The benefit of this technique over STB is that the same number of scan lines as available beamformers is

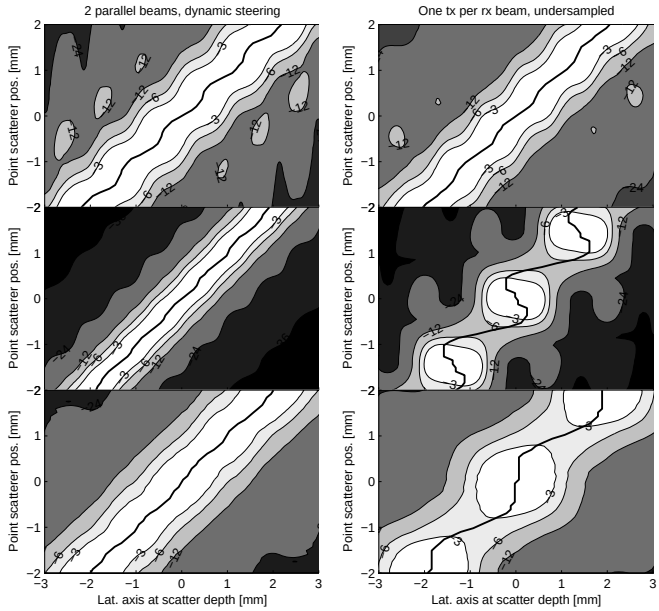

Figure A.13: Left column: dynamic steering is used to compensate for warping at all depths. Compare this to the results from compensating at the focal depth only, shown in Fig. A.12. No experimental results are available due to limitations in the available ultrasound hardware. Right column: The easiest way to increase the acquisition rate is simply to decrease the scan line density. Here the result from using the same transmit beam density as in the other plots is shown, but with only one parallel beam. This results in two-way under-sampling, as can clearly be seen from the middle and bottom pane.

obtained.

Note that significantly less spatial variance from parallel receive beam operation can be obtained by increasing the transmit beam density and/or increasing the transmit f-number. The penalty for doing so is decreased acquisition speed in the case of increased transmit beam density. The main drawback of increasing the transmit f-number is reduced penetration. Additionally it will give a wider transmit focus, giving poorer resolution.

It is worth noting that different underlying phenomena contribute to the artifacts at increasing depth. In the region close to the transducer the skewing effect is the dominant artifact. In the focal region the warping effect dominates, while deeper in the image both effects contribute.

References

[1] O. T. von Ramm, S. W. Smith, and H. G. Pavy, "High-speed ultrasound volumetric imaging system – part ii: Parallel processing and image display," *IEEE Transactions on Ultrasonics, Ferroelectrics, and Frequency Control*, vol. 38, March 1991.

[2] D. P. Shattuck, M. D. Weinshenker, S. W. Smith, and O. T. von Ramm, "Explososcan: A parallel processing technique for high speed ultrasound imaging with linear phased arrays," *Journal of the Acoustical Society of America*, vol. 75, no. 4, pp. 1273–1282, 1984.

[3] L. J. Augustine, "High resolution multiline ultrasonic beamformer." United States Patent 4.644.795, 1987.

[4] N. Wright, S. H. Maslak, D. J. Finger, and A. Gee, "Method and apparatus for coherent image formation." United States Patent 5.623.928, 1997.

[5] J. A. Jensen, "Field: A program for simulating ultrasound systems," *Medical & Biological Engineering & Computing*, vol. 34, pp. 351–353, 1996.

[6] J. N. Wright, *Image formation in diagnostic ultrasound*. IEEE international ultrasonics symposium short course, 1997.

[7] M. Kowałski, T. Kukulski, F. Jamal, J. D'Hooge, F. Weidemann, F. Rademakers, B. Bijnens, L. Hatle, and G. R. Sutherland, "Can natural strain and strain rate quantify regional myocardial deformation? a study in healthy subjects," *Ultrasound in Med. & Biol.*, vol. 27, no. 8, pp. 1087–1097, 2001.

[8] T. L. Szabo, *Diagnostic ultrasound imaging inside out*. Elsevier academic press, 2004.

[9] J. G. Proakis and D. G. Manolakis, *Digital Signal Processing. Principles, Algorithms, and Applications*. London: Prentice Hall, third ed., 1996.

[10] K. E. Thiele and A. Brauch, *Method and apparatus for dynamically steering ultrasonic phased arrays*. United States Patent 5.322.068, 1994.

Paper B

Reducing Color Flow Artifacts caused by Parallel Beam Acquisition

Torbjørn Hergum[1], Tore Bjåstad[1], Lasse Løvstakken[1], Kjell Kristoffersen[2] and Hans Torp[1]
[1]Department of Circulation and Medical Imaging, NTNU, Trondheim, Norway
[2]GE Vingmed Ultrasound, Horten, Norway

Abstract

In color flow imaging for medical diagnosis the inherent trade-off between frame rate and image quality may often lead to suboptimal images. Parallel receive beamforming is used to help overcome this problem, but this introduces artifacts in the images. In addition to the parallel beamforming artifacts found in B-mode imaging, we have found that a difference in curvature of transmit and receive beams gives a bias in the Doppler velocity estimates. This bias causes a discontinuity in the velocity estimates in color flow images.

In this work we have shown that interpolation of the autocorrelation estimates obtained from overlapping receive-beams can reduce these artifacts significantly. Since the auto-correlation function varies quite slowly the beams can be acquired with a significant time difference, for instance across interleaving groups or across scan planes in a 3D scan.

We have shown that a high frame rate of color flow images can be maintained with parallel beam acquisition with minimal deterioration of the image quality.

Submitted to *IEEE Transactions on UFFC*

B.1 Introduction

Parallel receive beams are used to increase the frame rate of ultrasound imaging[1, 2]. This will introduce artifacts in the images due to misalignment of the transmit- and receive-beams. A method using synthetic transmit beams (STB) has previously been shown to reduce this problem in B-mode imaging by aligning each receive-beam with a synthetic transmit beam [3]. However, the additional time lag between neighboring beams for Doppler packet acquisition may cause phase cancellation [4] and therefore a failed reconstruction of the synthetic transmit beams.

In addition to the artifacts of parallel beamforming in B-mode imaging, we have found that color flow imaging has an additional parallel beam artifact. The measured Doppler shift is dependent on the angle between the transmit/receive beams and the direction of the blood flow [5], but for parallel beams the curved wavefronts of a focused transmit beam will cause a changing angle with the blood flow, depending on the position of the received beam. This causes a discontinuity in the velocity estimates between groups of beams from different transmit events.

We have extended the ideas of synthetic transmit beamforming to reduce artifacts from parallel beams also for images based on Doppler processing, like Color Flow imaging, power-Doppler and B-Flow.

We will firstly describe and quantify the origins of parallel beam artifacts in color flow imaging, before showing why the STB method fails for fast blood flow or long time delays between samples. Then we will introduce STB on the auto-correlation function, and lastly show *in vivo* vascular and cardiac imaging examples.

B.2 Origin of artifacts

In B-mode imaging the two major causes of artifacts due to parallel beam acquisition are *skewing* and *warping* [3]. *Skewing* is the distortion of the two-way beam profile caused by misalignment of the transmit- and receive-beams. This misalignment also causes *warping*, where the receive-beam is pulled towards the center of the transmit-beam, such that the received signals does not originate from the apparent direction of the receive-beam.

Color flow, B-flow and power-Doppler images are usually made from the power (lag 0) and angle of the auto-correlation function with lag 1. The auto-correlation function from a sampled ultrasound signal $z(k)$ is $R(m) = \langle z(k+m)z(k)^* \rangle$, where m is the lag. It can be estimated from a packet of N samples by [5]

$$R_N(m) = \frac{1}{N} \sum_{k=1}^{N-m} z(k+m)z(k)^*. \tag{B.1}$$

In addition to *warping* and *skewing* Doppler imaging methods like Color Flow shows a parallel beam artifact caused by the curvature of the focused wavefront. The Doppler shift is recorded along the vector sum of the transmit- and receive-beam directions, the two-way normal, as is described in chapter 9 of [5]. The transmit beam

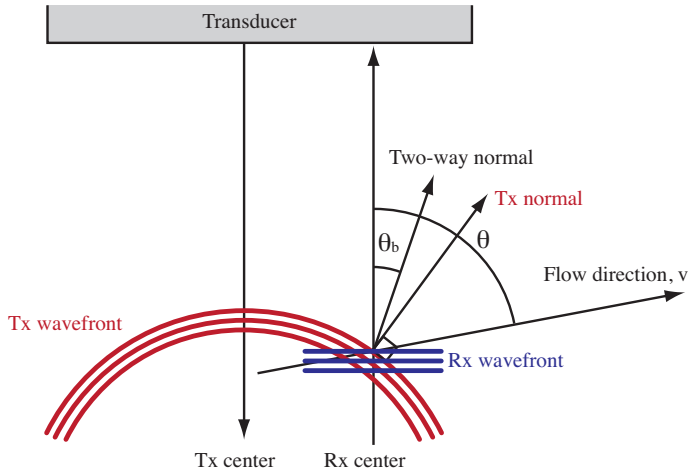

Figure B.1: Curved wave fronts above and below the focal point causes a varying angle between the flow and the receive-beams, depending on how far the receive-beam is steered off the axis of the transmitted beam. This is seen in color flow images as abrupt changes in velocity estimates from one group of received beams to the next.

is typically wide to fit all the parallel beams, and focused to increase the signal to noise ratio. Away from the focal point this makes the wavefront wide and curved. The receive-beam is typically dynamically focused and narrower than the transmit-beam, so it will have a different curvature, or not be curved at all, and overlap with a small part of the transmitted beam. This is sketched in Fig. B.1. When the curvature is not taken into account the expected Doppler shift f_d is

$$f_d = \frac{2vf_0}{c}\cos(\theta) \tag{B.2}$$

where v is the velocity of the blood, f_0 is the transmit frequency, c the speed of sound and θ the angle between the beam and the direction of the flow. The actual Doppler shift will be biased due to θ_b, shown in Fig. B.1, and give

$$f_b = \frac{2vf_0}{c}\cos(\theta - \theta_b). \tag{B.3}$$

We call it the parallel beam *Doppler bias* artifact. The relative difference between the expected and the measured Doppler shift is

$$\frac{f_b - f_d}{f_d} = \frac{\cos(\theta - \theta_b) - \cos(\theta)}{\cos(\theta)} \tag{B.4}$$

which is plotted for relevant combinations of θ and θ_b in Fig. B.2. From the figure we expect the Doppler bias to be most visible when the angle between the wave front normal and the flow direction is large.

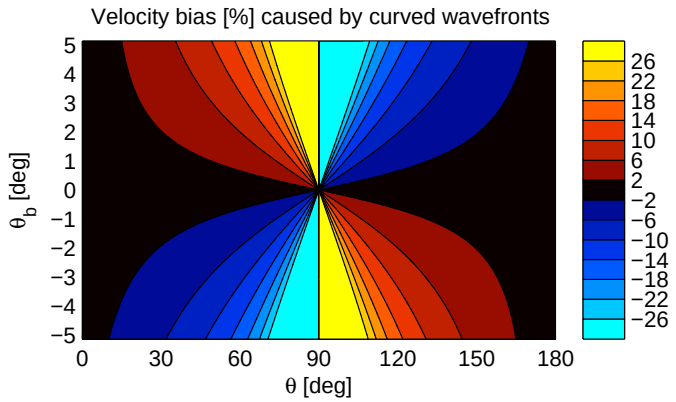

Figure B.2: Relative Doppler bias of equation (B.4), which is caused by curved, wide wavefronts on transmission and focused, planar wavefronts on reception. The angles θ and θ_b are indicated in Fig. B.1. The figure is limited to showing $\pm 30\%$ Doppler bias to avoid showing the asymtote near $\cos(\theta) = 0$.

The simple geometrical model with spherical wavefronts shown in Fig. B.1 is only valid far from the focal point. In reality, the wavefronts in the focal point is approximately planar, meaning that θ_b will approach zero when the diffracting effects overcomes the geometrical focusing effect [5]. We have investigated the depth-dependence of the beam curvature further by computer simulations using Field II [6], with parameters equaling the in vivo carotid images in the Results-section. The transmit pulse and estimated curvature is shown in Fig. B.3. Curvature was estimated from the phase variation laterally across the simulated transmit pulse at each depth.

Since the Doppler bias is symmetric about the center of the transmit beam, but with opposite signs, it will cause the velocity estimates to change abruptly between two neighboring beams from different transmit events. This is shown in Fig. B.4, which shows an *in vivo* example of the carotid artery without any lateral smoothing. The vertical discontinuities from transition between groups of parallel beams are clearly visible, particularly in the regions with velocity aliasing. This is also shown in the bottom part of the figure, where the deviation from the average velocity along the center of the carotid artery is plotted. Ideally this should be a smooth curve near zero.

B.2.1 Synthetic Transmit Beams applied to Color Flow

We have previously proposed *Synthetic Transmit Beams (STB)* as a method to reduce artifacts from parallel beams in B-mode imaging by interpolating between overlapping receive-beams from different transmit events[3]. The overlapping beams must sum coherently for the interpolation to work. Constructive interference happens when the

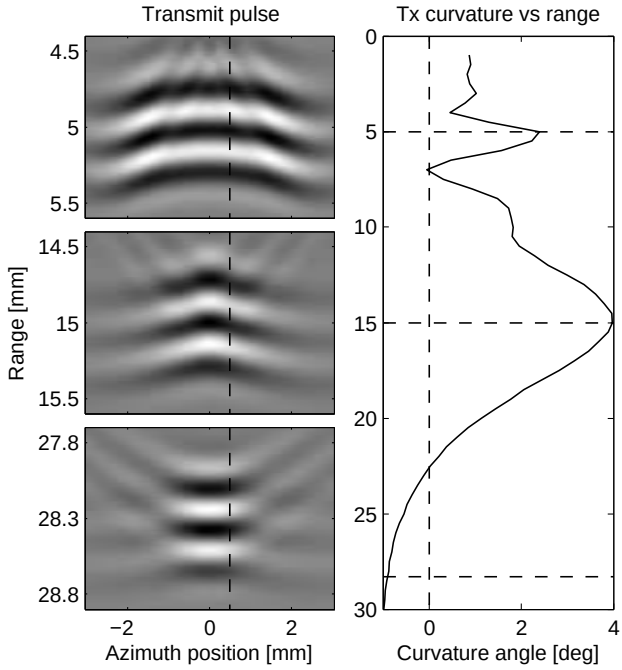

Figure B.3: Computer simulation of the curvature of transmit wavefronts. The left panes show the transmitted pulse at three depths: in the nearfield, at the position of peak curvature, and at the focal point. The dashed line indicates the position of the most steered receive beam. The estimated curvature along this line is plotted in the right pane. Horizontal dashed lines indicates the position of the three pulses shown. The simulation parameters corresponds to the carotid *in vivo* parameters of Table B.1

displacement between received pulses is less than $\lambda/8$, that is, when

$$v\tau = \Delta r \leq \lambda/8 = c/(8f_0) \tag{B.5}$$

where τ is the time lag between acquisition of the overlapping pulses. In comparison the Nyquist sampling velocity for Doppler imaging is $v_n = c/2f_0\Delta t$ where Δt is the time between pulses. Beam interleaving techniques [7] can be used when acquiring overlapping beams, by ensuring that the maximum PRF ultimately given by the scan depth is used to acquire the image.

Fig. B.5 indicates the position of a number of transmit beams (arrows pointing down) and receive beams (arrows pointing up). STB processing is done by interpolating overlapping receive beams to give the signal $\tilde{S}(x_r)$,

$$\tilde{S}(x_r) = \sum_k h(x_r, k) S_k(x_r), \tag{B.6}$$

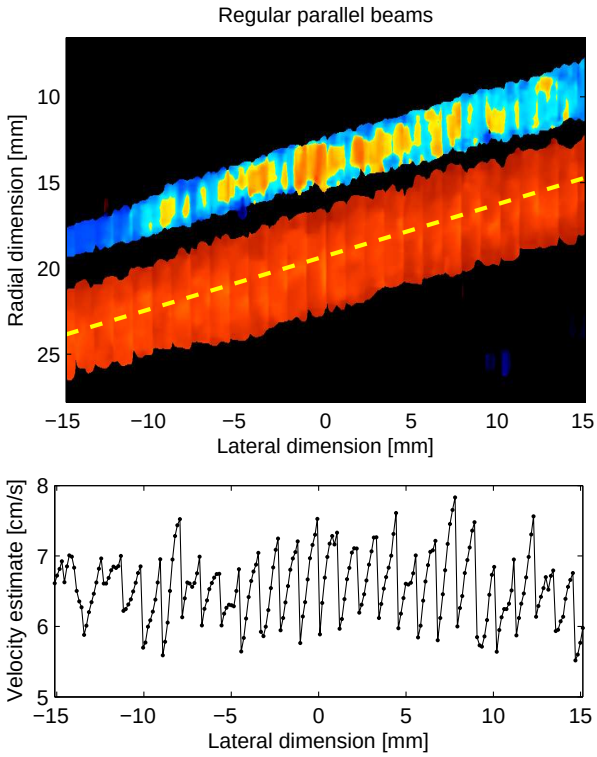

Figure B.4: Top: Doppler bias from experimental data. Note the vertical discontinuities of the velocity estimates, which appears at the transitions between beams from different transmit events. Bottom: estimated blood velocity from the central part of the artery, along the dashed line, in the above image.

where $h(x_r, k)$ is an interpolation filter and $S_k(x_r)$ is the signal received from transmitting towards direction k and receiving from direction r [3]. A linear interpolation filter will be used to illustrate the principle, because it only requires two overlapping receive beams which maximizes the frame rate. The interpolation filter has weights w and $(1 - w)$ where w is inversely proportional to the distance from the transmit beam, found as $w = \frac{x_r - x_k}{x_{k+1} - x_k}$. As an example a signal $\tilde{S}_1$ is made from the pair of beams a and b, as indicated in Fig. B.5. Just like with B-mode images this limits the artifacts caused by *warping* and *skewing* [3]. Several such signals are used to estimate the auto-correlation function. The cross correlation between two such STB processed

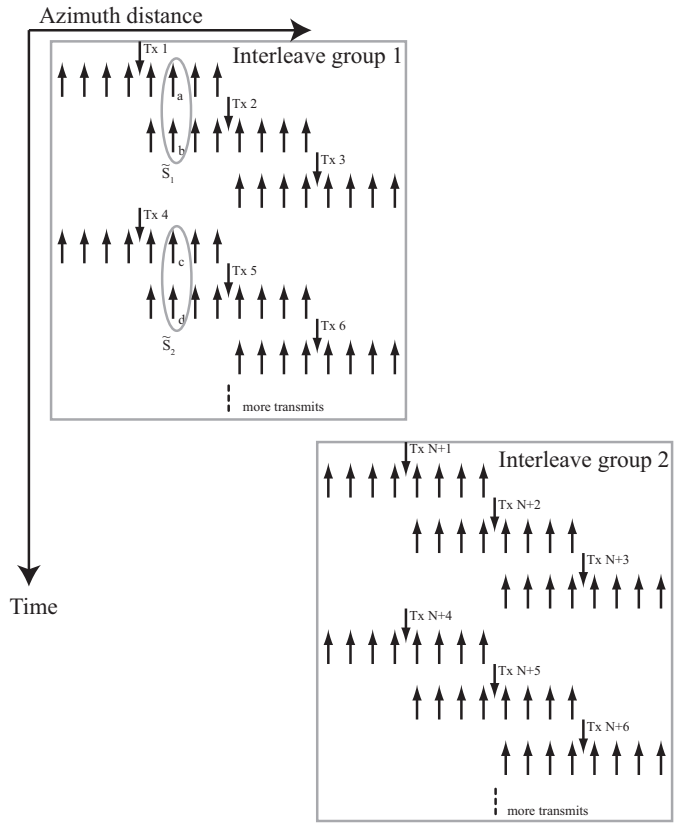

Figure B.5: Illustration of the scan sequence for color flow imaging, with overlapping beams as required by STB processing and two interleave groups. Only the first two samples of each packet of N pulses are drawn. See the text for further details.

signals, $\tilde{S}_1$ and $\tilde{S}_2$, is

$$\tilde{S}_1 = wS_a + (1-w)S_b \tag{B.7}$$

$$\tilde{S}_2 = wS_c + (1-w)S_d \tag{B.8}$$

$$\begin{aligned}\langle \tilde{S}_1 \tilde{S}_2^* \rangle &= w^2 \langle S_a S_c^* \rangle + w(1-w)\langle S_a S_d^* \rangle \\ &\quad + (1-w)w\langle S_b S_c^* \rangle + (1-w)^2 \langle S_b S_d^* \rangle\end{aligned} \tag{B.9}$$

where the beams a, b, c and d are all received from the same direction, but from different transmit events as indicated in Fig. B.5.

The received Doppler signal stays correlated only for a brief period of time, depending on the transit time of the scatterers passing through the sample volume. When the acquisition time between two overlapping beams used to estimate the auto-correlation function is long, too many of the scatterers inside the sample volume is replaced, and

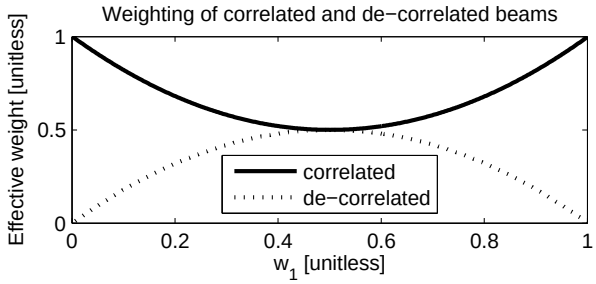

Figure B.6: Plotting the relative weighting of correlated content versus uncorrelated content for coherent STB processing of samples acquired with a large time delay.

the estimate can not reconstruct the auto-correlation function. This can happen for instance across interleave groups, as when the receive beams from *Tx 3* is combined with the receive beams from *Tx N+1* in Fig. B.5.

In these situations the two cross-terms in the middle of (B.9) include terms with zero expected correlation, meaning they will only contribute with white noise. The weighting of the two correlated terms versus the two un-correlated terms changes depending on the distance from the position of the transmit beam. Fig. B.6 plots these weights, $w^2 + (1-w)^2$ versus $2w(1-w)$, showing that the de-correlated terms contribute more with increasing distance to the transmit beams. This means that in the case of a significant time lag between samples the reconstruction will be best near the transmit beams and worst in the middle between them, reducing the spatial shift invariance of the imaging system.

The Doppler bias varies from beam to beam in a non-linear manner, as is seen from Fig. B.2. This means that it can not be removed entirely by STB using linear interpolation. However, as the bottom part of Fig. B.4 indicates, the Doppler bias of the STB-interpolated beams have opposite signs so the bias will be reduced. This will be shown later.

B.2.2 Incoherent STB

Since color flow images are made from the auto-correlation function, as is explained above, what would happen if we perform the STB interpolation on the auto-correlation estimate instead of on the IQ data? When the strict sampling requirements of (B.5) is broken, the interpolation between IQ samples can give arbitrary results, as is illustrated in the top part of Fig. B.7. This is because IQ data contains *absolute phase* information. The auto-correlation estimates, on the other hand, contains only the *phase change* between successive samples. Two estimates of the auto-correlation function obtained from overlapping beams with a large time difference will therefore depend only on the hemodynamic conditions. This is illustrated in the bottom part of Fig. B.7.

With this in mind we suggest to perform the STB interpolation on the auto-

correlation estimates instead of on IQ data. This will remove the cross-terms of (B.9) which only contributes white noise when the time delay is longer than specified in (B.5). Also, instead of using linear interpolation on the amplitude data we use linear interpolation of the second order correlation estimates.

One auto-correlation estimate is calculated from each packet, and the synthetic auto-correlation estimate $\tilde{R}$ is found by interpolating between the estimates originating from the same spatial position, but from different transmit events:

$$\tilde{R}(x_i) = \sum_k h(x_i, k) R(k) \tag{B.10}$$

$$= wR_1 + (1 - w)R_2 \tag{B.11}$$

with the same linear interpolation filter as for (B.6). We call this *incoherent STB*, as the method neglects absolute phase, in contrast to *coherent STB* when it is performed on IQ data [8]. With constant hemodynamics there is no lateral variation caused by combinations of differently correlated signals as for coherent STB, so incoherent STB is expected to be more spatially shift invariant.

There will however remain some lateral variation due to the different signal to noise ratio of the acquired data. Ideally coherent STB will reconstruct this, but the two-tap linear interpolation filter leaves some things to be desired when compared to the infinite-tap ideal interpolation filter. This is an inherent problem of all practical parallel beam processing methods when more than two parallel beams is considered.

B.3 Results

To test the influence of PRF and interleaving on the two STB approaches we have acquired two sets of ultrasound images using a GE Vingmed E9 (Vingmed, Horten, Norway) ultrasound scanner. One set of images shows the common carotid artery and the internal jugular vein, where the acquisition is interleaved to maximize the frame rate and obtain the desired Nyquist velocity. Secondly a set of cardiac images are acquired, but in this case the scan depth and desired Nyquist velocity were such that no beam interleaving could be applied.

For both cases the same raw IQ data is processed to get both coherent STB images, incoherent STB images and standard parallel beam images. This means that all differences are due to post-processing and not differences in acquisition.

B.3.1 *In vivo*: Linear array imaging

Fig. B.8 shows the power and velocity estimates of *in vivo* color flow images. The most relevant settings can be found in Table B.1. Cross correlation between neighbouring beams have previously been shown to give a good measure of parallel beam artifacts [9, 10], so the cross correlation between the $R(0)$ estimates of neighbouring beams is shown beneath the power images, and similarly the cross correlation between $R(1)$ estimates are shown beneath the velocity images. To make the correlation estimates less noisy the cross correlation plots are made from the raw data of the whole cine

loop, which consist of 44 frames. Note the differences in parallel beam artifacts, and the differences in beam-to-beam correlation between groups of parallel beams. There are four interleave groups, with transitions at [-7, 0, 7]mm, but only two interleave groups are shown in the cropped images.

The velocity from the center of the artery shown in Fig. B.8 is estimated in the same manner as the example in Fig. B.4. We assume that the velocity is constant along the center of the artery, so that we can estimate the Doppler bias by calculating the deviation from the mean velocity. This deviation is shown in Fig. B.9. Notice the discontinuities in the bias at the transition between beams from different transmit events when regular parallel beams are used, and compare this to the two other approaches. The relative change in velocity at these discontinuities are shown in Fig. B.10. The source data for these plots are extracted from the center of the carotid artery and averaged over 7 frames. For the beams where the distance to the center of the artery is between 15 and 19mm regular parallel beams had a mean bias and standard deviation of $19.9 \pm 3.0\%$, coherent STB showed a deviation of $3.8 \pm 2.3\%$ and incoherent STB had the lowest deviation at $2.9 \pm 1.5\%$.

B.3.2 Computer simulations

A computer simulation closely resembling the *in vivo* imaging in the previous section was set up using Field II [6], and matching the linear array parameters from Table B.1. The carotid artery was modelled as a straight three-dimensional tube filled with random point scatterers moving at a constant velocity. Just like the in vivo images, the inclination of the tube was set to 16°. The velocity estimates from one group of parallel beams was calculated in $N = 20$ realizations of the simulation, and the Doppler bias was calculated as the deviation from the mean value in the same way as for the in vivo images above. The uncertainty of the estimated bias was calculated as $\sigma/\sqrt{N}$, which is shown together with the bias estimates in Fig. B.11. σ is the standard deviation. The results were averaged over the central 1.1cm of the artery.

Notice that the maximum Doppler bias is present for the outermost beams. The average curvature between 15mm and 19mm depth was found from simulations to be 3.0°. The Doppler bias at beam 8 is $9.7 \pm 4.2\%$. Assuming a flat receive-beam, the pulse-echo curvature θ_b is $3.0°/2$. The *in vivo* angle θ between the beams and the flow is estimated to be 16°, which according to (B.4) should give an average Doppler bias of 9.1% for the outermost receive beam from 15 to 19mm depth.

B.3.3 *In vivo*: Phased Array Imaging

An M5S phased array probe (GE Vingmed Ultrasound, Horten, Norway) was used to image the left ventricle of a healthy volunteer. The resulting power- and velocity-images from the three parallel beam methods are shown in Fig. B.12. The cross correlation is shown below each image in the same way as for the linear images above, and relevant acquisition settings can be found in Table B.1.

There are no interleave groups in these images, and the hemodynamics are changing rapidly. Please notice the artifacts at the transitions between groups of parallel beams.

Table B.1: Settings for *in vivo* images.

Linear array parameters	Value
Center frequency f_0	5.9MHz
Tx $f-$number	5
Rx $f-$number	dynamic, min. 1.4
Tx focal depth	2.8 cm
Pulse length	2.5 cycles
Packet size	12
Parallel beams acquired	16
Parallel beams synthesized	8
Pulse repetition frequency	2000
Lateral smoothing	none
Radial smoothing (R0)	none
Radial smoothing (R1)	1.1mm
Phased array parameters	
Center frequency f_0	2.5MHz
Tx $f-$number	18
Rx $f-$number	dynamic, min. 1.5
Tx focal depth	14 cm
Pulse length	2.5 cycles
Packet size	8
Parallel beams acquired	16
Parallel beams synthesized	8
Pulse repetition frequency	4000
Radial smoothing	1.5mm
Lateral smoothing	none

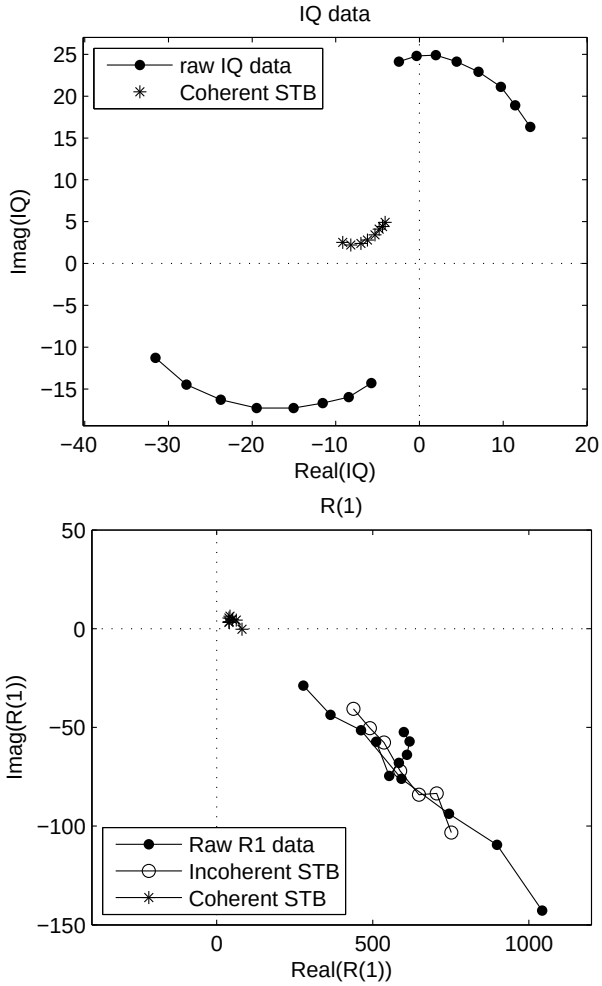

Figure B.7: Top: two packets of IQ data recorded from a beating heart, showing the signal spinning in the complex plane. These two packets are combined with coherent STB. Due to the large time delay between the combined samples they are summed with nearly opposite phase, to give the result marked $*$. Bottom: Auto-correlation with lag 1, R(1), of the data in the top figure. The velocity is estimated as $\angle R(1)$, which is seen to be nearly constant. Nevertheless, most of R(1) from the coherent STB samples, marked $*$, have a significantly different angle. If STB is performed incoherently on R(1) we obtain the signals marked $\circ$, seen to have the same angle as the original data.

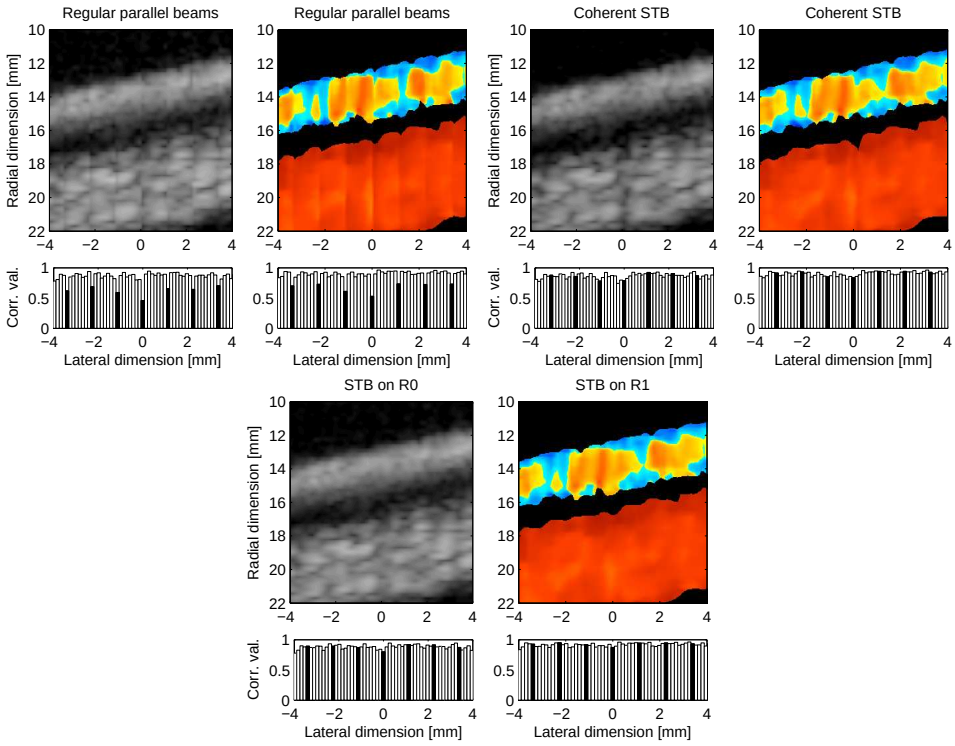

Figure B.8: Power and Color flow images of the common carotid artery and jugular vein. The top left pane shows standard parallel beam processing, the top right pane is treated with coherent STB, and the bottom pane shows incoherent STB, that is, the STB interpolation is performed on the auto-correlation function. There is one interleave group transition at $0mm$. The correlation values between neighboring beams are shown below each figure.

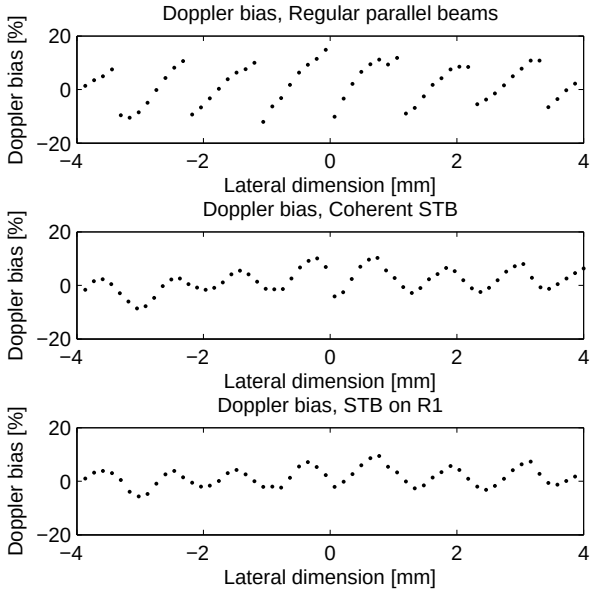

Figure B.9: The Doppler bias extracted from the center of the artery in Fig. B.8. Each dot represents the bias from one beam at the center of the artery. The bias is estimated as the deviation from the mean value, which assumes that the velocity is constant in the center of the artery.

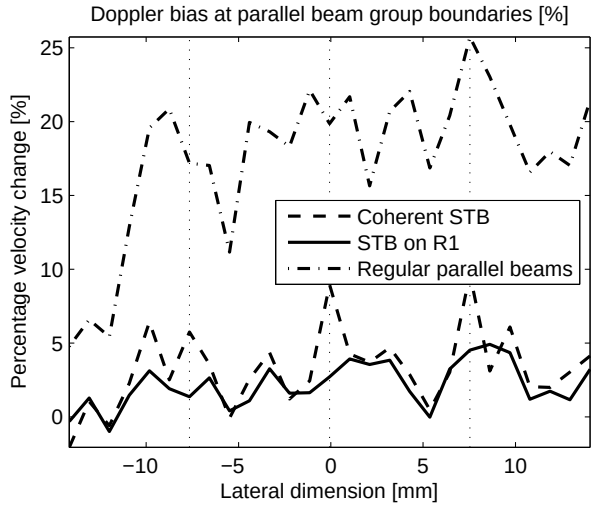

Figure B.10: The Doppler bias across neighbouring parallel beam groups of the three processing methods shown in Fig. B.8 and B.9. With constant flow and otherwise ideal conditions the values should be zero. The dashed vertical lines indicate the transition between interleaving groups.

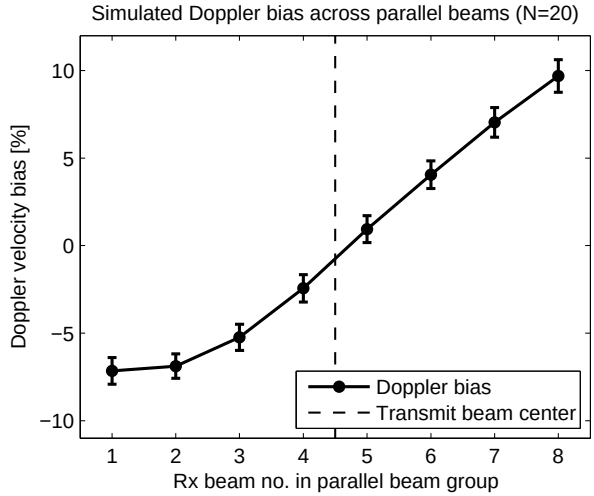

Figure B.11: Computer simulation of the Doppler bias for a situation closely resembling the linear-array *in vivo* images of Fig. B.8. The bias is estimated as the deviation from the mean velocity, and the uncertainty of the simulated results are indicated with error-bars showing $\pm\sigma/\sqrt{N}$ where σ is the standard deviation and $N = 20$ is the number of realizations.

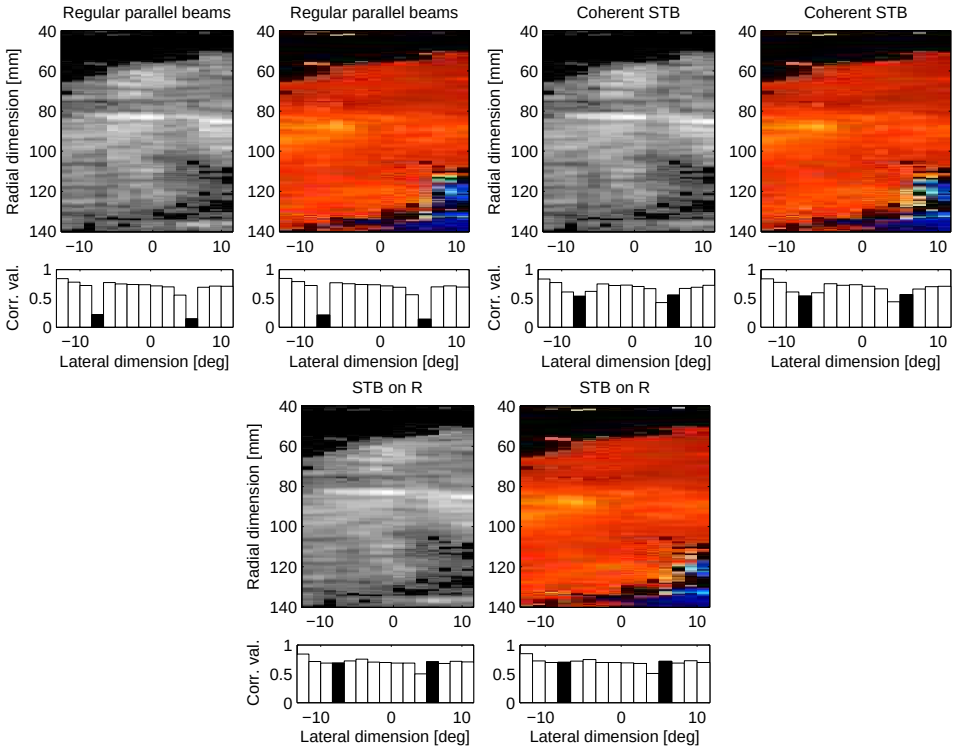

Figure B.12: Cardiac images captured with a phased array probe. Power images, R(0), are shown to the left and velocity images, angle(R(1)), are shown to the right. The images are not scan converted to make it easier to align the beams with the cross correlation plots.

B.4 Discussion

In this study we have described what causes the artifacts of parallel beamforming as applied to color flow imaging. In particular we have analyzed the previously undocumented Doppler bias effect caused by the varying Doppler shifts recorded offcenter from a curved transmit beam. We have also proposed solutions to the problem, in the form of coherent or incoherent Synthetic Transmit Beams (STB).

From the carotid images of Fig. B.8 it is clear that the application of STB reduces the artifacts from traditional parallel beam processing. The reduction of artifacts can be seen both from visual inspection of the images, and from the cross correlation plots beneath each figure. In regular parallel beamforming the cross correlation drops markedly across parallel beam groups, with black bars, but this is restored for both STB methods. The two STB methods differ noticeably at the transitions between interleave groups, where the cross correlation of coherent STB drops while incoherent STB does not.

Another difference between the coherent and incoherent STB methods is visible in the power images of Fig. B.8, where the signal at the interleave group transition in the center nearly disappears due to destructive interference. The power signal is used in some 2D color maps for vascular and cardiac imaging, so it is important that the power signal is also free from artifacts and dropouts.

The Doppler bias through the center of the artery is shown in Fig. B.9, and the abrupt discontinuities is easily visible for regular parallel receive beams. Both STB methods remove the discontinuities across parallel beam groups, but incoherent STB performs better across interleave groups. This is further seen in Fig. B.10, where only the bias at parallel beam group transitions is shown over the full width of the image to include all four interleave groups. For the depths $15 - 19mm$, around the maximum curvature seen in Fig. B.3, the average change is 19.9% for regular parallel beam processing. This corresponds well with the simulated values shown in Fig. B.11, which estimates the Doppler bias to be 9.7% for the edge beams, causing a total change of $2 * 9.7\% = 19.4\%$. Even the simple geometrical model with spherical wavefronts estimates the Doppler bias to be $2 * 9.1\% = 18.2\%$ which corresponds reasonably well with the simulated and in vivo results.

For both STB methods the *in vivo* Doppler bias drops to approximately 3%, which is not that easily visible in the images. There are peaks in the error plot of coherent STB at two of the interleave group crossings, and a trough at the third. This is due to the long time delay across interleave group crossing, which increases the variance of the estimates. This is not the case for incoherent STB.

Another effect to notice from Fig. B.10 is how the Doppler bias gets smaller for increasing depths of the artery. This can be explained by the position of the transmit focus of the recording, which is at the bottom of the color flow ROI. Close to the focal point the wavefronts are not expected to be curved, as shown in Fig. B.3, and the Doppler bias is expected to be minimal.

Similar results are seen from the cardiac images of Fig. B.12. They are acquired without interleaving, and both coherent and incoherent STB is able to reconstruct the beam-to-beam cross correlation, with the latter technique showing slightly better

results.

To benefit from an increasing number of parallel receive beams the transmitted pulse must be wider. This is typically done by limiting the aperture, which reduces penetration and signal to noise ratio.

In 3-D color flow imaging (3-D CFI) the trade-off between volume rates and image quality is particularly strained. For 3-D applications, and even more for 3-D CFI, parallel beamforming is particularly important to increase the volume rate without destroying the image quality. For 3-D imaging the beams are scanned two dimensionally, meaning that it is impossible to acquire overlapping beams, as required by STB, without a severe time penalty in at least one of the scanning dimensions. This makes 3-D CFI an ideal candidate for incoherent STB. It is still likely that the hemodynamics have changed significantly with the long data acquisition time of 3-D CFI, which makes it impossible to reconstruct the true velocity field. In this case incoherent STB will instead work as a temporal smoothing filter.

B.5 Conclusion

Parallel beam artifacts in color flow imaging are largely caused by the varying Doppler shifts recorded off center from a curved transmit beam. These artifacts can be reduced significantly by using *synthetic transmit beams (STB)*. With a small time delay between overlapping beams, coherent STB works well. With longer time delays, for instance across interleave groups, it is better to perform incoherent STB on the auto-correlation estimates instead of coherently on IQ data. STB reduces the need for lateral smoothing of color flow images made with several parallel beams, meaning that color flow images with a higher resolution can be obtained with a higher frame rate than can be obtained without STB.

References

[1] D. P. Shattuck, M. D. Weinshenker, S. W. Smith, and O. T. von Ramm, "Explososcan: A parallel processing technique for high speed ultrasound imaging with linear phased arrays," *Journal of the Acoustical Society of America*, vol. 75, no. 4, pp. 1273–1282, 1984.

[2] O. T. von Ramm, S. W. Smith, and H. G. Pavy, "High-speed ultrasound volumetric imaging system – part ii: Parallel processing and image display," *IEEE Transactions on Ultrasonics, Ferroelectrics, and Frequency Control*, vol. 38, March 1991.

[3] T. Hergum, T. Bjåstad, K. Kristoffersen, and H. Torp, "Parallel beamforming using synthetic transmit beams," *IEEE Transactions on Ultrasonics, Ferroelectrics, and Frequency Control*, vol. 54, no. 2, pp. 271–280, 2007.

[4] D. W. Clark, *Method and Apparatus for Multiline Color Flow and Angio Ultrasound Imaging*. WO 2008/068709 A1, Jun 2008.

[5] B. A. J. Angelsen, *Ultrasound Imaging*. Trondheim: Emantec AS, 2000.

[6] J. A. Jensen, "Field: A program for simulating ultrasound systems," *Medical & Biological Engineering & Computing*, vol. 34, pp. 351–353, 1996.

[7] R. H. Chesarek, "Ultrasound imaging system for relatively low-velocity blood flow at relatively high frame rates." United States Patent 4.888.694, Dec. 1989.

[8] B. S. Robinson, "Ultrasonic diagnostic imaging systems with blended multiline for 2d and 3d applications." United States Patent 6.482.157, 2001.

[9] T. Bjåstad, S. A. Aase, and H. Torp, "The impact of aberration on high frame rate cardiac b-mode imaging," *IEEE Transactions on Ultrasonics, Ferroelectrics, and Frequency Control*, vol. 54, January 2007.

[10] T. Bjåstad and H. Torp, "Synthetic transmit beam technique in an aberrating environment," *IEEE Transactions on Ultrasonics, Ferroelectrics, and Frequency Control*, In press.

Paper C

Fast Ultrasound Imaging Simulation in K-space

Torbjørn Hergum[1], Stian Langeland[2], Espen Remme[3] and Hans Torp[1]
[1]Department of Circulation and Medical Imaging, NTNU, Trondheim, Norway
[2]GE Vingmed Ultrasound, Horten, Norway
[3]Institute for Surgical Research, Rikshospitalet, Norway

Abstract

Most available ultrasound imaging simulation methods are based on the spatial impulse response approach. The execution speed of such a simulation is of the order of days for one heart-sized frame using desktop computers. For some applications, the accuracy of such rigorous simulation approaches is not necessary. This work outlines a much faster 3-D ultrasound imaging simulation approach that can be applied to tasks like simulating 3-D ultrasound images for speckletracking.

The increased speed of the proposed simulation method is based primarily on the approximation that the point spread function is set to be spatially invariant, which is a reasonably good approximation when using polar coordinates for simulating images from phased arrays with constant aperture. Ultrasound images are found as the convolution of the PSF and an object of sparsely distributed scatterers. The scatterers are passed through an anti-aliasing filter before insertion into a regular beam-space grid to reduce the bandwidth and significantly reduce the amount of data.

A comparison with the well-established simulation software package Field II has been made. A simulation of a cyst image using the same input object was found to be in the order of 7000 times slower than the presented method.

Following these considerations, the proposed simulation method can be a rapid and valuable tool for working with 3-D ultrasound imaging and in particular 3-D speckle-tracking.

IEEE Transactions on UFFC, vol. 56, no. 6, pp. 1159–67, 2009

C.1 Introduction

Ultrasound imaging is an important tool in cardiology, and the availability of dynamic, 3-D simulated ultrasound images is important for testing and validation of quantitative volumetric measurements. Several methods to simulate ultrasound images have already been published. Some aim to obtain the best accuracy possible without solving the full wave equation, like *Abersim* [1], which can accurately simulate an ultrasonic beam through heterogeneous tissue. Another well-known simulation method is based on linearly calculating the impulse response at all scatterer-positions, as is done by *Field II* [2]. Yet another step down the ladder of accuracy is the simulation of images by convolving an object with a point spread function [3, 4]. This can be a good approximation as long as the PSF remains constant, as it does near the focal point.

For large simulation tasks, like simulating dynamic 3-D cardiac images, all the above methods have major shortcomings. The first 2 methods, *Abersim* and *Field II*, suffer from significant computational demands, where simulating a single 3-D cardiac frame will take weeks. Simulations based on the convolution approach are very memory-intensive, particularly for dynamic images where the simulation grid must be very fine to let the speckle pattern be coherent from frame to frame.

In the need for such simulated cardiac images, we propose a simulation method we have called *Fusk*, for fast ultrasound simulation in K-space. It is based on the convolution approach, but with a few new techniques to make it faster. Most importantly we use an antialiasing filter on each discrete scatterer to enable the simulation to run on a coarse beam-space grid.

In this article, we first provide a description of the methods to make the convolution-based simulation more efficient. Then images simulated using *Fusk* are shown and compared with images from *Field II* simulations. The number of scatterers in an ultrasound imaging simulation is important for the processing speed. A description of the number of scatterers necessary to obtain fully developed speckle are provided. Finally, an example of a simulated 3-D cardiac image is shown.

C.2 Theory

Simulation of time-varying 3-D ultrasound images using a Fourier-based convolution with a PSF tends to be very memory-intensive. In general, the input object will have a very high bandwidth. A vector-based drawing, for example, normally has infinite bandwidth and needs to be sampled very densely to limit aliasing artifacts when it is discretized before Fourier transformation. This is particularly important for dynamic objects, where the subresolution position of the scatterers determines the speckle pattern.

Ultrasound simulation methods based on calculating the impulse response of the system for each scatterer, like *Field II* [2], do not have such high memory requirements. This is due to the sparse input object, and only the positions in space holding a scatterer are stored. However, spatial impulse response simulation methods are computationally demanding, making them several orders of magnitude slower than a

simple convolution.

The benefit of methods based on calculating the spatial impulse-response at each scatterer location is the much higher accuracy obtained compared to convolution-based methods. The main assumption of convolution-based imaging methods is that the imaging system is completely shift invariant,i.e., the PSF is equal in the whole image. However, ultrasound imaging is only spatially shift invariant in regions and is normally more shift invariant laterally than radially.

One notable exception to this is if the imaging system uses a wide transmit beam and expanding aperture on reception (Rx), keeping the Rx $f_{\#}$ (the ratio of the focal depth to the aperture size) constant with depth. The PSF will be dominated by the low Rx $f_{\#}$ relative to the transmit (Tx) $f_{\#}$, making the PSF approximately constant with depth.

Similarly, the imaging system can be nearly shift invariant for a phased-array setup where the beams are spread out in a fan instead of being parallel. With a constant aperture a, the angular width of the PSF is proportional to the ratio of the wavelength and the aperture size λ/a [5], that is, it is independent of depth. This is very common for cardiac imaging, where the aperture size is small due to the limited acoustic window between the ribs. This approximation is even better for a modern 2-D array where the focusing is dynamic in both the lateral and the elevation directions, in contrast to standard 1-D arrays with a fixed focus in the elevation direction.

One drawback of a convolution-based simulation compared with impulse-response methods is the neglect of the timing differences between beams, which makes it cumbersome for Doppler simulations. Additionally, both simulation methods neglect multiple scattering and reverberations.

Investigating the ultrasound imaging process in the Fourier domain, often dubbed K-space, is beneficial for understanding the present work. According to the Fraunhofer approximation, the lateral variation of the continuous wave (CW) ultrasound field at the focal depth can be approximated as the Fourier transform of the aperture [6]. The Fourier transform of this ultrasound field is thus a scaled version of the aperture. Extending this principle from CW to pulsed wave (PW) acquisition, containing more frequency components, the K-space representation of the ultrasound focal field is a lowpass-process in the lateral and elevation dimension and a bandpass process radially [7]. This is illustrated in Fig. C.1.

Radially, the region of support is centered on $2k_0 = 2f_0/c$, and bounded by the pulse bandwidth. In the k_x and k_y directions, the region of support is bounded by the aperture function, where the lateral width increases linearly with increasing radial frequency, meaning it is not a separable process.

Upon reception, the lateral K-space response is convolved with the reception aperture, and the radial resolution is approximately doubled due to the pulse compression. With equal transmit and receive apertures of size a focused at depth R, the critical angle as shown in Fig. C.1 is $\phi = tan^{-1}(1/2f_{\#})$, where $f_{\#} = R/a$. For arbitrary apertures, the maximum lateral frequency component is governed by $f_{\#tr} = R/(a_{tx}+a_{rx})$.

Simulation of harmonic imaging can be included by using the quasilinear approximation to calculate the PSF as described in [8]. The second harmonic PSF can be approximated even further by using the square of the linear transmitted field as the

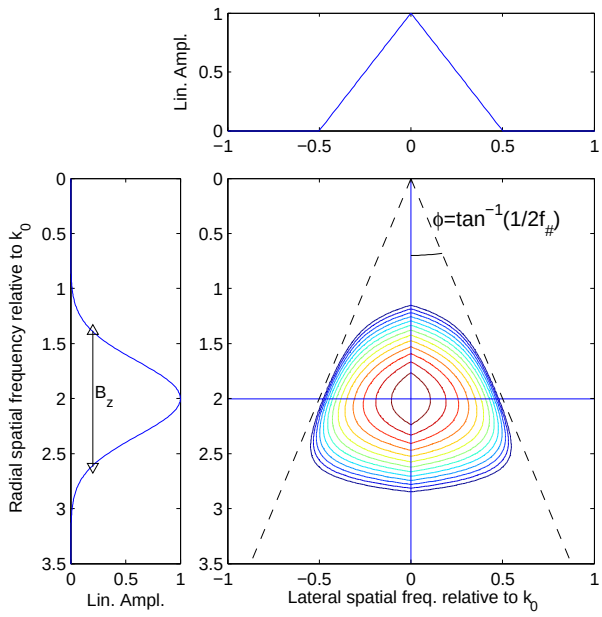

Figure C.1: The bottom right pane shows a coutour plot of a K-space point spread function (only showing positive radial frequencies); 3 dB separates each contour, with a total dynamic range of 40 dB for this figure. The top pane shows the aperture response at $k_z = 2k_0$ in a linear scale, indicated by the horizontal line of the image. Likewise the left pane shows the pulse response as indicated by the vertical line. The transmit and receive apertures are equal, which results in a triangular aperture response. The maximum lateral frequency content for each radial frequency is governed by the opening angle of the region of support, ϕ. For this case of equal transmit- and reception apertures $\phi = tan^{-1}(1/2f_{\#})$.

harmonic field. In K-space, this means the harmonic transmit response is an auto-convolution of the linear response laterally, and the center point in the f_z direction is shifted from f_0 to $2f_0$.

C.3 Method

To simulate 3-D dynamic objects efficiently and still maintain a proper dynamic speckle-pattern across frames, the inherent band-limited nature of ultrasound imaging is exploited. Instead of using a high-resolution simulation grid, a much coarser grid governed by ultrasound sampling criterions is used. In the radial direction, only a band with the desired bandwidth B_z centered on $2k_0$ is needed. This is illustrated in Fig. C.1. The minimum lateral sampling frequency needed to avoid aliasing is found from the maximum radial frequency content, $2k_0 + B_z/2$, evaluated at the critical angle ϕ to give $k_{zmin} = \pm(2k_0 + B_z/2)/(2f_{\#tr})$. Because the radial dimension only contains data in a relatively narrow band around the center frequency, the amount of data to be processed can be greatly reduced by performing all calculations in the baseband.

A sparse input object containing point scatterers has infinite bandwidth along all dimensions. An approximation with a fine grid after antialiasing reduces the bandwidth to a maximum of the inverse of the grid resolution, which is illustrated as region (a) in Fig. C.2. The PSF of ultrasound images only contain frequencies within the regions denoted by (c+) and (c), where the sign indicates the mirrored positive and negative frequencies. To reduce the amount of data without loosing information within the bandwidth of the PSF, a complex antialiasing filter is applied to the object, keeping only frequencies in region (b), which is slightly larger than region (c+).

The antialiasing filter is applied by placing each scatterer into the coarse simulation grid not as a point, but rather as a shifted and sampled impulse response of a separable 3-D antialiasing filter:

$$\begin{aligned} s(m_x, m_y, m_z) = \sum_k \sum_{l_{x,y,z}} & v_k \delta(x - x_k, y - y_k, z - z_k) \\ & h_x(m_x D_x - l_x) h_y(m_y D_y - l_y) h_z(m_z D_z - l_z) \\ & e^{-i2\omega_d z_k / c} \end{aligned} \tag{C.1}$$

where s is the sampled, demodulated, antialiased object; v_k is the scattering strength of each scatterer δ; h_x is an analog lowpass filter in the x-direction sampled with a spacing D_x, which is similar for the y and z-directions; ω_d is the demodulation frequency; and c is the speed of sound. In practice the antialiasing filter is found by 3 lookups into a short lookup table and subsequently mixing with a phasor in the radial direction. An example of 2 infinite- bandwidth point scatterers being prepared for a 1D-convolution is shown in Fig C.3. The red, dashed lines shows the antialiasing filter from the lookup table, shifted and scaled according to the position of the 2 delta-scatterers. A few values from the coarse-grid positions are selected, or looked

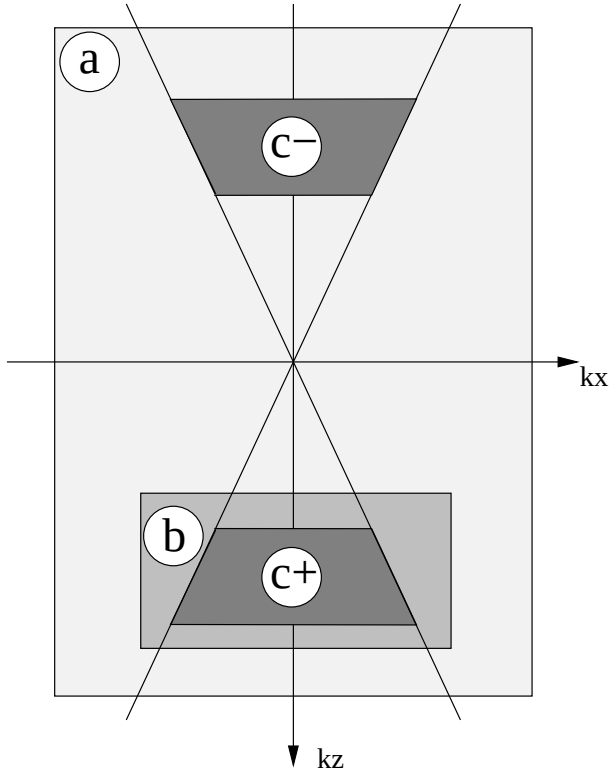

Figure C.2: Illustration of the various regions of K-space involved in the antialiasing process. Region a indicates the frequency content of the object, region b indicates the bandwidth of the antialiasing filter and region c indicates the region of support of the point spread function as was shown in Fig. C.1.

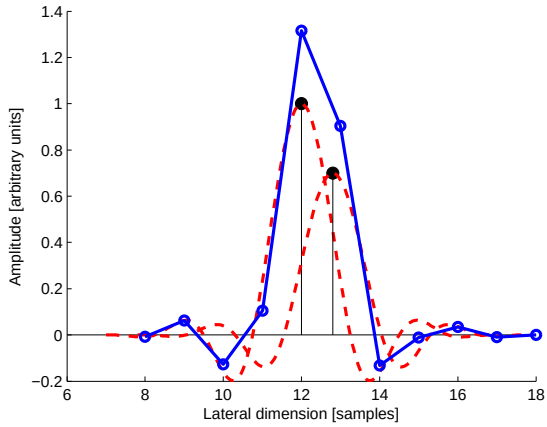

Figure C.3: Lateral antialiasing filter. Two high-precision scatterers (vertical black stems) replaced with a shifted and scaled antialiasing filter (dashed, red). The sum of the sampled, filtered result (solid blue line) is used as the coarse simulation-object. In the radial direction, a complex antialiasing-filter is used to include demodulation to base-band.

up, from the high resolution antialiasing filter, and summed to yield the coarse blue object.

The antialiasing filter used is a real-valued FIR lowpass filter in the lateral and elevation direction. The impulse response of such a filter is shown in Fig. C.4 and the corresponding frequency response is shown in Fig. C.5. In the radial direction the filter is multiplied with a complex exponential, performing complex demodulation together with the bandpass filtering.

An example of a collection of point scatterers used as input object to *Fusk* is shown in Fig. C.6 [9].

C.3.1 Phased array imaging

BecauseFusk is based on a Fourier convolution approach, all the scanlines have to be positioned with fixed spacing in Cartesian coordinates. Simulation of phased-array imaging is made possible by reverse scan-converting the input object instead of fanning out the beams. The reverse-scan-converted object is run through the simulation, resulting in the desired nonscan-converted image. This is illustrated schematically in Fig. C.7 and an example is shown in Fig. C.9.

The inverse-scan-converted object is found by transforming the scatterer positions to spherical coordinates. Inverse-scan-conversion implies spreading out the object above the focal depth and compressing it below. To obtain an even scatterer density in beam space, the scatterer density of the Cartesian object should be proportional to $1/r$, i.e., it should have an increased scatterer density near the transducer.

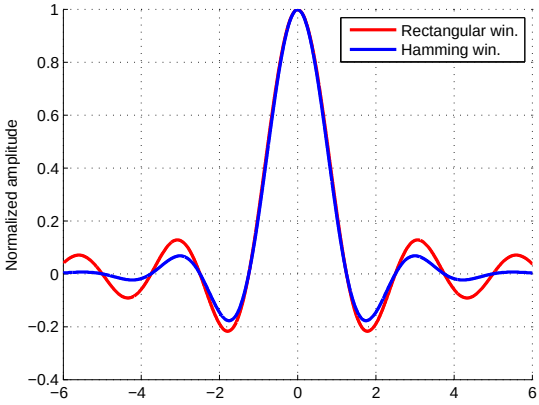

Figure C.4: Antialiasing filter impulse response. The hamming window was used for the results shown in the Results section.

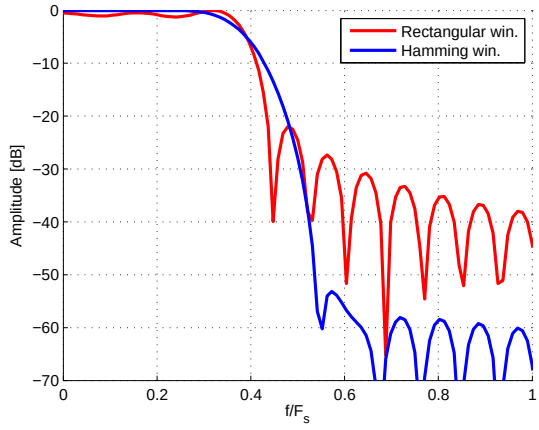

Figure C.5: Antialiasing filter frequency response. At the Nyquist limit, $f/F_s = 0.5$, the response has dropped to $-30dB$. The transition period is rather long, meaning that some oversampling of the object is necessary to make sure that the highest spatial frequencies are maintained. It is a finite-impulse response filter, so the phase is linear (not shown).

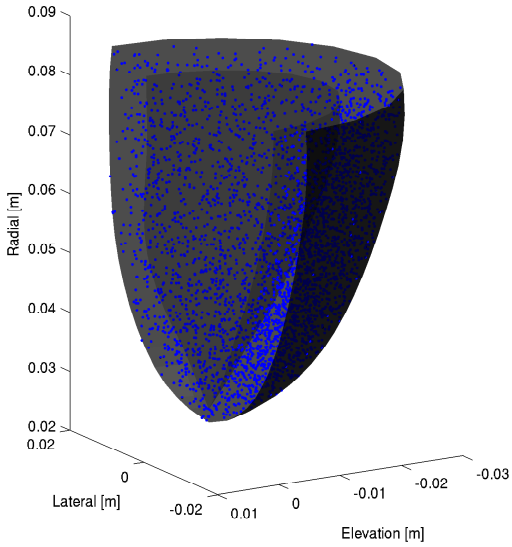

Figure C.6: A cut-through of a ventricular model showing some of the $\approx 700,000$ scatterers within the wall. The scatterers are randomly positioned material points from the finite element model with known positions throughout the cardiac cycle.

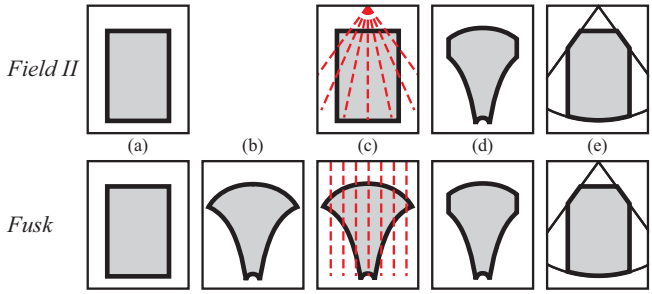

Figure C.7: Reverse scan conversion illustrated. The top row shows the standard phased array simulation steps as done by Field II, and the bottom row shows how Fusk performs the same task. Step (a) shows the real object to be imaged, a rectangle. In the top row, step (c) shows the fanning out of the beams of phased-array imaging. The received signals from these beams are shown in beam space in step (d). After scan conversion, we arrive at the image in step (e). With Fusk, an additional step (b) is included, where the object is reverse scan converted, that is, it gets the same geometry as in step (d) of standard imaging. The ultrasound simulation is performed as for a linear array in step (c), to arrive at the same beam-space image and scan converted image in steps (d) and (e), respectively.

C.3.2 Dynamic Cardiac Images

One example of an interesting application of Fusk is the simulation of dynamic 3-D ultrasound images of the left ventricle. A finite element model of an ellipsoidally shaped left ventricle was used to simulate realistic myocardial motion throughout the cardiac cycle during normal and ischemic conditions [10]. Point scatterers were extracted from the model as material points with known positions through the cycle. Knowing the exact location of all scatterers at all times makes for an excellent reference, e.g., for testing of speckle-tracking algorithms [11]. An example of such an object is shown in Fig. C.6.

C.3.3 Scatterer Density

Speeding up an ultrasound simulation can be done by making the program more efficient, as discussed above, or by reducing the number of scatterers in the model. When the density of the scatterers is too low, the resulting speckle pattern will not be fully developed. To be fully developed, the amplitude of the real and imaginary part of the IQ-signal of the speckle pattern needs to be independent and Gaussian-distributed, making the envelope of the signal Rayleigh distributed [12–14].

The second-order statistics will be correct if the scattering object is sampled according to the Nyquist criterion. A full-band simulation (like that of Field II) and an object with scatterers positioned on a grid require the scatterers to be spaced no more than $\frac{2f_{\#tr}}{2k_0+B_z/2}$ apart laterally and $1/(2k_0 + B_z/2)$ radially; see Fig. C.1. For a baseband simulation like Fusk, the requirement for radial sampling density is relaxed, and the scatterers need to be positioned just c/B_z apart. With irregularly spaced scatterers, the sampling frequency is not well defined, but it is still likely that Fusk requires a lower scatterer density to obtain fully developed speckle compared with full-band simulations.

C.3.4 Validation

To validate the proposed ultrasound-imaging simulator, it is compared with the well-known software package Field II [2]. Care has been taken to run the 2 simulators with the same imaging settings, which means that no frequency- dependent scattering or attenuation is included. Both software packages are implemented using Matlab (MathWorks, Natick, MA) with some core parts implemented using C, interfaced as a *mex*-file. For this paper, the simulations were performed on a Dell Precision 670n computer with an Intel Xeon 3.0 GHz processor and 4 Gb RAM.

Images of a point scatterer as well as a speckle-generating cyst phantom have been made using equal simulation parameters, listed in Table C.1. The cyst phantom contains $\sim 410,000$ scatterers with randomly distributed positions.

Local spatial shift invariance is an important property of any imaging system, particularly when features within the images are tracked from frame to frame. The shift invariance properties of Fusk and Field II have been investigated as explained in [15]. That is, a point scatterer has been moved laterally across the beam, and the

Table C.1: Some common parameters for simulations and experiments.

Parameter	Value
Center frequency f_0	2.5 MHz
Pulse bandwidth (FWHM)	0.62 MHz
Focal point	6 cm
Aperture (Tx and Rx)	22x13 mm
Apodization (Tx and Rx)	Rectangular
Pitch (*Field II*)	$343\mu m$
Antialiasing filter window	Hamming

RMS profile for each position of the scatterer is stacked and displayed as an image in Fig. C.12. A laterally shift invariant imaging simulator produces a diagonal structure, meaning the image of the point does not change as the scatterer moves - it merely shifts sideways. Similarly, the radial shift invariance has been examined by moving the scatterer radially. The latter data are also used for Doppler analysis to further verify that the phase of the IQ signal is accurate despite the coarse simulation grid.

C.4 Results

Cross-sectional images and pulse-echo beam profiles of a point scatterer at the focal depth is shown in Fig. C.8. Note the similarities of the cross-sectional images, as well as the position and level of the main lobe and sidelobes of the beam profiles.

Images from the speckle-generating phantom with embedded hypo- and hyperechoic regions are shown in Fig. C.9. The processing time of the Fusk simulation was 7220 times faster than the Field II simulation (23.6 s vs. 46.6 h). Please note the similarities of the 2 images near the focal depth of 6 cm. To compare the differences as a function of depth, the envelope of the signal from one beam is shown in Fig. C.10.

Fig. C.11 shows a scan-converted and volume-rendered example of a simulated 3-D image of the left and right ventricle, where the input object contains $\sim 700,000$ scatterers, some of which are shown in the movie in Fig. C.6.

Fig. C.12 and Fig. C.13 show the lateral and radial shift invariance of the 2 simulation methods, respectively,as explained above. The data from the radial shift invariance simulation has also been processed with a Doppler algorithm, and the resulting Doppler spectrum is shown in Fig. C.14.

Fig. C.15 shows the histogram of the IQ signal of Fusk and Field II from imaging a speckle-generating phantom. The scatterers are positioned in a grid, and they have complex, Gaussian-distributed scattering strengths. The lateral scattering distance corresponds to the lateral Nyquist sampling requirement of the RF domain, and the radial scattering distance is set to be slightly oversampled relative to the sampling criterion of the RF signal or 2 times undersampled. Please note the differences in the result for Fusk and Field II for the undersampled phantom.

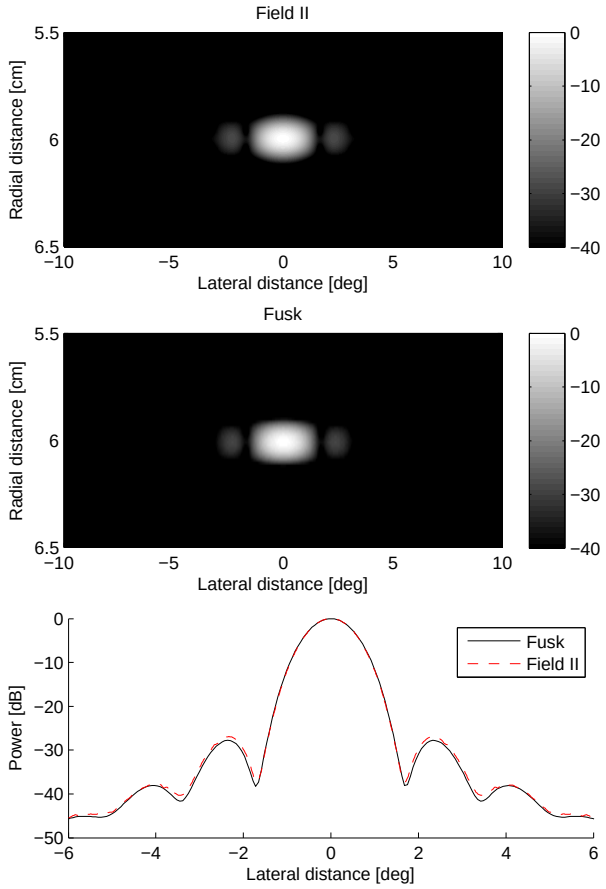

Figure C.8: Simulation of a point scatterer object at the focal depth of 6 cm, using a high scanline density and shown using $40dB$ dynamic range. The RMS beam profile is plotted in the bottom pane.

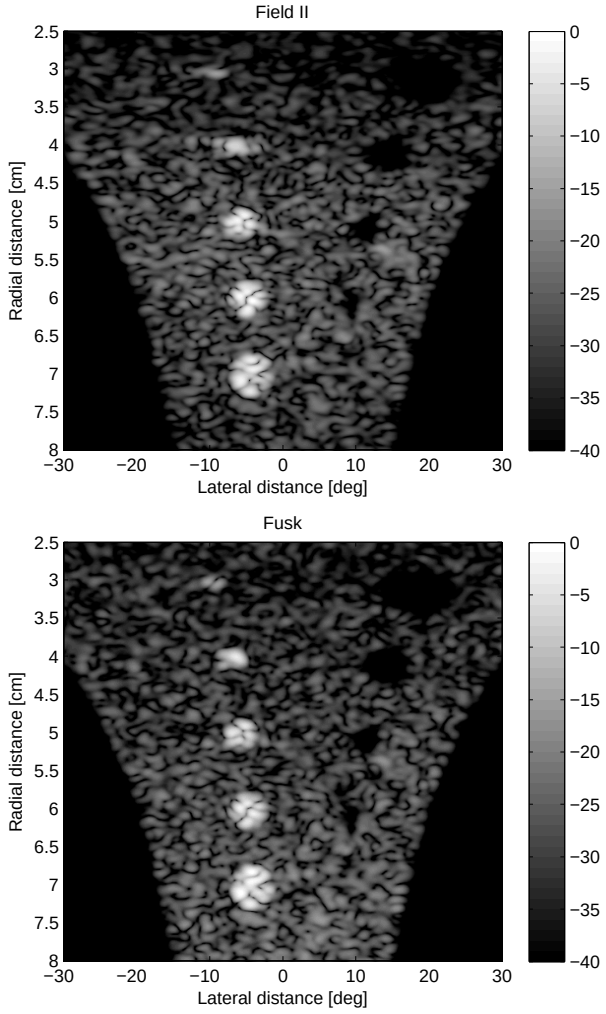

Figure C.9: Comparison of simulating a cyst-phantom using Field II (top) and Fusk (bottom). The phantom contains $\sim 410,000$ scatterers, and the processing time of the Field II-simulation was 7220 times slower than the Fusk simulation. The images are shown in beam-space coordinates to make the differences in the simulation methods most noticeable. This corresponds to step (d) of Fig. C.7.

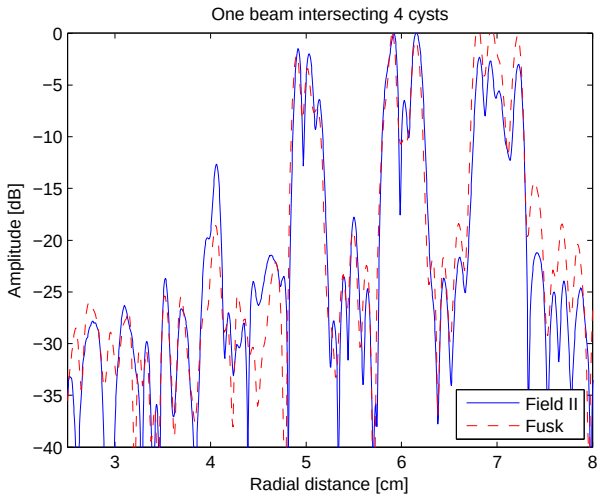

Figure C.10: Plot of the envelope of one beam intersecting the cysts of increased intensity shown in Fig. C.9. The focal depth is 6 *cm*.

C.5 Discussion

In this study, we have developed a method for fast simulation of ultrasound images, and we have applied it for simulation of dynamic 3-D cardiac images.

From investigating the PSF and beam profiles of Fusk and Field II in Fig. C.8 as well as the cyst-phantom simulations in Fig. C.9 it is apparent that Fusk performs quite well near the focal depth. Fusk simulates imaging with either constant $f_{\#}$ or constant aperture, which means that the images have a constant PSF either in Cartesian or beam space coordinates. The errors of this approximation are largest far away from the transmit focus, as in the near field. Field II will accurately reproduce the untidy acoustic diffraction pattern in the nearfield, but these effects will not be present in Fusk simulations. This error is most easily seen in Fig. C.10. One of the differences most easily spotted is the gain difference of the 2 methods. Fusk has a constant gain as a function of depth, while Field II has maximum gain in the focal region. A suitable time gain compensation can be applied to compensate for this. There is also some variation in the speckle pattern, particularly near the transducer, although the 2 methods show striking similarities despite the different processing approaches and large differences in speed.

Frequency-dependent attenuation has not been included in these simulations, but it can be incorporated by using a larger pulse bandwidth and filtering the image radially with a depth-dependent bandpass filter.

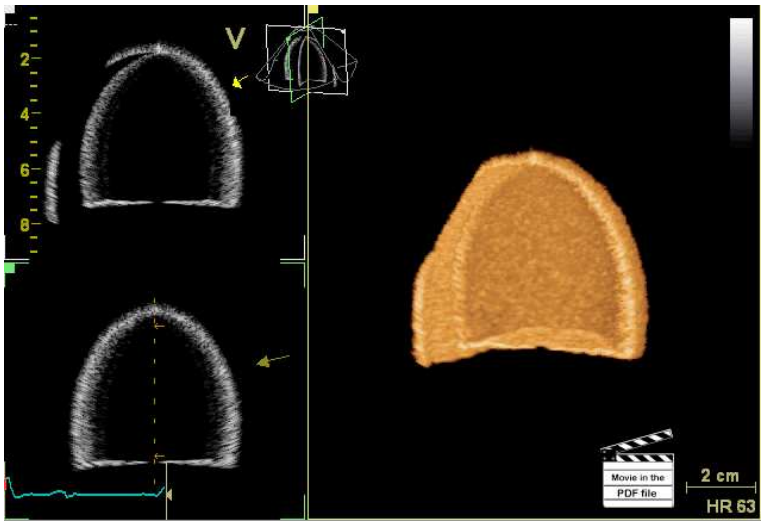

Figure C.11: 3-D rendering example from Fusk simulation. A slice of the input object is shown in Fig. C.6. The electronic version of this document, containing the movie, can be found at http://urn.kb.se/resolve?urn=urn:nbn:no:ntnu:diva-5937.

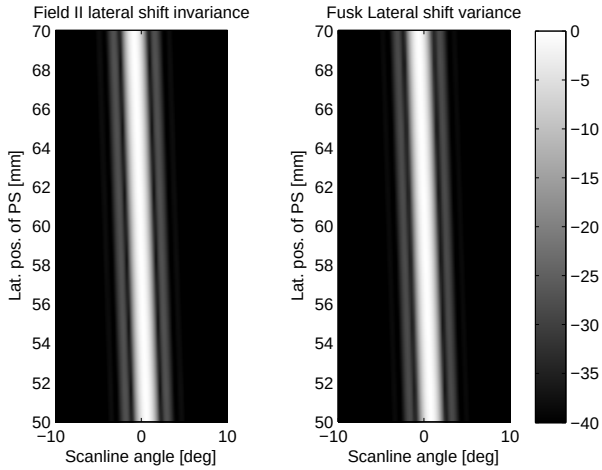

Figure C.12: *Field II* (left) and *Fusk* lateral shift invariance plot. For more details on shift invariance plots, see [15]. PS = point scatterer.

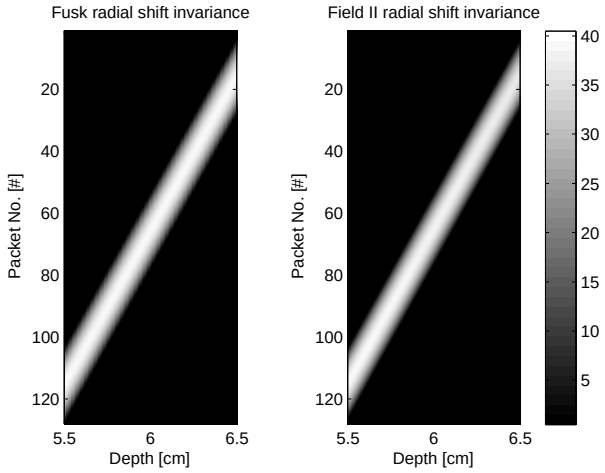

Figure C.13: Illustration of radial shift invariance of Field II and Fusk. A point scatterer is moving across the focal depth, which is in the middle of the z-axis.

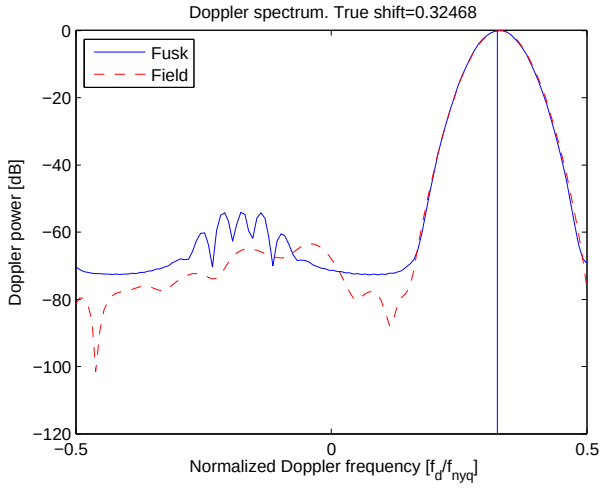

Figure C.14: Doppler spectrum from Fusk and Field II simulation of a moving point scatterer. Made from one slow-time column of Fig. C.13.

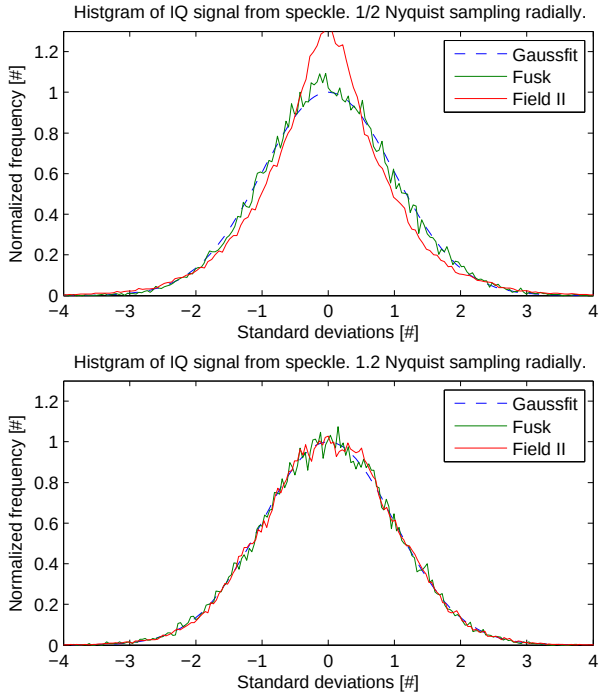

Figure C.15: Distribution of IQ signal amplitude from a speckle-generation phantom changes with varying radial scatterer density. Laterally the scatterers are positioned according to the sampling criterion. Radially the scatterers are positioned with 2 times undersampling according to the sampling criterion for a full-band simulation (top pane), and with 20% oversampling in the bottom pane. The point scatterers are positioned in a grid.

As expected, both simulation tools display excellent shift invariance properties, as seen in Fig. C.12 and Fig. C.13. This is not the case if the beam density is below the Rayleigh criterion or if the antialias filtering in Fusk is not done properly, although this is not shown here. This is further displayed in the Doppler spectra of Fig. C.14, where the spectra are nearly identical above the noise floor.

The histograms in Fig. C.15 shows that Fusk needs fewer scatterers than Field II to get fully developed speckle if the scatterers are given complex Gaussian scattering strengths. This is due to Fusk performing the simulations in baseband, thus requiring a lower radial sampling frequency compared with the full-band simulation of Field II.

The reason for using the 2-stage process of filtering each scatterer with an antialiasing filter and subsequentially filtering the whole object with the PSF filter instead of doing a full convolution with the PSF in the first place is due to processing speed. The 3-D separable antialiasing filter is realized using a short 1-D lookup-table, where a small amount of computer memory is changed for each new scatterer. Fig. C.1 shows that the PSF is not separable, so using the full 3-D PSF instead of the antialiasing filter would require significantly more memory to be changed when inserting each new scatterer. This will result in a performance degradation.

The accuracy of Fusk is best when the full aperture is used on reception for phased-array simulations. Better nearfield accuracy can be obtained by simulating more than one transmit zone using different PSFs.

Three orders of magnitude reduction in processing time can make up for the lack of accuracy for some applications. We have used Fusk successfully in the development of 3-D volumetric methods, where the data sets would have taken several weeks to generate using Field II.

C.6 Conclusion

It has been shown that the ultrasound simulation method Fusk can be a fast replacement for Field II and that it has acceptable accuracy for some applications. A cyst phantom image was simulated 7220 times faster using Fusk compared with Field II. Dynamic 3-D cardiac images have been made using Fusk. This is a task that would be exceedingly time consuming with standard simulation methods.

References

[1] T. Varslot and S.-E. Måsøy, "Forward propagation of acoustic pressure pulses in 3D soft biological tissue," *Modeling, Identification and Control*, vol. 27, no. 3, pp. 181–200, 2006.

[2] J. Jensen and N. B. Svendsen, "Calculation of pressure fields from arbitrarily shaped, apodized, and excited ultrasound transducers," *IEEE Transactions on Ultrasonics, Ferroelectrics, and Frequency Control*, vol. 39, pp. 262–267, 1992.

[3] J. C. Bamber and R. J. Dickinson, "Ultrasound B-scanning: a computer simulation," *Physics in Medicine and Biology*, vol. 25, no. 3, pp. 463–479, 1980.

[4] Q. Duan, P. Moireau, E. D. Angelini, D. Chapelle, and A. F. Laine, *Functional Imaging and Modeling of the Heart*, ch. Simulation of 3D Ultrasound with a Realistic Electro-mechanical Model of the Heart, pp. 463–473. Springer Berlin/Heidelberg, July 2007.

[5] J. N. Wright, *Image formation in diagnostic ultrasound*. IEEE international ultrasonics symposium short course, 1997.

[6] Goodman, *Introduction to Fourier optics*. Roberts & Company Publishers, third ed., 2005.

[7] W. F. Walker and G. E. Trahey, "The application of k-space in pulse echo ultrasound," *IEEE Transactions on Ultrasonics, Ferroelectrics, and Frequency Control*, vol. 45, pp. 541–558, 1998.

[8] H. Torp, T. F. Johansen, and J. S. Haugen, "Nonlinear wavepropagation - a fast 3D simulation method based on quasi-linear approximation of the second harmonic field," in *IEEE International Ultrasonics Symposium Proceedings*, pp. 567–570, 2002.

[9] S. I. Rabben, A. L. Haukanes, and F. Irgens, "A kinematic model for simulating physiological left ventricular deformation patterns - a tool for evaluation of myocardial strain imaging," in *IEEE International Ultrasonics Symposium Proceedings*, pp. 134–137, 2003.

[10] E. W. Remme and O. A. Smiseth, *Functional Imaging and Modeling of the Heart*, ch. Characteristic Strain Pattern of Moderately Ischemic Myocardium Investigated in a Finite Element Simulation Model, pp. 330–339. Springer Berlin / Heidelberg, 2007.

[11] J. Crosby, B. H. Amundsen, T. Hergum, E. W. Remme, S. Langeland, and H. Torp, "3-D speckle tracking for assessment of regional left ventricular function," *Ultrasound in Medicine & Biology*, vol. 35, pp. 458–71, Mar. 2009.

[12] R. F. Wagner, S. W. Smith, J. M. Sandrik, and H. Lopez, "Statistics of speckle in ultrasound B-scans," *IEEE Transactions on Sonics and Ultrasonics*, vol. 30, pp. 156–163, May 1983.

[13] R. Wagner, M. Insana, and S. Smith, "Fundamental correlation lengths of coherent speckle in medical ultrasonic images," *Ultrasonics, Ferroelectrics and Frequency Control, IEEE Transactions on*, vol. 35, pp. 34–44, Jan 1988.

[14] R. M. Cramblitt and K. J. Parker, "Generation of non-rayleigh speckle distributions using marked regularity models," *IEEE Transactions on Ultrasonics, Ferroelectrics, and Frequency Control*, vol. 46, pp. 867–874, July 1999.

[15] T. Hergum, T. Bjåstad, K. Kristoffersen, and H. Torp, "Parallel beamforming using synthetic transmit beams," *IEEE Transactions on Ultrasonics, Ferroelectrics, and Frequency Control*, vol. 54, no. 2, pp. 271–280, 2007.

The Effect of Including Myocardial Anisotropy in Simulated Ultrasound Images of the Heart

Jonas Crosby[1], Torbjørn Hergum[1], Espen Remme[2] and Hans Torp[1]
[1]Department of Circulation and Medical Imaging, NTNU, Trondheim, Norway
[2]Institute for Surgical Research, Rikshospitalet, Norway

Abstract

We have examined the effect of incorporating tissue anisotropy in simulated ultrasound images of the heart. In simulation studies, the cardiac muscle (myocardium) is usually modeled as a cloud of uncorrelated point scatterers. Although this approach successfully generates a realistic speckle pattern, it fails to reproduce any effects of image anisotropy seen in real ultrasound images. We hypothesize that some of this effect is caused by the varying orientation of anisotropic myocardial structures relative to the ultrasonic beam, and that this can be taken into account in simulations by imposing an angle dependent correlation of the scatterer points.

Ultrasound images of a porcine heart were obtained *in vitro*, and the dominating fiber directions were estimated from the insonification angles that gave rise to the highest backscatter intensities. A cylindrical sample of the myocardium was then modeled as a grid of point scatterers correlated in the principal directions of the muscle fibers, as determined experimentally. Ultrasound images of the model were simulated by using a fast k-space based convolution approach, and the results were compared with the *in vitro* recordings.

The simulated images successfully reproduced the insonification dependent through-wall distribution of backscatter intensities in the myocardial sample, as well as a realistic speckle pattern.

IEEE Transactions on UFFC, vol. 56, no. 2, pp. 326–33, 2009

D.1 Introduction

Significant research effort is put into development of new echocardiographic analysis tools for evaluation and quantification of myocardial function, which has recently resulted in e.g. tissue Doppler imaging, automatic volume segmentation methods, and speckle tracking echocardiography. Testing of the algorithms is an important part of the development process. It may be difficult to obtain a reliable reference in an *in vivo* context. Computer-simulated ultrasound images have therefore become a valuable tool for determining how well such methods perform under varying conditions. The cardiac muscle (myocardium) in these simulations is often modeled as a cloud of sub-resolution, uncorrelated point scatterers [1–3], which leads to a fully developed speckle pattern in the resulting image. Unfortunately, this approach fails to reproduce some of the echogenic properties of the myocardium observed in images of real hearts.

Regional variations in intensities inside the heart walls have been observable in 2D ultrasound images since the late seventies but the effect has become more prominent as the image quality has improved. Aygen et al. [4] examined the correspondence between the regional differences in backscatter intensity and the known fiber orientations in the left ventricle, and found that the bright regions in large degree were consistent with the regions where the ultrasound beams were perpendicular to the anticipated fiber directions. This effect is illustrated in Fig. D.1: In the apical 4-chamber image of the heart (Fig. D.1(a)), the circumferentially oriented muscle fibers in the middle of the intraventricular septum becomes perpendicular to the beam, thus causing a line of increased intensities in the image. By choosing a more oblique view (Fig. D.1(b)), this septal line is shifted sideways towards the endocardium where the fibers are oriented more longitudinally. In the short axis view(Fig. D.1(c)), the circumferential fibers in the midwall are nearly parallel with the beams that results in a reduced intensity in this region. On the LV and RV sides of the septum the fibers are more longitudinally oriented and intensity is higher on each side of the septal midwall. This view-dependence of the ultrasonic backscatter and attenuation has been thoroughly investigated by James G. Miller at the Washington University in St. Louis and his coworkers, by the means of tissue specimens, phantoms with graphite fibers, and measurements *in vivo*[5–10]. Furthermore, they have been using the angular dependence of backscatter and attenuation found by experimental measurements to model the effects of myocardial anisotropy on short-axis ultrasound images [11, 12]. In addition, a statistical parametric model of this effect has been developed by Santarelli and Landini [13], in which the myocardium were regarded as a matrix of cylindrical scatterers.

Unlike skeletal muscles that consist of quite large muscle cells (myocytes) arranged in regular, parallel bundles, the cardiac muscle has a far more complex architecture of smaller myocytes with extensive branching. However, as the contractile direction is quite homogenous in adjacent cardiac muscle cells, it is possible to define a local fiber direction. This fiber direction has been shown to have a similar distribution in mammalian hearts, following a helical pattern with smoothly varying inclination across the wall[14]. It has also been shown that the muscle fibers are organized in sheets, about four cells thick, interconnected by collagen cords, and separated by extracellular gaps (cleavage planes) [15]. Furthermore, the primary, secondary and

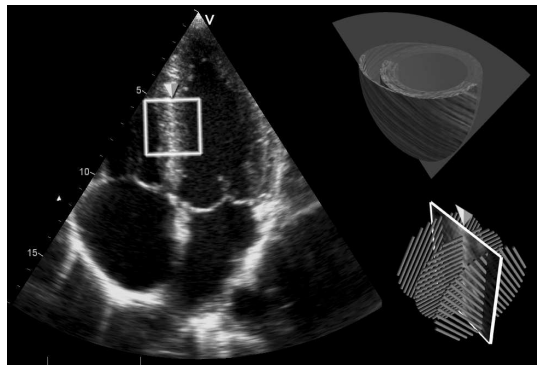

(a) 4-chamber view.

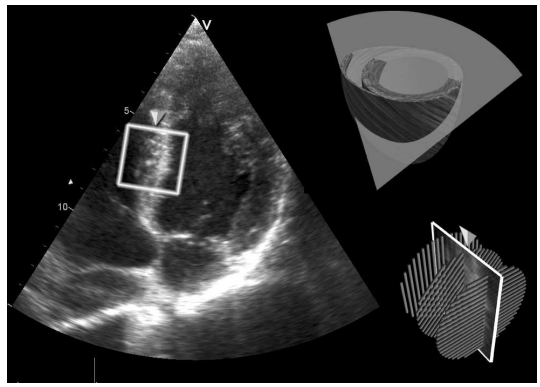

(b) Oblique view.

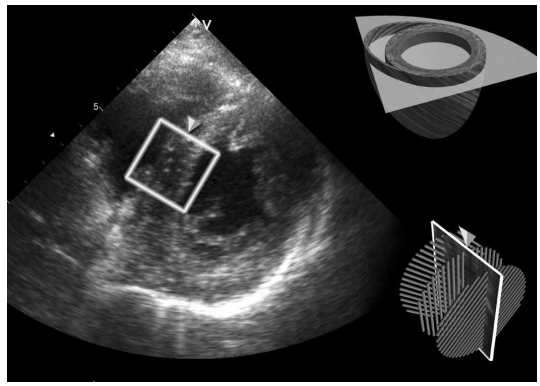

(c) Short-axis view.

Figure D.1: View-dependence of backscatter signal in B-mode images. The white squares enclose a part of the septal wall with the arrow pointing at the edge closest to the probe. The illustrations in the upper right corners indicate the position of the views relative to the left and right ventricles. The illustrations in the lower right corners show the expected out-of-plane fiber orientations in three layers that intersect the enclosed part of the septal wall.

tertiary eigenvectors from diffusion tensor magnetic resonance imaging (DT-MRI) have been found to correspond to the fiber direction, sheet direction and sheet normal, respectively [16].

Although the anisotropy of the myocardium is well-described, the effect of this anisotropy has been neglected in simulation-based validation of new tracking and segmentation methods. To the authors' knowledge, no ultrasound simulation approach incorporating myocardial anisotropy suited for validation of such methods has been reported. The aim of this study was to develop an anisotropic model of myocardial tissue that can be used with ultrasound simulations in order to obtain more realistic simulated cine images of the heart. In this first study, the simulation was limited to a region of interest in the septal wall, where the transmural variation of backscatter often is very striking in the ultrasound image. Previous simulations of myocardial anisotropy have originated from the field of ultrasonic tissue characterization, and have been designed for predicting the magnitude of backscatter. In contrast, the model in this study is intended to be used with motion tracking methods — e.g. optical flow, speckle tracking and edge detection techniques — in 2D or 3D ultrasound data. As the dynamic range usually is adjusted prior to the application of these methods, the absolute backscatter levels are of less importance than for tissue characterization. On the other hand, temporal continuity is crucial in order to be able to track motion. The main idea in our approach, was to enforce a directional correlation of the amplitudes of the point scatterers prior to the ultrasound simulation.

D.2 Background

In order to study the effect of anisotropy, it can be illustrative to look at the imaging process in the spatial frequency domain, also known as *k-space* [17, 18]. The limited bandwidth in ultrasound transducers, makes pulse-echo imaging a bandpass process axially. In addition, the limited aperture makes the imaging process a low-pass process laterally relative to the beam direction. This corresponds to a k-space region of support corresponding to the system's point spread function (PSF), as sketched in Fig. D.2 for the azimuth and range directions. In this article, the x, y, and z axes correspond to the azimuth, range, and elevation directions, respectively. Assuming rectangular apodization this region of support would have a triangular shape laterally, with width determined by the angle θ_{lim}:

$$\theta_{lim} = \pm \arctan\left(\frac{1}{2f_{\#}}\right) \tag{D.1}$$

where the F-number $f_{\#}$ is the ratio between the focal length F and the aperture D. The axial shape and size of the bandpass region around approximately twice the spatial frequency $k_0 = 2\pi f_0/c$ (where c is the sound speed in soft tissue) is mainly governed by the bandwidth B and center frequency f_0 of the transmit pulse. In order to be visible by the ultrasound imaging system, an object must have a variation of density and compressibility ("scattering ability") with spatial frequency content within this region of support.

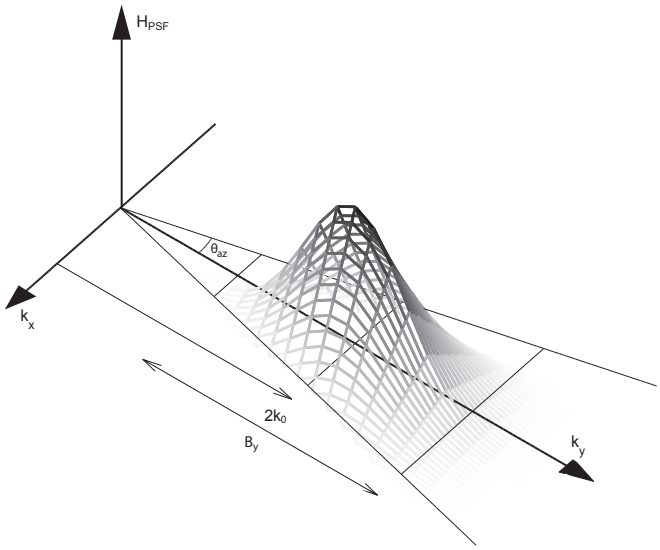

Figure D.2: Sketch of the k-space region of support for an ultrasound imaging system. The figure shows the frequency sensitivity (H_{PSF}) for spatial frequencies in the azimuth (x) and range (y) directions. The symmetric part of the figure for negative values of k_y is omitted for simplicity.

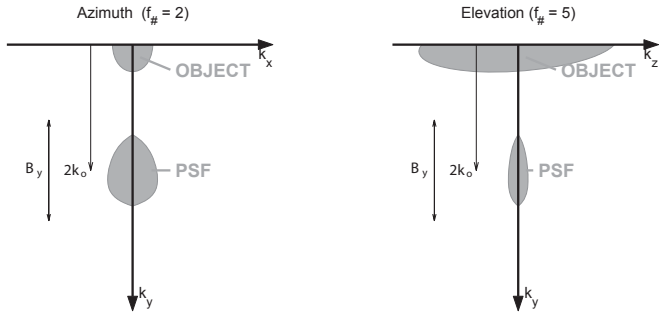

Figure D.3: Sketch of the azimuthal and elevational k-space representations of ultrasound imaging of an anisotropic object with main fiber orientation close to parallel to the beam direction.The symmetric part of the figure for negative values of k_y is omitted for simplicity.

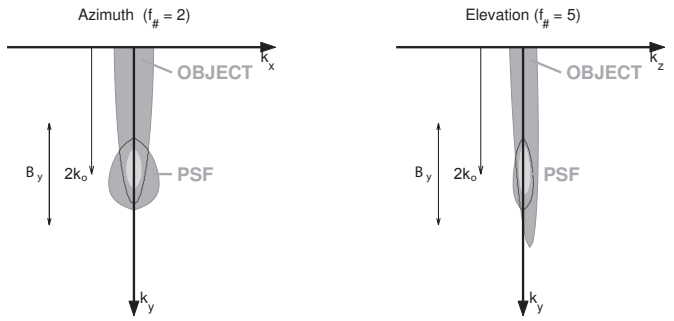

Figure D.4: Sketch of the azimuthal and elevational k-space representations of ultrasound imaging of an anisotropic object with main fiber orientation close to perpendicular to the beam direction.The symmetric part of the figure for negative values of k_y is omitted for simplicity.

While an isotropic medium has a distribution of scatterers that is invariant of the insonification angle, an anisotropic medium has different scatterer correlations in different directions and thereby an angular dependence in the spatial frequency distribution. In this work we assumed that the scatter ability of myocardium has the longest correlation length in the fiber direction, and shorter correlation lengths in the sheet and sheet normal directions. This can be modeled as an ellipsoidal shape in k-space, where the shortest axis of the ellipsoid corresponds to the direction of the muscle with longest correlation length, and vice versa. Figs. D.3 and D.4 show k-space representations of ultrasound imaging using a rectangular aperture of an anisotropic object — modeled as an ellipsoid in k-space — undergoing a rotation in the elevational direction. In Fig. D.3, the direction with longest correlation length is close to parallel to the ultrasound beam, and the corresponding low axial frequency content is not picked up by the system's region of support (PSF). In Fig. D.4, the insonification angle has changed so that the direction with longest correlation length is close to perpendicular to the ultrasound beam and the corresponding high axial frequency content is overlapping the PSF.

D.3 Method

The study was performed in three steps, elaborated below. First, the predominant fiber orientations in a cylindrical sample of the intraventricular septum were determined from *in vitro* images. Second, a model of the sample was constructed, which incorporated the fiber orientations found experimentally. Finally, simulated ultrasound images were generated from the model and compared with the *in vitro* images. The estimation of the fiber orientations, the model generation and the ultrasound simulations were performed by custom-made code in Matlab (The MathWorks, Natick, MA).

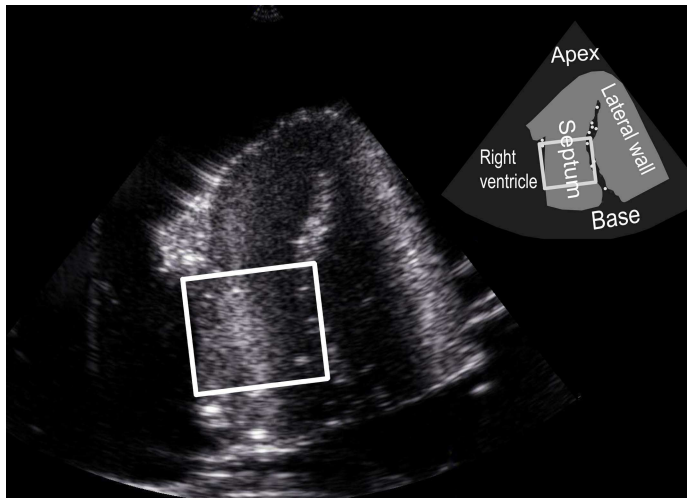

Figure D.5: Collapsed porcine left ventricle. Notice the appearance of a large cavity, despite the fact that the ventricle is collapsed and the only true cavity is seen lined by air bubbles as the bright line from the apex towards the base.

D.3.1 Data acquisition and fiber angle estimation

Data acquisition was performed using a Vivid 7 ultrasound scanner (GE Vingmed Ultrasound, Horten, Norway). The ultrasound image in Fig. D.5 shows the collapsed ventricle of a porcine heart indicating the region of interest for excision. A cylindrical sample was cut from the septum of the heart, as depicted in Fig. D.6(a). The excised specimen was then placed in a water-bath, where it was held in place by a clamp device connected to the shaft of a hybrid stepper motor (Y129, Astrosyn International Technology, Kent, U.K.). The specimen was then rotated in 0.9 degrees steps, in an angle interval between -135 and 135 degrees relative to the circumferential orientation. The experimental setup is shown in Fig. D.6(b). High resolution ultrasound images of the sample were obtained from the range of insonification angles using a 1.25D linear array probe (M12L, GE Vingmed Ultrasound, Horten, Norway) mounted above the sample with the azimuth direction parallel to the axis of rotation.

The angle-dependence of the echo signal from one transmural layer (i.e. from one scan-line) is shown in Fig. D.7. The backscatter intensities in Fig. D.7(b) were estimated by averaging over a 5 mm axial interval, placed close to the probe in order to reduce the effect of angle dependent attenuation, and then normalized relative to the maximal intensity value. The dominating fiber orientation in each transmural position was selected as perpendicular to the insonification angle that resulted in the strongest backscattered signal in the corresponding scan-line. For the layer showed in Fig. D.7, this resulted in a fiber angle of $-25°$. By repeating this for all scan-lines within the specimen, we obtained an expression of the fiber angle as function of transmural position that could be used as input to the anisotropic point scatterer

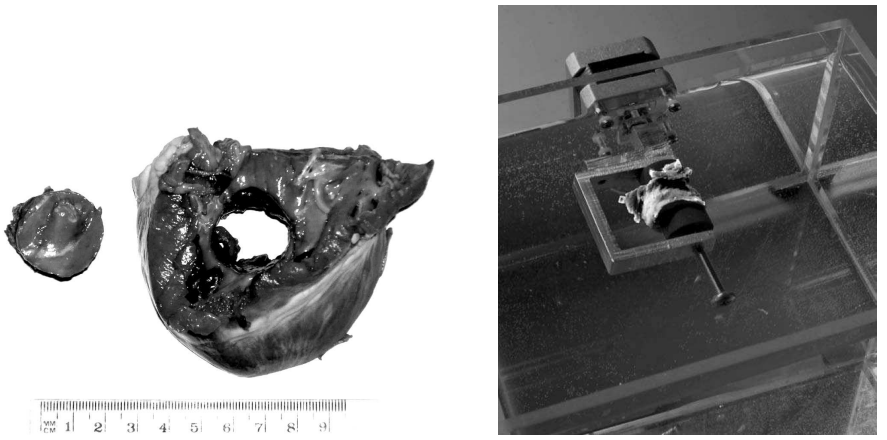

(a) Porcine septum with a cylindrical sample removed.

(b) Measurement setup.

Figure D.6: Data acquisition

model.

For comparison, fiber helix angles determined from the primary eigenvectors from the septal region in diffusion tensor magnetic resonance imaging (DT-MRI) from a different porcine heart of comparable dimensions were also acquired. The DT-MRI helix angles were computed as the angles between the primary DT-MRI eigenvectors and the user-specified circumferential direction using an approach similar to [19].

D.3.2 Point scatterer model

A cylindrical myocardial volume similar to the excised sample (radius: 14.5 mm, thickness: 15.6 mm) was modeled as a regular grid of point scatterers with initially zero-mean Gaussian distributed backscatter coefficients. The scatterer spacing was set to be 30 μm in the longitudinal (i_2) and circumferential (i_1) directions, and 70 μm in the transmural (i_3) direction.

The backscatter coefficients were then correlated in the direction of the muscle fibers found in the experiments by applying a directional smoothing filter on each transmural layer. The filter kernel was defined as an ellipsoidal gaussian function:

$$h \propto \exp\left(-\frac{1}{2}\left(\frac{s_1^2}{\sigma_1^2}+\frac{s_2^2}{\sigma_2^2}+\frac{s_3^2}{\sigma_3^2}\right)\right) \tag{D.2}$$

which in the spatial frequency domain also forms an gaussian ellipsoid:

$$H \propto \exp\left(-\frac{1}{2}\left(\sigma_1^2 k_1^2+\sigma_2^2 k_2^2+\sigma_3^2 k_3^2\right)\right) \tag{D.3}$$

The principal directions of the ellipsoid in eq. D.2 were oriented according to the estimated transmural filter angles $\theta(i_3)$:

$$s_1 = i_1 \cos(\theta(i_3)) - i_2 \sin(\theta(i_3)) \tag{D.4}$$

$$s_2 = i_1 \sin(\theta(i_3)) + i_2 \cos(\theta(i_3)) \tag{D.5}$$

$$s_3 = i_3 \tag{D.6}$$

The full width at half maximum (FWHM) in the principal directions were set to be 0.15 mm in the fiber direction ($\sigma_1 = 64\ \mu m$), 0.06 mm in the orthogonal direction ($\sigma_2 = 26\ \mu m$), and 0.10 mm in the sheet direction ($\sigma_3 = 42\ \mu m$). The sheet direction was set to be perpendicular to the endocardial surfaces.

The coordinates of each scatterer point were rotated stepwise around the center axis in order to achieve a range of insonification angles similar to the experiments.

D.3.3 Ultrasound simulation

Computer-simulated ultrasound images were then generated from the model by using the in-house 3D ultrasound imaging simulation program FUSK (Fast Ultrasound Simulation in K-space) [20]. In FUSK, the point spread function (PSF) is convolved with the point scatterers of the model by multiplication in the frequency domain (K-space), in order to reduce processing time.

The PSF is constructed in the baseband of the spatial frequency domain. The shape of the PSF along the k_y axis is determined by the frequency content of the ultrasound pulse, with reference to Fig. D.2. The shape in the k_x and k_z directions is given by the Fourier transform of the aperture apodization function according to the Fraunhofer approximation [21].

The point scatterers are filtered with a baseband-demodulated antialiasing filter, ensuring that the filter has a wider transition band than the PSF along all dimensions. This approach makes it possible to run the simulation on the coarser beam-space grid, and still handle the sub-resolution motion of scatterers points between frames, which is crucial for the gradual change of the speckle pattern. The ultrasound images are made from the resulting complex demodulated data (IQ-data) by detection, logarithmic compression and scan-conversion. The approximations in FUSK make it possible to run simulations three order of magnitude faster than impulse-response based simulators like Field II [22].

The simulation parameters were set to mimic the M12L linear array probe used in the experiments ($f_0 = 10\ MHz$; $B = 6\ MHz$), and scatterer points far from the imaging plane were excluded prior to simulation.

D.4 Results

The experiments revealed that the fiber orientation changed gradually over 140 degrees through the septal wall (Fig. D.8), from 59.4 degrees near the left ventricle to be almost longitudinal (-83.7 degrees) near the right ventricle. The fiber helix angles determined

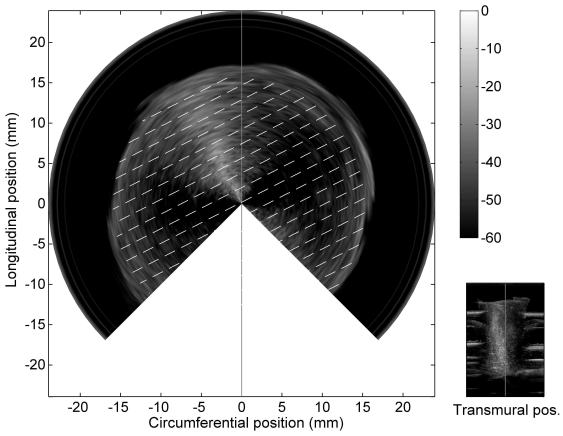

(a) Visualization of the angular dependence of one layer of the septum sample. The transmural position of the layer indicated by the vertical line in the small image to the right. The polar image is constructed from the corresponding beams from a range of insonification angles. The white dashed lines shows the estimated fiber direction in the layer.

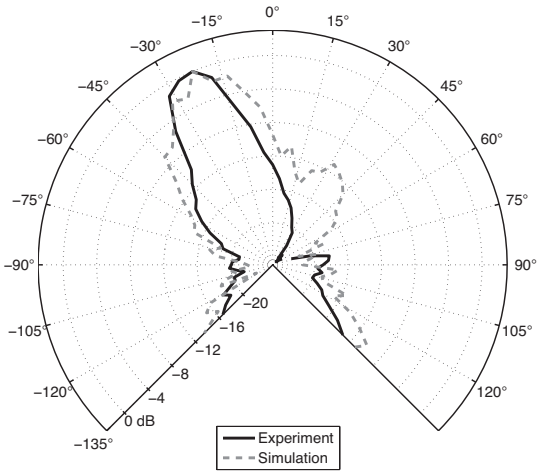

(b) Normalized apparent backscatter intensity versus insonification angle (relative to an apical view) for the transmural layer in (a) estimated from the in vitro recording (solid black line) and estimated from the simulations (dashed gray line).

Figure D.7: Polar plots showing the angular dependency of backscattered signal in a transmural layer of the septum sample. Apex is up in both images.

from DT-MRI (shown as dashed line in the same figure) showed a similar transmural variation. It should be noted that the number spatial resolution in the DT-MRI was much lower than the ultrasonic beam density, giving the DT-MRI fiber angles a more smoother appearance than the unfiltered ultrasound angles.

Fig. D.9 shows the simulated linear array images of the cylindrical specimen for five selected insonification angles. It can be seen that the bright regions in the image shifts transmurally depending on the insonification in the simulation as in the *in vitro* images. A video clip showing the recorded and simulated data during a 270° rotation of the cylindrical specimen can be seen in Fig. D.10. The bright horizontal lines in the *in vitro* recordings in Fig. D.9 on each side of the cylindrical specimen were reflections from the rubber cylinders that are holding the sample. The simulation of each frame containing 35 million scatterers took approximately 35 minutes on a Dell Precision 670n Workstation (Intel Xeon 3.0 GHz processor; 4 GB RAM).

D.5 Discussion and conclusion

Both the dimensions of the individual cardiac myocytes (length: $\sim 130-140\,\mu m$; mean diameter: 18 μm [23]) and the sheets (thickness: $\sim 40\,\mu m$) are below the spatial resolution of an ultrasound imaging systems at clinically useful frequencies. Nevertheless, the amplitude of the backscattered signal will be dependent on the angle between the laminar structures — and the fiber angles — and the local wave-front. If the structures are close to perpendicular to the wave-front, then the specular backscatter can be detected by the aperture.

The fiber angle orientations in this study were estimated using ultrasound. The smooth transmural 140 degree change in fiber angle is similar to observations by DT-MRI in this and previous studies [24, 25]. As the DT-MRI fiber angles found in this study were based on a different heart than with the ultrasound estimates, individual variations in the fiber organization are expected. However, the overall fiber organization is known to be quite similar within mammalian species. The rotational insonification approach using a linear array probe constitutes a new fast method for ultrasound-based determination of fiber helix angles in small cardiac samples, as a convenient alternative to histology or DT-MRI. It is also possible to use fiber and sheet directions found by DT-MRI or histology as input to the model. If the fiber directions are allowed to change in the longitudinal and circumferential directions in addition to transmurally, this is feasible using the proposed approach but would require a more sophisticated filtering scheme. Furthermore, the sheet directions are known to vary transmurally. The sheet angles can be estimated by DT-MRI from the secondary eigenvectors, or by ultrasound, applying the rotational insonification approach in the orthogonal direction.

As seen in Fig. D.9, the simulated images showed a line of increased intensity where the fibers were close to perpendicular to the beam direction, similar to experimental results. In contrast, simulated ultrasound images without tissue anisotropy give a homogenous speckle pattern with no transmural variation in backscatter level, and therefore look the same for all insonification angles (not shown). With knowledge of

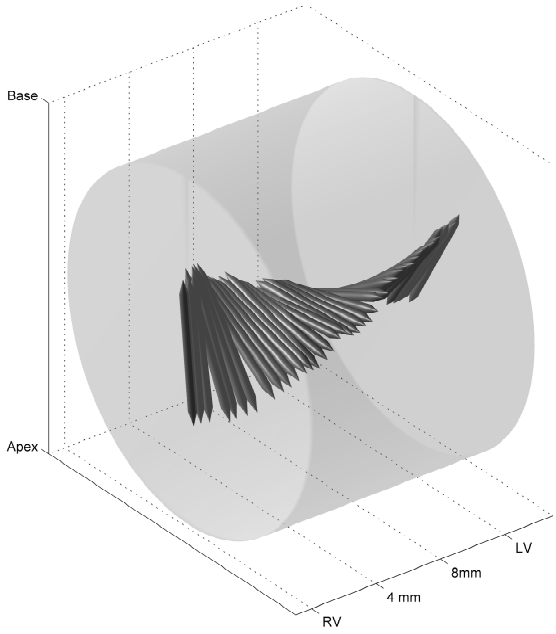

(a) Visualization of the dominating fiber direction in the sample.

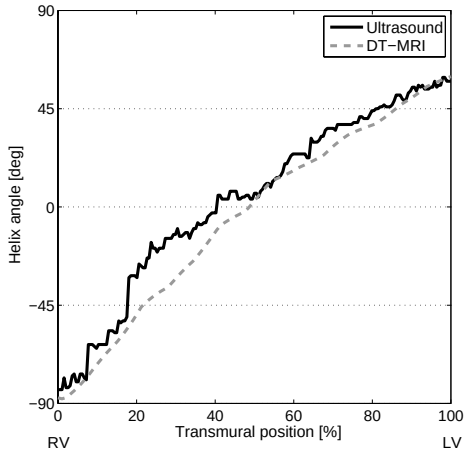

(b) Fiber angle estimated by ultrasound (solid line) in the cylindrical specimen, and septal fiber angle determined by diffusion tensor magnetic resonance imaging (DT-MRI) of a comparable porcine heart (dashed line).

Figure D.8: Transmural fiber orientation estimated by ultrasound.

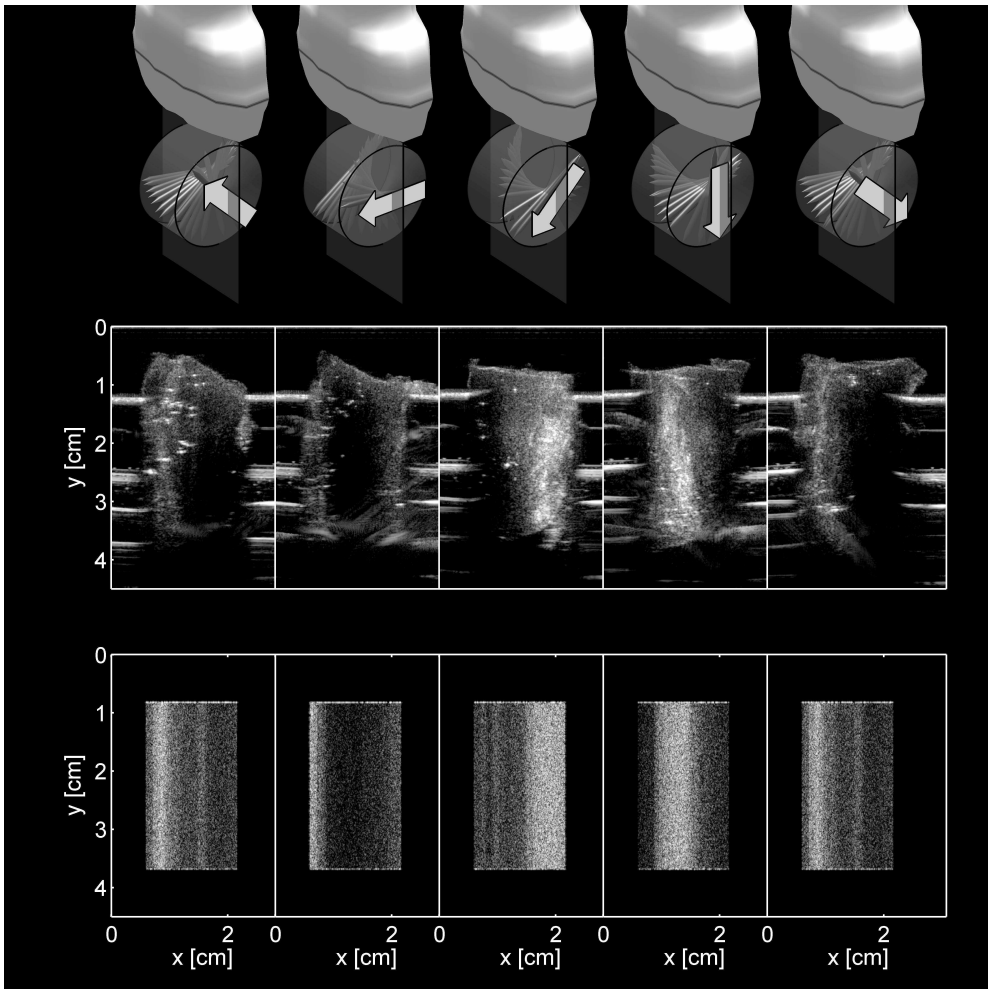

Figure D.9: Simulation results, linear array. The upper row shows the orientation of the cylindrical specimen relative to the transducer for five different insonification angles. The arrow is oriented in the long-axis direction of the heart, pointing towards the base, and the bars within the specimen indicate the estimated fiber directions. The middle row shows sections of the *in vitro* ultrasound images of the specimen for the five different insonification angles. The lower row shows the corresponding simulated images. In the ultrasound images, the right ventricle would be to the left of the specimen and the left ventricle to the right.

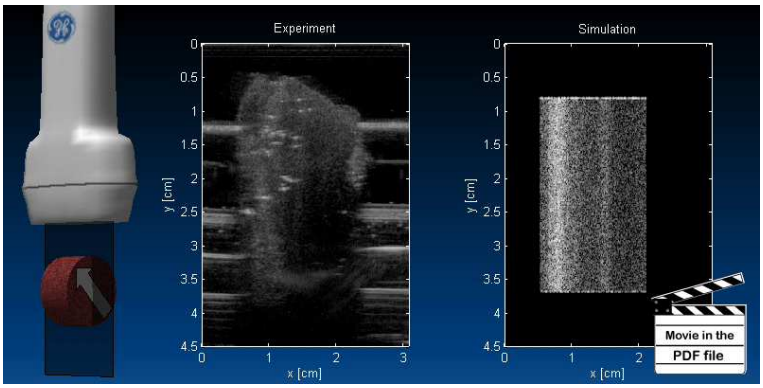

Figure D.10: A video clip showing the recorded and simulated data during a 270° rotation of the cylindrical specimen. The electronic version of this document, containing the movie, can be found at http://urn.kb.se/resolve?urn=urn:nbn:no:ntnu:diva-5937.

the PSF of the imaging systems, it should be possible to tune the filter parameters to correspond with experimental angular backscatter profiles, but this is beyond the scope of the current study. The autocorrelation lengths could also be found directly using for example acoustic microscopy. An earlier acoustic microscopy study [26] reports fiber autocorrelation lengths much lower ($37 \pm 18\ \mu m$) than the filter lengths in our model. However, the limited region of interest in that study might have neglected the contribution from larger structures such as the cleavage planes reported in [15].

Some weaker bands of increased intensities were also visible in the simulation results that did not appear in the *in vitro* recordings. These bands were most conspicuous where the scatterer grid was rotated 45 degrees relative to the initial configuration, and could be an artifact of the filtering of the ordered grid.

In this study, the angular dependence of attenuation was neglected as this effect is difficult to model just based on geometrical considerations. Consequently, the simulation do not reproduce the increased weakening of the signal when the beam is orientated close to parallel with the fibers, as seen in the experimental results in Fig. D.9. The difference in attenuation between parallel and perpendicular insonification has been found to amount to 0.8 $dB\,cm^{-1}MHz^{-1}$ [10]. One way to include this attenuation, is to specify an attenuation coefficient for each point depending on the local fiber angle based on attenuation values found from experiments, as done in the work by Holland et al. [11].

The vast number of scatterer points in this study is a consequence of the high imaging frequency. In simulations at clinically relevant frequency around 2 MHz, the grid resolution — and thereby the simulation time — can be significantly reduced. Although the FUSK method was applied in this study, the anisotropic model is not limited to this simulation tool. Established ultrasound simulation software as the Field II package could very well be used to perform the simulations but at the cost of much higher simulation time.

It is evident that the anisotropic behavior of the myocardium has a significant effect on ultrasound images of myocardium. Myocardial anisotropy could possibly affect the performance of edge (or surface) detection methods as it introduces varying image-intensities within the wall and might also cause false motion in tissue tracking methods. Simulated ultrasound images that includes the effect of fiber orientation thus provide a more realistic test to assess the accuracy of such methods. The scatterer model approach proposed in this paper constitutes a simple and flexible — although not quantitatively accurate — way to reproduce the regional view-dependent variation in backscatter seen in real ultrasound images of the heart. The anisotropic models can easily be used with existing ultrasound simulation software, without the need of passing additional information of the fiber geometry to the simulator.

Acknowledgment

The authors gratefully acknowledge the assistance of Prof. Atle Bjørnerud and Dr. Frédéric Courivaud at the Interventional Centre at Rikshospitalet University Hospital, Oslo, Norway, in the acquisition of DT-MRI data.

References

[1] J. A. Jensen and S. I. Nikolov, "Fast simulation of ultrasound images," in *IEEE International Ultrasonics Symposium Proceedings*, pp. 1721–1724, 2000.

[2] K. Liu, J. Bai, and Y. Jiang, "Computer simulation model on ultrasonic myocardial backscatter," *Ultrasonics*, vol. 44 Suppl 1, pp. e261–269, Dec 2006.

[3] Q. Duan, P. Moireau, E. Angelini, D. Chapelle, and L. A.F., "Simulation of 3d ultrasound with a realistic electro-mechanical model of the heart," in *Proceedings of FIMH'07 Conference*, (Salt Lake City, USA), pp. 463–470, June 2007.

[4] M. Aygen and R. L. Popp, "Influence of the orientation of myocardial fibers on echocardiographic images," *The American Journal of Cardiology*, vol. 60, pp. 147–152, Jul 1987.

[5] J. G. Mottley and J. G. Miller, "Anisotropy of the ultrasonic backscatter of myocardial tissue: I. Theory and measurements in vitro," *The Journal of the Acoustical Society of America*, vol. 83, pp. 755–761, Feb 1988.

[6] E. I. Madaras, J. Perez, B. E. Sobel, J. G. Mottley, and J. G. Miller, "Anisotropy of the ultrasonic backscatter of myocardial tissue: II. Measurements in vivo," *The Journal of the Acoustical Society of America*, vol. 83, pp. 762–769, Feb 1988.

[7] J. G. Mottley and J. G. Miller, "Anisotropy of the ultrasonic attenuation in soft tissues: measurements in vitro," *The Journal of the Acoustical Society of America*, vol. 88, pp. 1203–1210, Sep 1990.

[8] D. Recchia, C. S. Hall, R. K. Shepard, J. G. Miller, and S. A. Wickline, "Mechanism of the view-dependence of ultrasonic backscatter fromnormal myocardium," *IEEE Transactions on Ultrasonics, Ferroelectrics and Frequency Control*, vol. 42, pp. 91–98, Jan. 1995.

[9] J. G. Miller, J. E. Perez, S. A. Wickline, S. L. Baldwin, B. Barzilai, V. Davila-Roman, R. J. Fedewa, A. E. Finch-Johnston, C. S. Hall, S. M. Handley, F. D. Hockett, M. R. Holland, A. Kovacs, G. M. Lanza, S. H. Lewis, J. N. Marsh, J. Mobley, D. E. Sosnovik, R. L. Trousil, K. D. Wallace, and K. R. Waters, "Backscatter imaging and myocardial tissue characterization," in *Ultrasonics*

Symposium, 1998. Proceedings., 1998 IEEE, vol. 2, (Sendai, Japan), pp. 1373–1383, 1998.

[10] S. Baldwin, M. Yang, K. Marutyan, K. Wallace, M. Holland, and J. Miller, "Influence of bright intramural echoes on estimates of ultrasonic attenuation from backscattered ultrasound in excised myocardium," *Ultrasonic Imaging*, vol. 26, pp. 233–249, Oct 2004.

[11] M. Holland, U. Wilkenshoff, A. Finch-Johnston, S. Handley, J. Perez, and J. Miller, "Effects of myocardial fiber orientation in echocardiography: Quantitative measurements and computer simulation of the regional dependence of backscattered ultrasound in the parasternal short-axis view," *Journal of the Acoustical Society of America*, vol. 11, pp. 929–937, Oct 1998.

[12] M. R. Holland, A. Kovacs, S. H. Posdamer, K. D. Wallace, and J. G. Miller, "Anisotropy of apparent backscatter in the short-axis view of mouse hearts," *Ultrasound in Medicine & Biology*, vol. 31, pp. 1623–1629, Dec 2005.

[13] M. Santarelli and L. Landini, "A model of ultrasound backscatter for the assessment of myocardial tissue structure and architecture," *IEEE Transactions on Biomedical Engineering*, vol. 43, pp. 901–911, Sep 1996.

[14] D. D. Streeter Jr. and D. L. Bassett, "An engineering analysis of myocardial fiber orientation in pig's left ventricle in systole," *The Anatomical Record*, vol. 155, pp. 503–511, Aug 1966.

[15] I. LeGrice, B. Smaill, L. Chai, S. Edgar, J. Gavin, and P. Hunter, "Laminar structure of the heart: ventricular myocyte arrangement and connective tissue architecture in the dog," *American Journal of Physiology*, vol. 269, pp. H571–582, Aug 1995.

[16] W. Tseng, V. Wedeen, T. Reese, R. Smith, and E. Halpern, "Diffusion tensor MRI of myocardial fibers and sheets: correspondence with visible cut-face texture," *Journal of Magnetic Resonance Imaging*, vol. 17, pp. 31–42, Jan 2003.

[17] R. Lerner and R. Waag, "Wave space interpretation of scattered ultrasound," *Ultrasound in Medicine & Biology*, vol. 14, pp. 97–102, 1988.

[18] M. E. Anderson and G. E. Trahey, *A seminar on k-space applied to medical ultrasound*. Department of Biomedical Engineering, Duke University, Feb 2006.

[19] E. Wu, Y. Wu, J. Nicholls, J. Wang, S. Liao, S. Zhu, C. Lau, and H. Tse, "MR diffusion tensor imaging study of postinfarct myocardium structural remodeling in a porcine model," *Magnetic Resonance in Medicine*, vol. 58, pp. 687–695, Oct 2007.

[20] T. Hergum, J. Crosby, M. Langhammer, and H. Torp, "The effect of including fiber orientation in simulated 3D ultrasound images of the heart," *proceedings of the IEEE Ultrasonics Symposium*, pp. 1991–1994, 2006.

[21] W. F. Walker and G. E. Trahey, "The application of k-space in pulse echo ultrasound," *IEEE Transactions on Ultrasonics, Ferroelectrics, and Frequency Control*, vol. 45, pp. 541–558, 1998.

[22] J. Jensen, "Simulation of advanced ultrasound systems using Field II," in *IEEE International Symposium on Biomedical Imaging: Nano to Macro*, vol. 1, pp. 636–639, 2004.

[23] A. Gerdes and J. Capasso, "Structural remodeling and mechanical dysfunction of cardiac myocytes in heart failure," *Journal of Molecular and Cellular Cardiology*, vol. 27, pp. 849–856, Mar 1995.

[24] P. Schmid, T. Jaermann, P. Boesiger, P. F. Niederer, P. P. Lunkenheimer, C. W. Cryer, and R. H. Anderson, "Ventricular myocardial architecture as visualised in postmortem swine hearts using magnetic resonance diffusion tensor imaging," *European Journal of Cardio-Thoracic Surgery*, vol. 27, pp. 468–472, Mar 2005.

[25] L. Geerts, P. Bovendeerd, K. Nicolay, and T. Atrs, "Characterization of the normal cardiac myofiber field in goat measured with MR-diffusion tensor imaging," *American Journal of Physiology, Heart and Circulatory Physiology*, vol. 283, pp. H139–H145, Feb 2002.

[26] D. T. Linker, B. A. Angelsen, and R. L. Popp, "Autocorrelation length of normal and myopathic human myocardium measured by acoustic microscopy: implications for clinical ultrasonic tissue characterization," *Ultrasound in Medicine & Biology*, vol. 16, no. 8, pp. 793–799, 1990.

Paper E

Quantification of Valvular Regurgitation Area and Geometry using HPRF 3D Doppler

Torbjørn Hergum[1], Thomas Renhult Skaug[1], Knut Matre[2] and Hans Torp[1]

[1]Department of Circulation and Medical Imaging, NTNU, Trondheim, Norway

[2]Institute of Medicine, University of Bergen, Bergen, Norway

Abstract

It is important to determine the severity of valvular regurgitation accurately because surgery is indicated only in severe regurgitations. The evaluation of, for example, mitral regurgitation is complex, and the current methods have limitations. We have developed a 3-D Doppler method to estimate the cross-sectional area and the geometry of a regurgitant jet at the vena contracta just downstream from the actual orifice. The back-scattered Doppler signal from multiple beams distributed over the area of interest was measured. The received power from these beams was then calibrated using both a priori knowledge of the lateral extent of the beams and a reference beam that was completely enclosed by the vena contracta. To isolate the Doppler signal received from the core of a regurgitant jet, a high pulse repetition frequency and a steep clutter filter are required. The method has been implemented and verified by computer simulations and by in vitro experiments using a pulsatile flow phantom and prosthetic valves with a range of holes. We were able to distinguish between mild, moderate, and severe valvular regurgitation. We were also able to quantify the regurgitational area as well as show the geometry of the regurgitation.

IEEE Transactions on UFFC, vol. 56, no. 5, pp. 975–82, 2009

E.1 Introduction

Quantification of mitral regurgitation is a predictor of mortality and also provides support for early intervention in asymptomatic patients [1]. Semiquantitative parameters include the Doppler-intensity of the regurgitant CW-signal, mitral flow and pulmonary vein flow velocities measured by pulsed wave (PW)- Doppler, and the regurgitant jet size measured by color flow imaging (CFI). These parameters are dependent on loading conditions and instrument settings such as gain and the Nyquist limit, and regurgitant jets measured by CFI are influenced by blood entrainment [2].

Quantification by the proximal isovelocity surface area (PISA)method assumes a flat plane and a circular regurgitant orifice. Functional mitral regurgitation (MR) tends to be underestimated by this method due to asymmetry of the geometry [3].

Vena contracta is defined as the narrowest part of a jet, typically found a few millimeters distal to the orifice. The blood flow in the vena contracta is laminar. Using 2-D color flow to measure the width of the vena contracta has been validated against angiography and is recommended by the European Society of Cardiology as a measure of mitral regurgitation severity [2, 4]. All the methods above have limitations due to 3-D assumptions of 2-dimensionally derived shapes, dimensions, and velocity profiles. The cross-sectional area (CSA) of the vena contracta measured by 3-D CFI and systematic cropping of the data set have shown better correlation with angiographic grading than using the vena contracta width as measured by 2D color flow [5]. Similar studies have been carried out with aortic and tricuspid regurgitation [6, 7].

A mitral regurgitation jet can have a velocity of $4 - 6\ m/s$, and CFI typically has a maximum Nyquist frequency of $1\ m/s$, making the Doppler signal alias several times and get the high bandwidth characteristics of turbulence. Fluid entrainment, arbitrary gain settings, and poor resolution add to the problem of determining the border of the jet.

Measuring volume flow rate with ultrasound has been done by multiplying the average blood velocity found by Doppler with the cross-sectional area of the vessel found from B-mode. However, this has several limitations [8, 9]. A different approach is based on the principle that for laminar flow and constant hematocrit the backscattered power from blood is proportional to the volume of blood within the sample volume of an ultrasound beam [10]. This is called a *measurement beam*. The factor of proportionality needs to be determined to obtain an estimate of the blood volume using a narrow *reference beam* of known cross-sectional area that is totally covered by the blood flow. This principle was initially used to measure the volume flow in arteries [11], but it failed to gain popularity due to problems with a very large area to cover with one beam and a large distribution of blood velocities within the beam. Later, Buck *et. al.* have used the method to quantify volume flow through the vena contracta of regurgitant jets [12–14], because such jets have a narrow velocity distribution and limited size. One drawback of this method is that the sensitivity of the measurement beam is assumed to be homogeneous over the area of the jet. This is usually not the case, because a transducer typically uses a rectangular aperture that gives a *sinc*-shaped beam profile. Additionally, the sensitivities of the measurement and reference beam are different, and the positioning of the beam is critical. No information about

the geometry of the orifice is found.

We propose using the sum of several narrow beams as a composite measurement beam and selecting one of these as the reference beam. This approach will ensure a more homogeneous sensitivity and less critical positioning of the sample volume, and it will have the added benefit of providing a geometry estimate of the effective orifice. For a thin disklike sample volume, the power of the composite measurement beam will be proportional to the cross-sectional area of the jet; thus, the method can be used to estimate the CSA of the vena contracta. If an estimate of the blood velocity in the jet is found, the flow rate can be calculated as the product of the CSA and the velocity time integral (VTI) or the mean velocity.

The ultrasound data are acquired using a 3-D high pulse repetition frequency (HPRF) Doppler modality, where the PRF is typically above 20 kHz and the packet size is 8 to 16 as for color-flow acquisition. The resulting Nyquist limit ranges from 3 to 5 m/s depending on the transmitted frequency. Despite transmitting a packet of pulses in each direction, the acquisition time is much shorter than CFI due to the high pulse repetition frequency.

Initially, the details of the quantification method are shown, followed by results showing that the method works well in a computer simulation. Encouraged by the simulation results, we have tested the method in a pulsatile flow phantom, using a blood-mimicking fluid and porcine valves with orifices of known sizes.

E.2 Theory

Fig. E.1 shows a leaking valve where several beams are indicated. We want to combine these beams into a composite measurement beam and also select one of the beams as a reference beam. The ratio of the expected power from the composite beam and the reference beam must also be found because they do not have the same sensitivity.

Let $g(x, y)$ be the pulse-echo beam profile, where x and y are the azimuth- and elevation-axis coordinates. N beams are positioned at (x_k, y_k), $k = 1 : N$. The two-way beam profile of the beam positioned at position k is denoted $g_k(x, y)$.

Let $s_k(\tau)$ be the RF signal from a beam steered towards (x_k, y_k), where τ is the time delay after pulse transmission ("fast time"). The expected power received from this beam is

$$< |s_k(\tau)|^2 > = \int_{-\infty}^{\infty} \sigma(x, y)|g_k(x, y, \tau)|^2 dxdy \tag{E.1}$$

where $\sigma(x, y)$ accounts for the scattering cross section, frequency-dependent attenuation, and the effect of a clutter filter. Specifically, the clutter filter will make $\sigma(x, y)$ equal to zero outside the jet. The impulse response of the clutter filter can be included with an additional convolution integral, but this has been omitted for notational simplicity.

To obtain data from the whole orifice, several such beams are combined. The

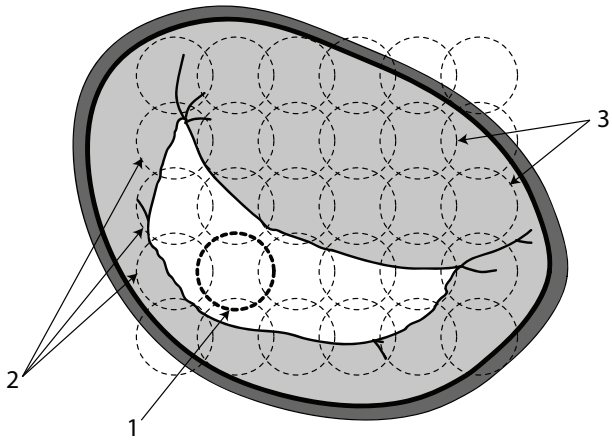

Figure E.1: Sketch of a leaking valve with multiple beams indicated. Beam 1 is totally inside the orifice and is selected as the reference beam. Several beams are partially overlapping with the orifice, for instance the beams labeled 2. The combined power from these beams acts as the measurement beam. Finally, a lot of beams are outside the orifice, like those labeled 3, which will not contribute to the measurement because the signal will be removed by the clutter filter.

expected total received power from these beams is given by

$$\begin{aligned} P_w &= \sum_k < |s_k(\tau)|^2 > \\ &= \int_{-\infty}^{\infty} \sum_k \sigma(x,y)|g_k(x,y,\tau)|^2 dxdy \\ &= \int_{CSA_{jet}} \sigma(x,y) G_w(x,y,\tau) dxdy \end{aligned} \tag{E.2}$$

where <> denotes expectation value and the integration in (E.2) is taken over the CSA of the jet, because this is the only area with scatterers moving fast enough to escape the clutter-filter. $G_w(x,y,\tau)$ is the two-way power beam profile of the composite beam,

$$G_w(x,y,\tau) = \sum_k |g_k(x,y,\tau)|^2. \tag{E.3}$$

A simulated example of this function is shown for a 1-D case in Fig. E.2 where 9 pulse-echo power beam profiles from a rectangular aperture are summed to produce the composite 2-way power beam profile $g_w(x,y,\tau)$.

If one of the narrow beams is totally enclosed within the CSA, $k = ref$, the

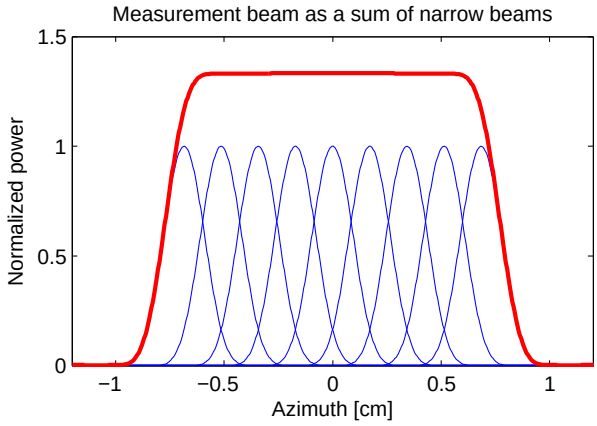

Figure E.2: A composite measurement beam is made by adding up multiple narrow beams. Here 9 narrow beams from a rectangular aperture are added up to make a wide, flat beam. The beam spacing is set to half the Rayleigh criterion. With a less dense spacing, the measurement beam will have ripples. The power is normalized to the maximum value of the narrow beams to show that the sensitivity of the measurement beam is higher than each of the narrow beams.

expected received power from this beam is

$$\begin{aligned} P_{ref}(\tau) &= < |s_{ref}(\tau)|^2 > \\ &= \int_{-\infty}^{\infty} \sigma(x,y)|g_{ref}(x,y,\tau)|^2 dxdy \end{aligned} \tag{E.4}$$

$$\tag{E.5}$$

The estimate $\hat{P}_w(\tau)$ of $P_w(\tau)$ can be found from the recorded signals $s_k(\tau)$ by

$$\hat{P}_w(\tau) = \sum_k |s_k(\tau)|^2 \tag{E.6}$$

Similarly the estimate $\hat{P}_{ref}(\tau)$ of $P_{ref}(\tau)$ is

$$\begin{aligned} \hat{P}_{ref}(\tau) &= |s_{ref}(\tau)|^2 \\ &= \max_{k=1:N} \left[|s_k(\tau)|^2 \right] \end{aligned} \tag{E.7}$$

where $s_{ref}(\tau)$ is the reference beam, found as the beam with most power.

The variance of the estimates $\hat{P}_w$ and $\hat{P}_{ref}$ can be reduced by averaging over time and/or space. Radially this is done by averaging the estimates for several values of τ. Time averaging is done by smoothing in "slow time", that is, by combining several subsequent estimates from the same position in space with the same τ.

The ratio between the power of the measurement beam and the power of the reference beam is

$$\frac{P_w}{P_{ref}} = \frac{\int_{-\infty}^{\infty} \sum_k \sigma(x,y)|g_k(x,y,\tau)|^2 dxdy}{\int_{-\infty}^{\infty} \sigma(x,y)|g_{ref}(x,y,\tau)|^2 dxdy} \tag{E.8}$$

and with substitution of the composite measurement beam profile from (E.3):

$$\frac{P_w}{P_{ref}} = \frac{\int_{CSA_{jet}} \sigma(x,y)G_w(x,y,\tau)dxdy}{\int_{-\infty}^{\infty} \sigma(x,y)|g_{ref}(x,y,\tau)|^2 dxdy} \tag{E.9}$$

When the beam density is high and the measurement beam extends beyond the area of the jet, the two-way power beam profile of the measurement beam, $G_w(x,y)$, is close to constant over the jet area. In other words, $G_w(x,y)$ is independent of x and y in the above integration. When $\sigma(x,y)$ is approximated as constant within the orifice and zero outside, (E.9) reduces to

$$\frac{P_w}{P_{ref}} = \frac{G_w CSA_{jet}}{\Gamma_{ref}} \tag{E.10}$$

where CSA_{jet} is the cross-sectional area of the jet and the expected power of the reference beam is

$$\Gamma_{ref}(\tau) = \int_{-\infty}^{\infty} |g_{ref}(x,y,\tau)|^2 dxdy. \tag{E.11}$$

When $G_w(x,y)$ is not constant, it can be approximated with its average or maximum value within the area of the jet.

The cross-sectional area can now be estimated from the recorded data by rearranging (E.10) and substituting P_w and P_{ref} with their corresponding estimated values $\hat{P}_w$ and $\hat{P}_{ref}$:

$$\hat{CSA}_{jet} = \frac{\hat{P}_w}{\hat{P}_{ref}} \frac{\Gamma_{ref}}{G_w} \tag{E.12}$$

Angle (in)dependence

The area estimation is angle dependent. When the ultrasound beam is at an angle θ with the area surface normal it will be overestimated by

$$CSA_{measured} = \frac{CSA_{true}}{\cos(\theta)} \tag{E.13}$$

For the estimation of flow, however, the $\cos(\theta)$ angle dependence of the Doppler technique effectively cancels the $\cos(\theta)$ dependence of the area estimate, so the flow estimate is angle independent. However the angle θ must be so small that $v\cos(\theta)$ is still large enough to be effectively separated from the clutter and slow-moving blood by clutter filtering, v is the speed of the blood.

E.3 Methods

To validate the theory outlined above, we have implemented the procedure using Matlab (The MathWorks, Natick, MA) and have acquired input data from simulations and from in vitro measurements.

Doppler simulations

Ultrasound Doppler signals are stochastic variables, so estimating the reference beam as the beam with most power will give a biased estimate if there is more than one beam to choose from. A simple simulation has been made to investigate this, using zero mean complex Gaussian IQ data. (IQ data are the complex in-phase and quadrature components of baseband demodulated RF-data.) The simulation takes into account the number of range samples in the sample volume and the packet size to see how the expected value of the reference beam changes with the number of beams in the vena contracta.

Another simulation was made to investigate the estimated cross-sectional area of the vena contracta. It uses the Fraunhofer approximation to calculate the point spread function at the focal depth and calculates the estimated area of a range of orifices. For simplicity, the orifice geometries are circular.

A stochastic variation was added to the simulation by including a 2-D Doppler signal model adapted from [15], and using the settings in Table E.1. These settings will later be used in the in vitro recordings. No clutter was added to the signal.

In Vitro Using a Pulsatile Flow Phantom

To further validate the method, we used a pulsatile flow phantom, illustrated in Fig. E.3, which consisted of a modified peristaltic pump (Sarns type 15200; Sarns Inc./3M, Ann Arbor,MI), tubing, an arterial filter, and a chamber to mimic the left atrium and ventricle. Six prosthetic porcine valves (Carpentier-Edwards models 6625 and 6650; Edwards Lifesciences, Irvine, CA) with precisely cut holes were inserted into the phantom to provide regurgitation severities ranging from mild (less than 0.2 cm^2) to severe (more than 0.4 cm^2) [16]. One such valve is pictured in Fig. E.4. The true area of the cut orifices was found from planimetry of photographs.

The phantom was filled with a blood-mimicking fluid based on the recipes found in [17, 18] using ultrafine polyamide particles (Orgasol; ELF Atochem, Paris, France) with diameters of 5 μm as the scattering agent. The specified amount of Dextran made the attenuation too large for successful recording, so we reduced the quantity by 50%,

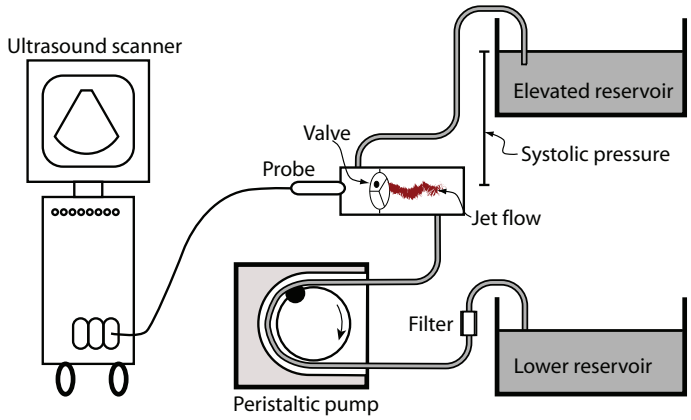

Figure E.3: Illustration of the *in vitro* flow phantom. The systolic pressure was generated by the height difference from the elevated reservoir to the valve. The peristaltic pump, which has one of its rollers removed, acts as a left ventricular relaxation pump and counteracts the systolic pressure during diastole.

which resulted in good readings. We also substituted the surfactant because we found that *Sun Glansemiddel*, (Lilleborg AS, Oslo, Norway), a surfactant used for automatic washing machines, made less foam than the ingredients in the original recipe.

Several recordings were made for each orifice size, some with stationary flow and some with pulsatile flow at 60 beats/min. The arterial filter was included to remove any clotted Orgasol and trap air bubbles. Unfortunately, it gradually reduced the concentration of Orgasol, so a spoonful of an Orgasol+surfactant mixture was added to the blood-mimicking fluid when swapping valves. Therefore, the particle concentration was not kept constant. A Vivid 7 Dimension with a 3V matrix array probe (GE Vingmed, Horten, Norway) was used to obtain the ultrasound data. The most important settings are specified in Table E.1.

The size of the 3-D sample volume consisting of the numerous beams of the composite measurement beam is limited in the radial direction from the high pulse repetition frequency and laterally from frame rate requirements. In a clinical application, the size of the region of interest (ROI) is large enough to span most mitral regurgitation orifices, which rarely are more than $2cm$ long. We were doing the acquisition in 2 steps to make sure the vena contracta was inside the sample volume. The operator found the region of interest ROI using a B-mode, HPRF PW, and 2-D CF triplex mode as is shown in Fig. E.5. Vena contracta was found by searching for a region with a combination of high velocity, low spectral bandwidth, and high power. Subsequently, the ROI was scanned using a real-time 3-D HPRF Doppler mode.

The transmit frequency f_0 and the PRF was chosen with a reasonable trade-off. A high PRF and low f_0 is desirable to obtain a high Nyquist frequency, necessary to resolve velocities on the order of 5 m/s. At the same time a high transmit frequency is desired to increase the resolution to enable the correct estimation of small orifices and

Figure E.4: Prosthetic porcine valve used with the *in vitro* validation study. The true size of the orifice is determined by planimetry of photographs.

to get better geometry estimates. A higher frequency will also increase the scattering from blood [10].

The received data from the 3-D sample volume was filtered with a fourth-order polynomial regression clutter filter to remove the signal from clutter and slowly moving blood in the range-ambiguous sample volumes [19]. When the pump had been engaged to get pulsatile flow, the frames not corresponding to the systole were automatically removed based on the signal power after clutter filtering. Radial and temporal smoothing was applied to reduce the stochastic variation of the estimates. A reference beam was selected as the beam with most power after clutter filtering.

The calibration factor Γ_r/G_w from (E.12) was calculated for the current probe and scanning parameters. The beam profiles were found simply by using the Fourier transform of the aperture, as given by the Fraunhofer approximation. More sophisticated ultrasound simulation software like *Field II* (linear) [20] or *Abersim* (nonlinear) [21] can be used at the cost of several orders of magnitude slower processing. Finally, the CSA of the vena contracta was estimated from (E.12).

The geometry estimate was obtained as the high-pass filtered, radially smoothed, and laterally interpolated power Doppler azimuth-elevation image.

In the methodology proposed by Buck *et. al.* [12–14] the location of the vena contracta is found using 2-D CF and PW in a way similar to the currently proposed method. After finding the region of interest, however, the 2 methods differ significantly. Buck *et. al.* acquires 2, 1-D signals, one narrow reference beam and one wide measurement beam. The 2 Doppler spectrums are then traced, the VTI and the calibration factor is calculated, and the user is presented estimates of the average cross-sectional area of the vena contracta and the total regurgitant stroke volume. In comparison, our proposed method acquires a 3-D volume of Doppler data instead of a 1-D beam. This volume of data is then for the time being analyzed offline, where

Table E.1: Simulation and In Vitro Parameters

Parameter	Value
Center frequency f_0	2.1 MHz
Pulse length	5.5 periods
PRF	21 kHz
ROI size (az*el*range)	19.2x18.0x8.0 mm
Volume rate	7 (real time)
Tx azimuth $f-$number	5.9
Rx azimuth $f-$number	4.7
Tx elevation $f-$number	7.8
Rx elevation $f-$number	5.6
Focal depth	8.9 cm
Packetsize	8
Temporal smoothing	4 frames
Radial smoothing	3.2 mm

the low-velocity signals are removed, a reference beam is selected automatically, the total Doppler power from the jet is found, and the calibration factor is calculated as described in the previous section. Only the signals from the high-velocity core of the jet remain, and the user is presented a 2-D image of the jet core at the vena contracta together with an estimate of the cross-sectional area.

E.4 Results

With an unknown number of beams intersecting the vena contracta, it is not trivial to find an accurate estimate of the power of the reference beam. We are simply using the maximum value as described earlier and have investigated how much this will bias the power estimate of the reference beam with an increasing number of candidate beams. The result is shown in Fig. E.6.

A biased reference beam will influence the estimate of the CSA. Simulation results showing the histogram of CSA estimates with a fixed orifice size are shown in Fig. E.7.

Now varying the size of the orifice, the mean value of the estimated CSA is plotted with a dashed line in Fig. E.8. Omitting the stochastic variation of the Doppler signal model gives a different result, which is plotted with a solid line in the same figure.

The flow phantom was built to mimic mitral regurgitation. Fig. E.5 displays a typical example from the use of the phantom, showing a triplex mode of B-mode, 2-D color flow, and a HPRF PW Doppler spectrum. The PW Doppler sample volume is positioned in the vena contracta, as can be seen by examining the velocity and bandwidth of the spectrum.

In addition to the simulated results, Fig. E.8 shows the estimated and true area for several orifice sizes used in the flow phantom. Each data point is the result of a single recording, where the recordings are made by alternating stationary and pulsatile flow.

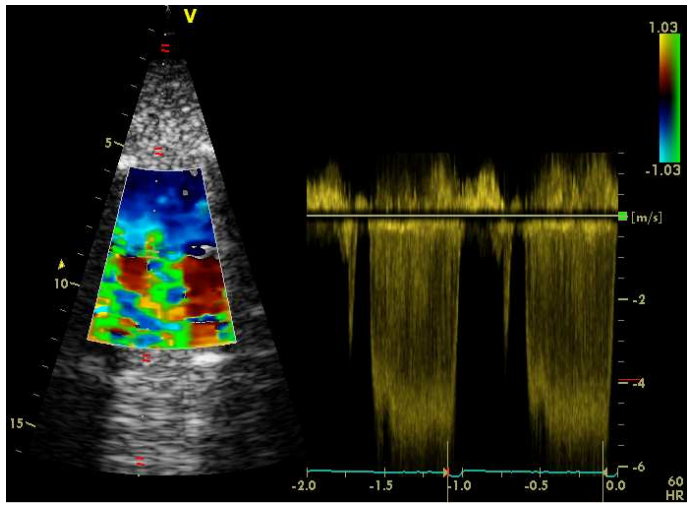

Figure E.5: An example of a triplex image, showing jet flow using the flow phantom and an approximately circular orifice with a 6mm diameter.

The sample volume is repositioned for each recording. Results from both stationary and pulsatile flow are included. Please note the trend of the data, and how it compares to the simulations.

A photograph of a prosthetic valve with a nearly circular orifice of 4.2mm diameter is shown side by side with the corresponding geometry estimate in Fig E.9. The scaling of the images is equal, please note the blurring effect of the limited ultrasound resolution.

E.5 Discussion

In this study, we have developed and tested a 3-D HPRF Doppler method for quantification of valvular regurgitation size and estimation of the geometry of the lesion. It has been examined both by simulations and in vitro.

The Doppler spectrum shown in Fig. E.5 has a peak velocity near 5 m/s which is typical for a mitral regurgitant jet. The narrow bandwidth indicates that the sample volume coincides with the vena contracta region. Moving the sample volume a few millimeters in any direction makes the Doppler signal cover the whole band from zero to the peak velocity. It is also worth noting that the hemispheric inflow region needed to use the PISA method is not easily seen. The very narrow, negative peak in the spectrum before systole is caused by a flapping of the valve before it closes properly.

The simulated and in vitro results plotted in Fig. E.8 demonstrate that the proposed method is able to quantify valvular regurgitation. When the orifice CSA is smaller than the ultrasound beam, the areas are overestimated as expected, because the reference beam can no longer fit inside the small orifice and the calibration of the

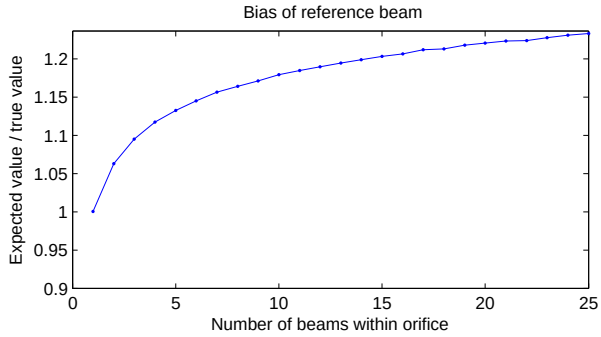

Figure E.6: The reference beam is increasingly overestimated when more beams are included in the orifice.

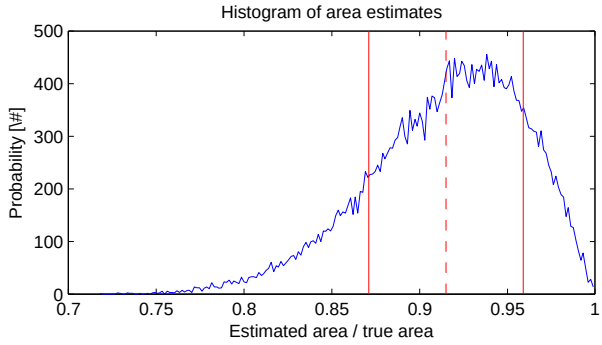

Figure E.7: Histogram of the outcome from 1000 simulations of an orifice fitting 3 beams. An unbiased estimator of the CSA has a mean value of 1. The dashed line indicates the mean value, and the solid vertical lines indicate the mean value $\pm$ 1 standard deviation.

measurement goes wrong. For large orifice sizes, the method underestimates the orifice size due to the stochastic nature of the Doppler signals and the way the calibration of the measurement is done based on the beam with most power. Fig. E.7 shows how the expected value of the reference beam is unbiased only when a single beam passes through the vena contracta. Typically less than 10 beams are candidates for selection as reference beams. From the figure, we can see that this corresponds to the reference beam being overestimated by up to 20 %. Because the power of the reference beam appears in the denominator of the CSA estimate in (E.12), the CSA estimate is increasingly underestimated for increasing orifice size as is seen in Fig. E.8. Omitting the stochastic variation makes the CSA estimate unbiased for orifice sizes larger than the beam width of the reference beam.

Prosthetic valves with 6 different orifices ranging from mild to severe mitral regurgitation were used in the flow phantom. It was not possible to include larger orifices

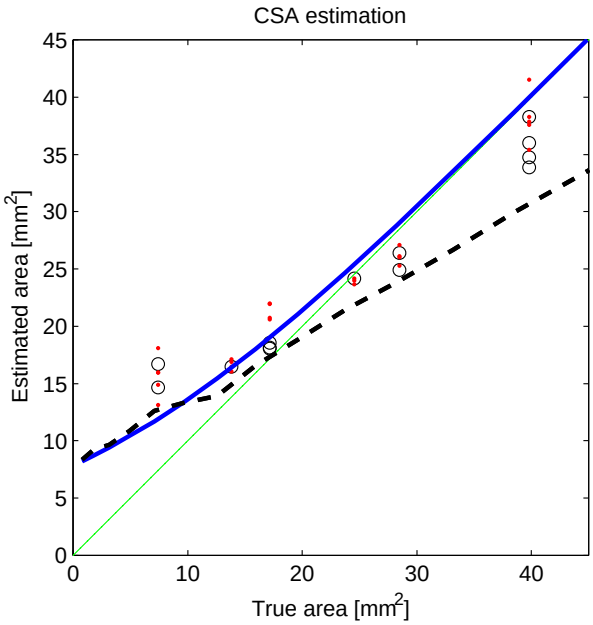

Figure E.8: Estimated CSA from both pulsatile and steady-state in vitro data, as well as simulated estimates. The dots (red) and circles (black) indicate the mean value from a measurement with pulsatile or steadystate flow, respectively. The dashed line shows the result from estimates based on the stochastic Doppler simulation, and the solid blue line shows the results of the deterministic simulations.

without destroying the valve. The in vitro CSA estimates shown in Fig. E.8 follow the same trend as the simulated results in the same figure, starting out with overestimation due to the too large reference beam area and ending with underestimation due to the increasing overestimation of the reference beam power. The data, however, are closer to the true value for large orifice sizes than the stochastic simulations predict, despite taking care to make the simulations as realistic as possible in terms of autocorrelation and smoothing. The offset might be caused by the omission of clutter in the simulated signals.

All orifices are nearly circular, even though clinically an orifice in a valve can have several different shapes. If the geometry of the orifice is known, the underestimation for large orifices can to some extent be compensated for.

The standard deviation of the in vitro CSA estimates is quite large. This is partly caused by the stochastic variation of the Doppler signal, where the situation for an orifice with 3 beams inside is shown in Fig. E.7. Additional smoothing will reduce this variation, but it might not be straightforward to implement. The vena contracta has a limited size, which means that if too much spatial smoothing is applied the estimates of the reference beam will be too low, causing an overestimation of the CSA. Additional

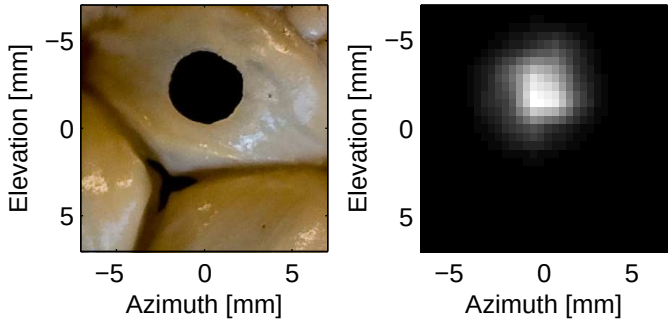

Figure E.9: Photography and power Doppler geometry estimate of an orifice with a 4.2mm diameter. The size of the two images is equal, and the colormap of the ultrasound image is linear, that is, is is not compressed logarithmically.

averaging in time is difficult due to the limited frame rate (typically 10 frames/sec) and because the vena contracta can move slightly from frame to frame due to the transient nature of a jet and movement of the operator.

The proposed method has a few inherent drawbacks, the most important of which is that the CSA estimate is based on a precalculated calibration factor. Ideally the full path of the beam must be known in detail to account for aberrations and nonlinearities, but this is not feasible in a clinical setting.

Further work

We also would like to validate the method for noncircular orifices and include measurement of flow rate, *e.g.*, with a transit-time flow meter. The method will also benefit a lot from development of better 3-D probes, where larger apertures with narrow beams should make the CSA estimation more accurate.

E.6 Conclusion

The proposed method is a promising new technique for the estimation of the cross-sectional area and geometry of regurgitant jets of moderate and severe orifice sizes, where the orifice is larger than the CSA of a single beam.

References

[1] M. Enriquez-Sarano, J. F. Avierinos, D. Messika-Zeitoun, D. Detaint, M. Capps, V. Nkomo, C. Scott, H. V. Schaff, and A. J. Tajik, "Quantitative determinants of the outcome of asymptomatic mitral regurgitation," *The New England Journal of Medicine*, vol. 352, pp. 875–883, Mar 2005.

[2] W. A. Zoghbi, M. Enriquez-Sarano, E. Foster, P. A. Grayburn, C. D. Kraft, R. A. Levine, P. Nihoyannopoulos, C. M. Otto, M. A. Quinones, H. Rakowski, W. J. Stewart, A. Waggoner, and N. J. Weissman, "Recommendations for evaluation of the severity of native valvular regurgitation with two-dimensional and doppler echocardiography," *Journal of the American Society of Echocardiography*, vol. 16, pp. 777–802, Jul 2003.

[3] P. Kahlert, B. Plicht, I. M. Schenk, R.-A. Janosi, R. Erbel, and T. Buck, "Direct assessment of size and shape of noncircular vena contracta area in functional versus organic mitral regurgitation using real-time three-dimensional echocardiography," *Journal of the American Society of Echocardiography*, vol. 21, pp. 912–921, Aug 2008.

[4] A. Vahanian, H. Baumgartner, J. Bax, E. Butchart, R. Dion, G. Filippatos, F. Flachskampf, R. Hall, B. Iung, J. Kasprzak, P. Nataf, P. Tornos, L. Torracca, and A. Wenink, "Guidelines on the management of valvular heart disease: The task force on the management of valvular heart disease of the european society of cardiology," *European Heart Journal*, vol. 28, pp. 230–268, Jan 2007.

[5] D. Khanna, S. Vengala, A. P. Miller, N. C. Nanda, S. G. Lloyd, S. Ahmed, A. Sinha, F. Mehmood, K. Bodiwala, S. Upendram, M. Gownder, H. S. Dod, A. Nunez, A. D. Pacifico, D. C. McGiffin, J. K. Kirklin, and V. K. Misra, "Quantification of mitral regurgitation by live three-dimensional transthoracic echocardiographic measurements of vena contracta area," *Echocardiography*, vol. 21, pp. 737–743, Nov 2004.

[6] L. Fang, M. C. Hsiung, A. P. Miller, N. C. Nanda, W. H. Yin, M. S. Young, D. E. Velayudhan, S. Rajdev, and V. Patel, "Assessment of aortic regurgitation by live three-dimensional transthoracic echocardiographic measurements of vena contracta area: usefulness and validation," *Echocardiography*, vol. 22, pp. 775–781, Oct 2005.

[7] D. E. Velayudhan, T. M. Brown, N. C. Nanda, V. Patel, A. P. Miller, F. Mehmood, S. Rajdev, L. Fang, E. E. Frans, S. Vengala, P. Madadi, P. Yelamanchili, and O. Baysan, "Quantification of tricuspid regurgitation by live three-dimensional transthoracic echocardiographic measurements of vena contracta area," *Echocardiography*, vol. 23, pp. 793–800, Oct 2006.

[8] S. H. Eik-Nes, K. Marsal, and K. Kristoffersen, "Methodology and basic problems related to blood flow studies in the human fetus," *Ultrasound in Medicine & Biology*, vol. 10, no. 3, pp. 329–337, 1984.

[9] P. N. Burns, "Measuring volume flow with doppler ultrasound - an old nut," *Ultrasound in obstetrics & gynecology*, vol. 2, no. 4, p. 238, 1992.

[10] B. A. J. Angelsen, "A theoretical study of the scattering of ultrasound from blood," *IEEE Transactions on Biomedical Engineering*, vol. 27, pp. 754–767, 1980.

[11] C. F. Hottinger and J. D. Meindl, "Blood flow measurement using the attenuation-compensated volume flowmeter," *Ultrasonic Imaging*, vol. 1, pp. 1–15, January 1979.

[12] T. Buck, R. A. Mucci, J. L. Guerrero, G. Holmvang, M. D. Handschumacher, and R. A. Levine, "The power-velocity integral at the vena contracta, a new method for direct quantification of regurgitant volume flow," *Circulation*, vol. 102, pp. 1053–1061, 2000.

[13] T. Buck, B. Plicht, P. Hunold, R. A. Mucci, R. Erbel, and R. A. Levine, "Broad-beam spectral doppler sonification of the vena contracta using matrix-array technology," *Journal of the American College of Cardiology*, vol. 45, 2005.

[14] T. Buck, R. A. Mucci, J. L. Guerrero, G. Holmvang, M. D. Handschumacher, and R. A. Levine, "Flow quantification in valvular heart disease based on the integral of backscattered acoustic power using doppler ultrasound," in *IEEE International Ultrasonics Symposium Proceedings*, March 2000.

[15] H. Torp, K. Kristoffersen, and B. A. J. Angelsen, "Autocorrelation techniques in color flow imaging: signal model and statistical properties of the autocorrelation estimates," *IEEE Transactions on Ultrasonics, Ferroelectrics and Frequency Control*, vol. 41, pp. 604–612, September 1994.

[16] A. C. of Cardiology, A. H. A. T. F. on Practice Guidelines (Writing Committee to revise the 1998 guidelines for the management of patients with valvular heart disease), S. of Cardiovascular Anesthesiologists, R. O. Bonow, B. A. Carabello, K. Chatterjee, A. C. de Leon, D. P. Faxon, M. D. Freed, W. H. Gaasch, B. W. Lytle, R. A. Nishimura, P. T. O'Gara, R. A. O'Rourke, C. M. Otto, P. M. Shah, J. S. Shanewise, S. C. Smith, A. K. Jacobs, C. D. Adams, J. L. Anderson, E. M. Antman, V. Fuster, J. L. Halperin, L. F. Hiratzka, S. A. Hunt, B. W. Lytle,

R. Nishimura, R. L. Page, and B. Riegel, "Acc/aha 2006 guidelines for the management of patients with valvular heart disease: a report of the american college of cardiology/american heart association task force on practice guidelines (writing committee to revise the 1998 guidelines for the management of patients with valvular heart disease) developed in collaboration with the society of cardiovascular anesthesiologists endorsed by the society for cardiovascular angiography and interventions and the society of thoracic surgeons," *Journal of the American College of Cardiology*, vol. 48, pp. e1–148, Aug 2006.

[17] K. V. Ramnarine, D. K. Nassiri, P. R. Hoskins, and J. Lubbers, "Validation of a new blood mimicking fluid for use in doppler flow test objects," *Ultrasound in Medicine & Biology*, vol. 24, pp. 451–459, March 1998.

[18] K. V. Ramnarine, P. R. Hoskins, H. F. Routh, and F. Davidson, "Doppler backscatter properties of a blood-mimicking fluid for doppler performance assessment," *Ultrasound in Medicine & Biology*, vol. 25, pp. 105–110, January 1999.

[19] H. Torp, "Clutter rejection filters in color flow imaging: a theoretical approach," *IEEE Transactions on Ultrasonics, Ferroelectrics, and Frequency Control*, vol. 44, pp. 417–424, March 1997.

[20] J. Jensen and N. B. Svendsen, "Calculation of pressure fields from arbitrarily shaped, apodized, and excited ultrasound transducers," *IEEE Transactions on Ultrasonics, Ferroelectrics, and Frequency Control*, vol. 39, pp. 262–267, 1992.

[21] T. Varslot and S.-E. Måsøy, "Forward propagation of acoustic pressure pulses in 3D soft biological tissue," *Modeling, Identification and Control*, vol. 27, no. 3, pp. 181–200, 2006.

Paper F

Quantification of Mitral Regurgitation using HPRF 3D Color Doppler

Thomas Renhult Skaug[1], Torbjørn Hergum[1], Brage Amundsen[1], Terje Skjærpe[2], Hans Torp[1] and Bjørn Olav Haugen[1]
[1]Department of Circulation and Medical Imaging, NTNU, Trondheim, Norway
[2]St. Olavs Hospital, Trondheim, Norway

Abstract

Background: A novel method to find the vena contract area (VCA) and quantify mitral regurgitation (MR) using multibeam high pulse repetition frequency Doppler (Muldo) is validated in vivo.

Methods: Twenty-seven patients with both organic and functional regurgitation were included. The Doppler signal was isolated from the mitral regurgitant jet using high pulse repetition frequency 3D color Doppler, where the Nyquist limit was set near the peak velocity of the jet. The VCA was found by summing the Doppler power from multiple beams within the vena contracta region, where the calibration was done with a reference beam within the jet. The regurgitant volume measured by Muldo (Muldo RV) was calculated as the product of VCA and the velocity-time-integral of the regurgitant jet as measured by CW Doppler. The regurgitant volume measured by magnetic resonance imaging (MRI RV) was calculated as the difference between the left ventricular and aortic stroke volume. In addition, evaluation of MR grade (1-4) and calculation of the regurgitant volume by the proximal isovelocity surface area method (Pisa RV) was done by 2D echocardiography.

Results: The correlation between MRI RV and Muldo RV (N=27), between MRI RV and Pisa RV (N=22) and between Pisa RV and Muldo RV were $r_s = 0.82$, $r_s = 0.78$ and $r_s = 0.63$, respectively. The 95% limits of agreement were $-3.0 \pm 26.2ml$, $4.7 \pm 30.6ml$ and $-9.7 \pm 37.0ml$, respectively.

Kappa agreement between 2D echo MR grade and Muldo RV was 0.44 and between 2D echo MR grade and MRI RV it was 0.48.

Conclusion: For moderate to severe regurgitation there was good agreement between MRI RV and Muldo RV. As expected, agreement was lower in mild regurgitation.

Submitted to *Circulation*

F.1 Introduction

According to American guidelines (ACC/AHA), surgery is indicated for severe mitral regurgitation (MR) when valve repair is possible, even in the absence of symptoms [1]. The echocardiographic assessment of severity is challenging, however, as it requires the integration of different two-dimensional semi-quantitative (2D) Doppler parameters with inherent strengths and weaknesses [2, 3]. The proximal isovelocity surface area (Pisa) method has several important limitations in that it assumes a circular regurgitant orifice and a flat valve plane [4].

A different approach to quantifying mitral regurgitation is to look at the vena contracta, which is slightly smaller than the anatomic orifice, and thus a measure of the effective regurgitant orifice area (EROA) [2]. Under both European and American guidelines, a vena contracta width (VCW) of $7mm$ or more and an EROA and regurgitant volume (RV) as measured by Pisa of $0.4cm^2$ and $60ml$ or more, respectively, are regarded as specific signs of severe MR [1, 5]. When the orifice is non-circular, a 2D measurement of the vena contracta and Pisa might lead to under or overestimation of the regurgitation [6, 7]. To avoid this, 3D color flow imaging (CFI) can be used to quantify the regurgitant jet area and jet volume [8, 9], the vena contracta area or cross-sectional area of the vena contracta (VCA) [10, 11] and Pisa [12]. Measuring the VCA by 3D CFI has shown better correlation with angiographic grading than the VCW measured by 2D CFI [10]. However, such direct color Doppler measurements are limited by low temporal and spatial resolution, high dependence on gain settings and limited separation of the core of the jet from the recruited slow flow around the jet.

In laminar blood flow with constant hematocrit, the backscattered Doppler power is proportional to the blood volume in the sample volume of an ultrasound beam [13]. This measurement can be calibrated to give an absolute measurement of volume, as was shown for measuring volume flow in arteries by Hottinger and Meindl in 1979 [14]. This principle can be used in the quantification of mitral regurgitation as shown by Buck et al., who measured the volume flow in the vena contracta by using a single wide measurement beam and a narrow reference beam [15]. We have recently extended this principle from using two beams along one dimension to using multiple beams in 3 dimensions [16]. This results in a more homogeneous measurement beam, which is the sum of all narrow beams, and provides information about the geometry of the jet. The purpose of this study was to validate this method by comparing it to standard 2D Doppler methods and to regurgitation volumes measured by magnetic resonance imaging, which has previously been validated for this purpose [17, 18].

F.2 Methods

F.2.1 Multibeam high pulse repetition frequency Doppler

The maximum velocity (the Nyquist velocity) that can be resolved with CFI is typically $1m/s$ for cardiac applications, which is much lower than the core velocities of $4-5m/s$ in an MR jet. Measuring the area of the central, high velocity parts of the jet requires

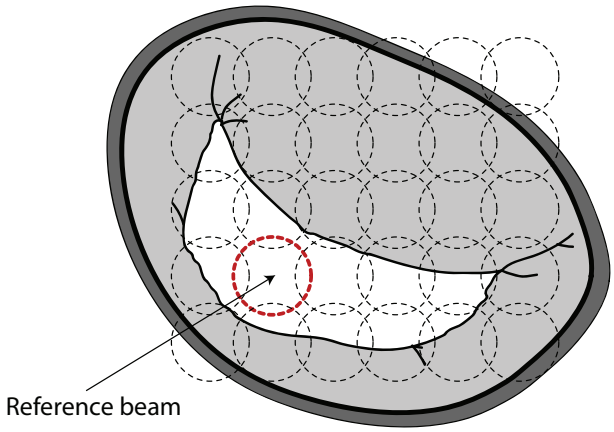

Figure F.1: Sketch of a leaking valve with multiple beams shown. The indicated reference beam is selected automatically as the beam that is most likely to be inside the orifice. The sum of the remaining beams is used as a composite measurement beam, as shown in Fig. F.2.

increasing the Nyquist velocity. We have done this by acquiring the data using a custom high pulse repetition frequency (HPRF) 3D color Doppler mode dubbed Muldo - Multibeam HPRF Doppler. In a HPRF modality, several pulses are fired before the deep echoes from the first pulse have returned to the probe, such that exact range information is lost. This means that velocity certitude is traded for range ambiguity. However, this is not a problem when the ultrasound beam only intersects one jet, because the Doppler signal originating from the spurious sample volumes is removed by a high pass filter.

Several ultrasound beams are spread out across the valve, as is shown in Fig. F.1. A composite measurement beam is made by summing the contribution from all the beams after clutter filtering. A computer simulation of the power of the individual beams (pink) comprising the composite measurement beam (red) and a wide, single measurement beam (blue) are shown to scale in Fig. F.2. The composite beam has a more homogeneous sensitivity and a higher signal-to-noise ratio (SNR) than the single, wide beam. The composite beam can be made arbitrarily large without losing SNR, although with a reduction in the frame rate.

The beam with the most power is selected as the reference beam, as this is the beam most likely to be completely covered by the regurgitant jet. In laminar blood flow, the power of the Doppler signal received from a sample volume is proportional to the blood volume within that sample volume. When the Doppler signal is filtered with a high-pass filter so that only signals from blood traveling above a given velocity remain, the Doppler power will be proportional to the volume of blood traveling above this speed. This involves using a sample volume that is very short in the radial direction to make sure that it only contains signals from the vena contracta, meaning that the Doppler power will be proportional to the VCA. The proportionality factor is calculated using

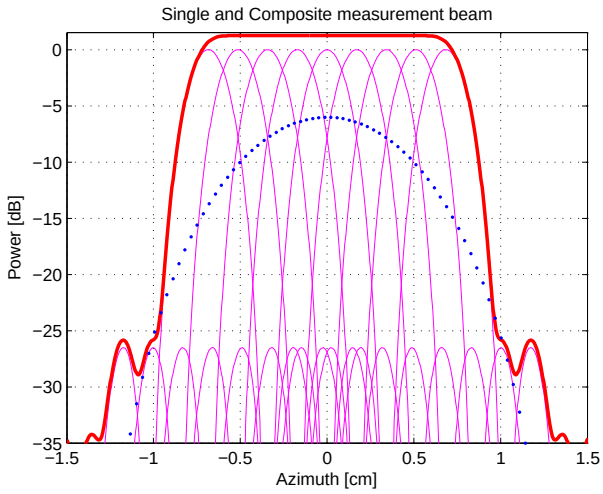

Figure F.2: A composite measurement beam is made by adding multiple narrow beams together. In this 2D sketch, 9 narrow beams have been added to make a wide, flat beam. The dashed line shows the beam profile of a single, wide beam from a smaller transducer. Notice that the peak sensitivity of this beam is approximately 8dB lower than for the composite beam, and that the sensitivity varies significantly.

the additional power measurement of the reference beam and a computer model of the ratio of the composite beam to the reference beam. This enables the calculation of the calibrated value of the VCA.

F.2.2 Data acquisition and processing

Equipment

A Vivid 7 Dimension (GE Vingmed Ultrasound, Horten, Norway) equipped with a 3V matrix array probe and an M4S 2D cardiac probe was used to acquire 3D HPRF Doppler and standard 2D images, respectively. An external computer with custom software was used for post-processing of the raw 3D Doppler data to calculate the VCA. EchoPac (GE Vingmed Ultrasound, Horten, Norway) was used to analyze the 2D images.

Subjects

This study was performed at the Department of Cardiology, University Hospital of Trondheim, Norway. The primary exclusion criteria were aortic regurgitation, atrial fibrillation or other arrythmia and those with contraindications for MRI. Of the thirty-five subjects with mild to severe mitral regurgitation (grade 1-4) who consented to participate, three of the subjects were excluded due to poor Muldo quality, four due

to poor MRI quality caused by arrhythmias during testing, and one due to renal failure requiring dialysis between the investigations. Consequently, the study was based on 27 subjects, 11 women and 16 men, with a median age of 51 years and a range from 28 to 81 years. Sixteen subjects had organic mitral disease or unidentified etiology and 11 had functional regurgitation. All were in sinus rhythm, and the median ejection fraction measured by echocardiography was 50% with a range of 23% to 65%. The median interval between the echocardiographic and MRI examination was 0 days with a range of 0 to 5 days. The study was approved by the Regional Committee for Medical Research Ethics (REK), Norwegian Social Science Data Service and conducted according to the Helsinki Declaration. The volunteers gave written informed consent to participate.

2D echocardiography

A standard 2D echocardiography (2D echo) examination was performed, including an assessment of the jet area by CFI compared to left atrial size and mitral and pulmonary vein flow. The maximal velocity and the velocity time integral (VTI) of the regurgitant jet were measured by continuous wave (CW) Doppler. The mitral regurgitant flow rate by Pisa was measured with a Nyquist limit of about $40cm/s$, and the RV was calculated (Pisa RV). We were unable to assess the Pisa flow rate in five subjects. A highly qualified echo-observer, blinded for the MRI and Muldo results, analyzed Pisa measurements and mitral regurgitation grade (2D echo MR grade) as 1=mild, 2=mild to moderate, 3=moderate to severe and 4=severe [2].

Muldo

Muldo recordings were made in the apical view in two steps, as illustrated in Fig. F.3. With the scanner in triplex-mode (B-mode, CFI, and PW-Doppler), the vena contracta was located by moving the PW sample volume into the jet flow shown by CFI, and adjusted to include the highest velocities. The scanner was then switched to a custom HPRF 3D color Doppler mode, with the position of the 3D sample volume centered around the PW sample volume. One recording consisted of data from up to 15 heart cycles. The procedure was repeated several times to make sure that the vena contracta was within the 3D sample volume despite patient movements. Currently the acquisition speed is limited to about 10 volumes per second. The raw 3D Doppler data was analyzed with custom software developed using Matlab (The Mathworks, Natick, MA). Radial smoothing was applied to reduce the variance of the estimates. The estimate of the VCA (Muldo VCA) was the median value of all the measurements. Frames corresponding to the systolic jet were selected. Some frames were excluded according to the following criteria:

- No visible jet above noise level
- The region of interest (ROI) did not cover the jet area
- The smallest jet area was found to be on the top or bottom depth of the ROI, suggesting that the vena contracta could be above or below the ROI

Muldo was analyzed by an observer blinded for the MRI data and the 2D echo MR grade results. To assess interobserver variability, another blinded observer analyzed 18 of the subjects. The regurgitant volume (Muldo RV) was calculated as the product of Muldo VCA and the VTI of the regurgitant jet measured by CW Doppler. In addition to estimating the VCA, Muldo also provided an estimate of the geometry of the orifice, which was not used further in this study.

MRI Study

All patients were examined during supine rest using a Siemens Avanto 1.5 T system with a body matrix coil (Siemens, Erlangen, Germany). TrueFISP cine images were acquired during end-expiratory breath holds in the 4- and 2-chamber views, and in short-axis from the base to the apex of the left ventricle with the following settings: retrospective ECG-gating, in-plane resolution 0.9 x 0.9 mm, echo time 1.12 ms, repetition time 58 ms, flip angle 80°, slice thickness 6 mm with 4 mm gap and 25-30 frames/beat. Flow in the ascending aorta was quantified using an SSFP phase-contrast sequence with the following settings: retrospective ECG-gating, inplane resolution 1.3 x 1.3 mm, minimal TR (61.05ms) and TE (3.09ms), slice thickness 6 mm, VENC adjusted to just above maximal systolic velocities, 25-30 frames/beat. All images were analysed in Segment (http://segment.heiberg.se) [19], by an observer unaware of the echocardiographic results. The LV stroke volume was calculated by semi-automatically drawing endocardial contours in the short-axis images in end-diastole and -systole (aortic valve closure). Systolic long-axis excursion was quantified by measuring the descent of the septal, lateral, inferior and anterior points of the mitral annulus in the 4- and 2-chamber views. The average value was incorporated into the stroke volume estimate in the software. Systolic flow in the ascending aorta was quantified from the phase-contrast images by drawing a region of interest in the ascending aorta. Quantification of the mitral regurgitant volume (MRI RV) was done by the formula:

MRI RV = Stroke volume (left ventricle) - Stroke volume (aorta)

The accuracy of the method was tested in an in vivo validation study where the same measurements as described above were done in 10 subjects (4 healthy subjects, 6 with a recent myocardial infarction) where the absence of a mitral regurgitation was confirmed by echocardiography by an experienced sonographer. The estimated error was $3 \pm 5ml$ per stroke.

Statistics

The null hypothesis corresponds to no difference between the Muldo, MRI and 2D echo in the quantification of MR. Including 27 patients gives a power $> 90\%$ at the 5 % significance level for detecting a difference in regurgitation volume of 5 ml, assuming 1 standard deviation (σ) of 3.2 ml. Spearman rank correlation was used because the continuous variables were not normally distributed. Agreement between the continuous variables (Muldo RV, MRI RV, Pisa RV) was assessed by calculating the 95% limits of agreement (mean difference $\mu \pm 2\sigma$) [20]. To assess the agreement between 2D echo MR grade (1-4), Muldo RV ($ml/beat$), Muldo VCA (mm^2) and MRI

RV ($ml/beat$), we used kappa statistics. In accordance with current guidelines, we divided the Muldo VCA results into four categories: 1=0-19 mm^2; 2=20-29 mm^2; 3=30-39mm^2; 4 > 40mm^2. Muldo RV and MRI RV were divided into four categories: 1=0-29ml; 2=30-44ml; 3=45-59ml; 4 > 60ml [2]. We assessed kappa agreement between 2D echo MR grade and Muldo RV and MRI RV respectively for both organic and functional MR. Because the differences were normally distributed, we used paired samples t-tests to compare the heart rate during Muldo and MRI. We compared MRI RV and Muldo RV in subgroups with MRI RV less than and more than 30ml, and the mean difference between MRI RV and Muldo RV in both those with organic and those with functional regurgitation. We assessed the interobserver variability of the Muldo VCA in 18 subjects as the coefficient of repeatability, defined as two standard deviations (2σ) of the differences, and the interobserver repeatability of Muldo RV was calculated.

Descriptive values are reported as median and range, and 95% limits of agreement are reported as $\mu \pm 2\sigma$. The statistical analyses were performed in SPSS (SPSS Inc., Chicago, Illinois)

F.3 Results

The descriptive results of all methods are presented in Table F.1 table 1. There was no significant difference between heart rate during the Muldo and MRI recordings, with a mean difference of 2.4 beats/min (95% CI -1.2, 6.0).

The correlation between MRI RV and Muldo RV was $r_s = 0.82$, $p < 0.001$, and the 95% limits of agreement were $-3.0 \pm 26.2ml$. The correlation between MRI RV and Pisa RV was $r_s = 0.78$, $p < 0.001$, and the 95% limits of agreement were $4.7 \pm 30.6ml$. The correlation between Pisa RV and Muldo RV was $r_s = 0.63$, $p = 0.002$, and the 95% limits of agreement were $-9.7 \pm 37.0ml$. The agreement between the different methods is shown in Figs. F.4 – F.6. There was no significant difference between MRI RV and Muldo RV, or between MRI RV and Pisa RV, while Pisa RV was significantly lower than Muldo RV.

The correlation and kappa agreement between the different methods describing mitral regurgitation severity are presented in Tables F.2 and F.3 and in Fig. F.7. Agreement between the various methods was better for organic than functional mitral regurgitation, as seen in Table F.3.

There was a significant difference between MRI RV and Muldo RV in patients with mild mitral regurgitation as defined by MRI RV < 30ml (N=12) with a mean difference of -11.8 ml and 95%CI (-17.9, -5.6). In patients with moderate and severe regurgitation defined by MRI RV > 30ml (N=15), there was no significant difference, with a mean difference of 5.2 ml and 95%CI (-0.6, 10.0). The mean differences between MRI RV and Muldo RV in organic and functional mitral regurgitation were 1.1ml and 95%CI (-5.7, 7.9) and -8.8 ml and 95% CI (-16.8, -0.8), respectively.

Interobserver analysis of the Muldo VCA in 18 subjects demonstrated that the coefficient of repeatability was 8.6 mm2. Due to the interobserver variability with Muldo VCA, the coefficient of repeatability for Muldo RV was 9.8 ml.

Descriptives	median	range
Muldo VCA (N=27)	$25.7mm^2$	$12.0 - 59.0mm^2$
VTI by CW Doppler (N=27)	$150cm$	$74 - 213cm$
Peak jet vel. by CW Dop. (N=27)	$5.3m/s$	$4.3 - 6.3m/s$
Muldo RV (N=27)	$35.6ml$	$14.2 - 99ml$
Muldo RV in funct. MR (N=11)	$32.3ml$	$14 - 54.2ml$
Muldo RV in org. MR (N=16)	$39.8ml$	$14.2 - 99ml$
MRI RV (N=27)	$35.1ml$	$4.2 - 129ml$
MRI RV in funct. MR (N=11)	$14.3ml$	$7.8 - 46.3ml$
MRI RV in org. MR (N=16)	$47.1ml$	$4 - 129ml$
Pisa RV (N=22)	$22.2ml$	$2.2 - 80ml$
Heart rate during MRI (N=27)	$64.0/min$	$48 - 110/min$
Heart rate during echo/Muldo (N=27)	$63.0/min$	$43 - 104/min$

Table F.1: Study results

Descriptives	r_s	p
MRI RV vs Muldo VCA (N=27)	0.64	<0.001
MRI RV vs. Muldo RV (N=27)	0.82	<0.001
MRI RV vs. Pisa RV (N=22)	0.78	<0.001
Pisa RV vs. Muldo RV (N=22)	0.63	0.002
2D echo vs. Muldo VCA (N=27)	0.41	0.036
2D echo vs. Muldo RV (N=27)	0.66	<0.001
2D echo vs. MRI RV (N=27)	0.82	<0.001
2D echo vs Pisa RV (N=22)	0.74	<0.001

Table F.2: Correlations. r_s is calculated using Spearman's statistics.

2D Echo MR grade	kappa	p
MRI RV vs Muldo VCA (N=27)	0.32	0.005
MRI RV vs Muldo RV (N=27)	0.49	<0.001
2D echo vs Muldo VCA (N=27)	0.12	0.30
2D echo vs Muldo RV (N=27)	0.44	<0.001
2D echo vs MRI RV (N=27)	0.48	<0.001
MRI RV vs Muldo RV, funct. (N=11)	0.11	0.60
2D echo vs Muldo RV, funct. (N=11)	0.19	0.36
2D echo vs MRI RV, funct. (N=11)	0.30	0.12
MRI RV vs Muldo RV, org. (N=16)	0.67	<0.001
2D echo vs Muldo RV, org.(N=16)	0.58	<0.001
2D echo vs MRI RV, org. (N=16)	0.57	<0.001

Table F.3: Kappa agreement. Muldo VCA: 1=0-19mm^2; 2=20-29mm^2; 3=30-39mm^2; 4 > 40mm^2. Muldo RV and MRI RV: 1=0-29ml; 2=30-44ml; 3=45-59ml; 4 > 60ml.

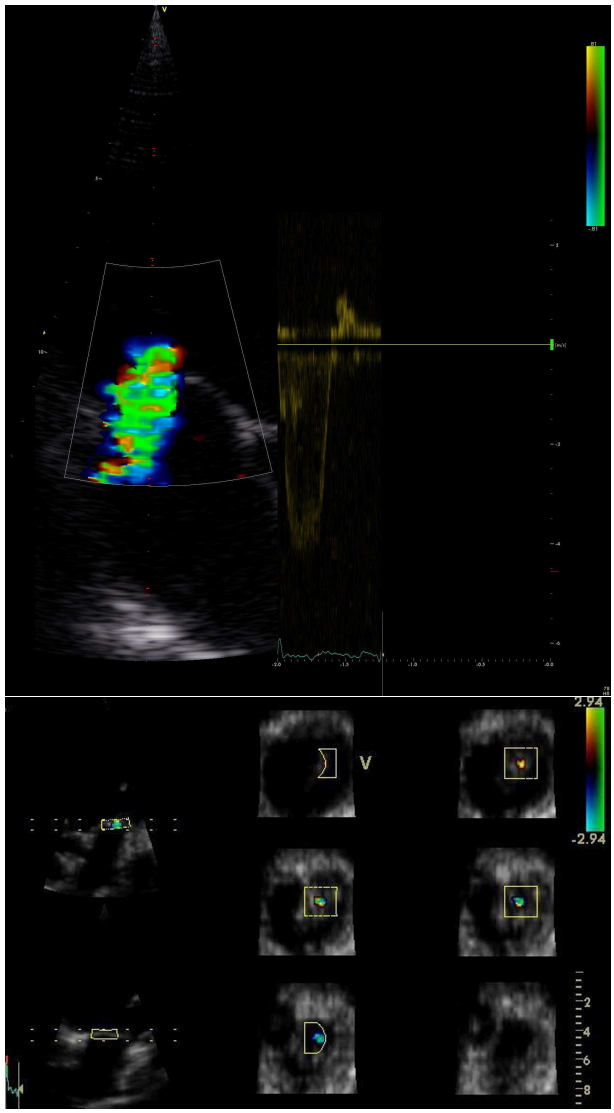

Figure F.3: Two-step Muldo data acquisition. Top: Triplex scan. Bottom: 3D HPRF Color flow. Note the Nyquist limit (2.94m/s) and the small ROI (radial depth 7mm and lateral extension 20 mm).

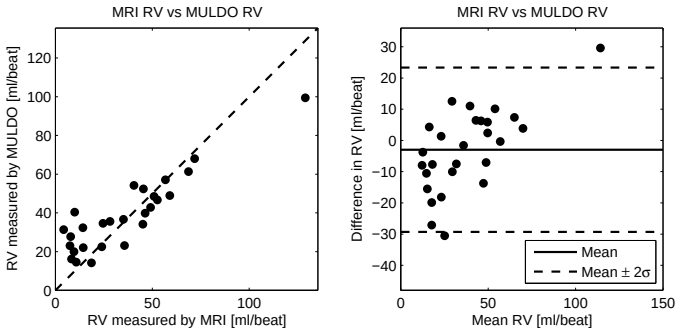

Figure F.4: The correlation between MRI RV and Muldo RV was $r_s = 0.82$, $p < 0.001$. The 95% limits of agreement between MRI RV and Muldo RV were $-3.0 \pm 26.2ml$. $N = 27$.

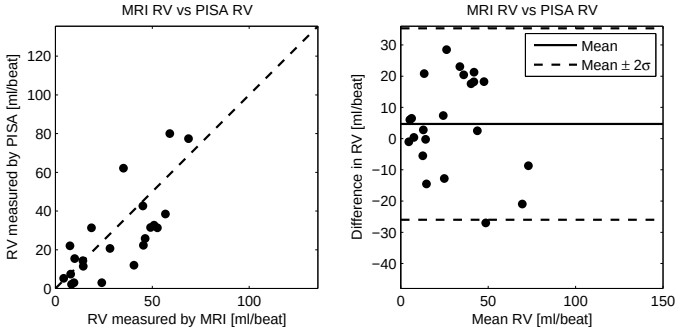

Figure F.5: The correlation between MRI RV and Pisa RV was $r_s = 0.78$, $p < 0.001$. The 95% limits of agreement between MRI RV and Pisa RV were $4.7 \pm 30.6ml$. $N = 22$.

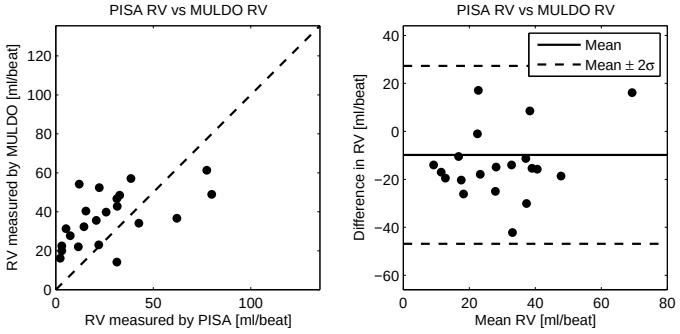

Figure F.6: Correlation between Pisa RV and Muldo RV was $r_s = 0.63$, $p = 0.002$. The 95% limits of agreement between Pisa RV and Muldo RV were $-9.7 \pm -37.0ml$. $N = 22$.

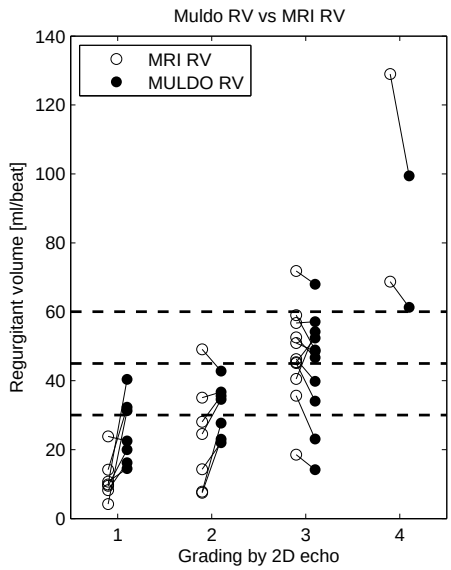

Figure F.7: Agreement between 2D echo MR grade and Muldo RV, kappa=0.44 and $p < 0.001$, and between 2D echo MR grade and MRI RV, kappa=0.48, $p < 0.001$. Agreement between MRI RV and Muldo RV, kappa=0.49 and $p < 0.001$. Muldo RV and MRI RV categories: 1=0-29ml; 2=30-44ml; 3=45-59ml and $4 > 60ml$.

F.4 Discussion

The present study shows that the severity of mitral regurgitation can be quantified with a new 3D echocardiographic method based on multibeam high pulse repetition frequency Doppler (Muldo). The method is an extension of previous one-dimensional methods, and has the potential to quantify both the area and shape of the vena contracta. In patients with more than a mild regurgitant jet evaluated by a standard 2D Doppler examination it is necessary to quantify of the regurgitant volume to discriminate between the moderate and severe MR [2].

Agreement between MRI RV and Muldo RV and between 2D echo MR grade and Muldo RV was moderately good. In organic mitral regurgitation, agreement between the methods was even better, and there was no significant difference between MRI RV and Muldo RV. Agreement was poor in functional mitral regurgitation, with the Muldo RV being significantly higher. Similarly, in patients with MRI RV $< 30ml$ there was significant overestimation by Muldo RV, but there was no significant difference between MRI RV and Muldo RV in those with MRI RV $> 30ml$. The 95% limits of agreement were wide between the MRI RV and Muldo RV and are partly explained by the significant overestimation of mild regurgitation by Muldo.

Because Muldo estimates the VCA based on a calibrated measurement of the backscattered Doppler power and requires no manual tracing, the calculations can be done semi-automatically. Furthermore, the calculations are not affected by gain settings or color blooming. The major advantages of extending the method to three dimensions are a more homogeneous sensitivity of the measurement beam, which ensures that a slight shift of the ROI will not result in a different measurement. The signal-to-noise ratio is also improved. Since the reference beam is automatically selected from the grid of beams, it is easier for the sonographer to obtain a reference measurement, compared to if only a single reference beam is used. Additionally, Muldo uses a 3D color flow Doppler acquisition with a high Nyquist limit ,which makes it possible to visualize the geometry of the high-velocity core of the vena contracta. This is not possible with standard color flow imaging. Although we were not able to fully resolve the maximal jet velocities, the core of the jet can be extracted with filtering as long as the peak velocity is less than two times the Nyquist aliasing velocity.

To achieve a high PRF, and thus a high Nyquist limit, the ROI must be small in the radial direction. Consequently, it can be challenging to position the ROI correctly, especially with large displacements of the mitral valve as is found in hyperdynamic ventricles or in severe regurgitation. As shown in the experimental study [16] Muldo will overestimate the size of the regurgitation in mild disease when the orifice is narrow relative to the size of the reference beam. This limitation is inherent to all similar techniques requiring a reference measurement [21]. Accordingly, agreement was better for the moderate and severe regurgitation in the present study. Area estimation by Muldo is angle dependent, like other Doppler methods, and misalignment will overestimate the VCA. However, the regurgitant volume will be angle independent as this overestimation will be exactly cancelled out by underestimation of the VTI from CW Doppler in the jet core.

The criteria for inclusion and exclusion of frames were well defined, but there

were still some frames that were of uncertain nature, which explains the interobserver variability of Muldo VCA.

Correct quantification of the VTI is essential for measuring the regurgitant volume. This can be difficult if the CW signal has variable density, either due to motion of the jet core, or variation of the regurgitant volume during systole [2, 22]. For a short-duration regurgitation, the current frame rate of 10Hz is probably too low, but this can be expected to improve with technical development. To reduce this kind of error, Muldo acquires data over 10-15 cardiac cycles.

In the present study we found better correlation and agreement between Muldo RV and MRI RV than between Muldo VCA and MRI RV. This is not surprising, as the regurgitant volume is not only given by the EROA, but also by the duration of the regurgitation and the pressure gradient across the mitral valve. MRI is the best non-invasive reference method available for quantification of mitral regurgitation, and the in vivo validation results show that the MRI measurements only contributed to a modest part of the total difference between the methods.

As demonstrated in Fig. F.4 the 95% limits of agreement between MRI RV and Muldo RV were wide in our study, while Buck et al demonstrated excellent agreement. They reported a mean difference of $0.4ml$ and $\sigma = 3.2ml$, corresponding to 95% limits of agreement $0.4 \pm 6.4ml$ between broad beam spectral Doppler and MRI measurements of mitral regurgitant volume up to $40ml$. There are some differences to note. Our population was characterized by a wider range of regurgitant volumes measured by MRI (4 – $129ml$) than in the population investigated by Buck et al. (6 – $46ml$). Secondly, the calculation of MRI RV was somewhat different, as we calculated the LV stroke volume by volumetric measurements in short and long axis images, while Buck et al measured mitral inflow by phase contrast imaging [21]. There is also an expected overestimation of the Muldo VCA in mild regurgitation as shown in vitro [16]. We demonstrated significant overestimation by Muldo for mild regurgitation as defined by MRI RV $< 30ml$, but no significant bias for MRI RV$> 30ml$. However, MRI is a reference method and not a gold standard, and the calculation of MRI RV relies on several measurements with inherent variability (systolic + diastolic volumes and aortic outflow) in the same way as Muldo RV relies on measuring both Muldo VCA and VTI accurately.

We found significant correlation ($r_s = 0.66$) and moderately good agreement (kappa=0.44, $p < 0.001$) between 2D echo MR grade and Muldo RV. The fact that Muldo overestimates mild regurgitation ($RV < 30ml$) is clearly illustrated in Fig. F.7. This contributes to some overlap between MR grade 1 and 2. It is noteworthy that the Kappa agreement between 2D echo MR grade and MRI RV was comparably good (kappa=0.48).

We demonstrated better agreement between 2D echo MR grade and Muldo RV and between MRI RV and Muldo RV for organic than for functional mitral regurgitation. This probably stems from the same source as the overestimation of mild regurgitation - that the reference beams are too large for some orifices. The regurgitant orifice is usually asymmetric and non-circular in functional as opposed to organic mitral regurgitation [7], meaning that the cross-sectional area may be large, but still not able to encompass the full reference beam. Additionally, those with an organic etiology in

our study were part of a higher RV population than those with a functional etiology.

Pisa is a standard method for quantifying the regurgitant volume, but it assumes a circular defect and hemispheric proximal flow convergence area [2, 4]. In our study, 2D Pisa was feasible in 22 out of 27 patients. The 95% limits of agreement between MRI RV and Pisa RV (Fig. F.5) were wider than between MRI RV and Muldo RV (Fig. F.4).

In 3D CFI studies it has been demonstrated that the proximal flow convergence area is hemielliptic rather than hemispheric, leading to significant underestimation of the EROA measured by 2D CFI compared to 3D CFI [23]. In functional as opposed to organic mitral regurgitation, the EROA is underestimated by 2D Pisa due to asymmetric geometry of the EROA [12]. We demonstrated that the 95% limits of agreement between Pisa RV and Muldo RV were wide (Fig. F.6). Muldo RV was significantly larger than Pisa RV. Similarly, the VCA measured by 3D CFI has been demonstrated to be significantly larger than the EROA measured by 2D Pisa, especially in patients with elliptical orifice shapes. The 95% limits of agreement were quite wide, and there was a significant bias with increasing differences between the methods with increasing EROA averages [24].

We expect the next generation of 3D probes to increase the aperture size to match the currently available 2D probes. This will enable narrower reference beams, meaning that Muldo will be able to measure smaller orifices and narrower asymmetric functional mitral regurgitation without a bias. The current, low frame rate of 10Hz is also expected to increase significantly with the application of parallel receive beams.

F.5 Conclusion

For the quantification of mitral regurgitation, our recently introduced method Muldo overcomes several of the limitations of color flow imaging as well as the assumptions made by Pisa that lead to underestimation of non-circular defects. However, Muldo significantly overestimated mild regurgitation, but these are usually identified easily by standard 2D Doppler examinations, making further quantitative efforts unnecessary. There was no significant bias for moderate and severe mitral regurgitation when Muldo was compared to magnetic resonance imaging.

We believe that regurgitant volume measured by Muldo can supplement 2D Doppler for the quantification of moderate and severe mitral regurgitation.

References

[1] A. C. of Cardiology, A. H. A. T. F. on Practice Guidelines (Writing Committee to revise the 1998 guidelines for the management of patients with valvular heart disease), S. of Cardiovascular Anesthesiologists, R. O. Bonow, B. A. Carabello, K. Chatterjee, A. C. de Leon, D. P. Faxon, M. D. Freed, W. H. Gaasch, B. W. Lytle, R. A. Nishimura, P. T. O'Gara, R. A. O'Rourke, C. M. Otto, P. M. Shah, J. S. Shanewise, S. C. Smith, A. K. Jacobs, C. D. Adams, J. L. Anderson, E. M. Antman, V. Fuster, J. L. Halperin, L. F. Hiratzka, S. A. Hunt, B. W. Lytle, R. Nishimura, R. L. Page, and B. Riegel, "Acc/aha 2006 guidelines for the management of patients with valvular heart disease: a report of the american college of cardiology/american heart association task force on practice guidelines (writing committee to revise the 1998 guidelines for the management of patients with valvular heart disease) developed in collaboration with the society of cardiovascular anesthesiologists endorsed by the society for cardiovascular angiography and interventions and the society of thoracic surgeons," *Journal of the American College of Cardiology*, vol. 48, pp. e1–148, Aug 2006.

[2] W. A. Zoghbi, M. Enriquez-Sarano, E. Foster, P. A. Grayburn, C. D. Kraft, R. A. Levine, P. Nihoyannopoulos, C. M. Otto, M. A. Quinones, H. Rakowski, W. J. Stewart, A. Waggoner, and N. J. Weissman, "Recommendations for evaluation of the severity of native valvular regurgitation with two-dimensional and doppler echocardiography," *Journal of the American Society of Echocardiography*, vol. 16, pp. 777–802, Jul 2003.

[3] M. Enriquez-Sarano, C. W. Akins, and A. Vahanian, "Mitral regurgitation," *The Lancet*, vol. 373, no. 9672, pp. 1382–1394, 2009.

[4] I. A. Simpson, T. Shiota, M. Gharib, and D. J. Sahn, "Current status of flow convergence for clinical applications: Is it a leaning tower of "PISA"?," *Journal of the American College of Cardiology*, vol. 27, no. 2, pp. 504–509, 1996.

[5] A. Vahanian, H. Baumgartner, J. Bax, E. Butchart, R. Dion, G. Filippatos, F. Flachskampf, R. Hall, B. Iung, J. Kasprzak, P. Nataf, P. Tornos, L. Torracca, and A. Wenink, "Guidelines on the management of valvular heart disease: The task force on the management of valvular heart disease of the european society of cardiology," *European Heart Journal*, vol. 28, pp. 230–268, Jan 2007.

[6] B. J. Roberts and P. A. Grayburn, "Color flow imaging of the vena contracta in mitral regurgitation: technical considerations," *Journal of the American Society of Echocardiography*, vol. 16, pp. 1002–1006, September 2003.

[7] P. Kahlert, B. Plicht, I. M. Schenk, R.-A. Janosi, R. Erbel, and T. Buck, "Direct assessment of size and shape of noncircular vena contracta area in functional versus organic mitral regurgitation using real-time three-dimensional echocardiography," *Journal of the American Society of Echocardiography*, vol. 21, pp. 912–921, Aug 2008.

[8] L. Sugeng, L. Weinert, and R. M. Lang, "Real-time 3-Dimensional color doppler flow of mitral and tricuspid regurgitation: Feasibility and initial quantitative comparison with 2-Dimensional methods," *Journal of the American Society of Echocardiography*, vol. 20, pp. 1050–1057, Sept. 2007.

[9] R. D. Simone, G. Glombitza, C. F. Vahl, J. Albers, H. P. Meinzer, and S. Hagl, "Three-dimensional color doppler: a clinical study in patients with mitral regurgitation," *Journal of the American College of Cardiology*, vol. 33, no. 6, pp. 1646–1654, 1999.

[10] D. Khanna, S. Vengala, A. P. Miller, N. C. Nanda, S. G. Lloyd, S. Ahmed, A. Sinha, F. Mehmood, K. Bodiwala, S. Upendram, M. Gownder, H. S. Dod, A. Nunez, A. D. Pacifico, D. C. McGiffin, J. K. Kirklin, and V. K. Misra, "Quantification of mitral regurgitation by live three-dimensional transthoracic echocardiographic measurements of vena contracta area," *Echocardiography - Jnl Cardiovascular Ultrasound & Allied Techniques*, vol. 21, pp. 737–743(7), November 2004.

[11] S. H. Little, B. Pirat, R. Kumar, S. R. Igo, M. McCulloch, C. J. Hartley, J. Xu, and W. A. Zoghbi, "Three-Dimensional color doppler echocardiography for direct measurement of vena contracta area in mitral regurgitation: In vitro validation and clinical experience," *JACC: Cardiovascular Imaging*, vol. 1, no. 6, pp. 695–704, 2008.

[12] Y. Matsumura, G. Saracino, K. Sugioka, H. Tran, N. L. Greenberg, N. Wada, M. Toyono, S. Fukuda, T. Hozumi, and J. D. Thomas, "Determination of regurgitant orifice area with the use of a new Three-Dimensional flow convergence geometric assumption in functional mitral regurgitation," *Journal of the American Society of Echocardiography*, vol. 21, no. 11, pp. 1251–1256, 2008.

[13] B. A. J. Angelsen, "A theoretical study of the scattering of ultrasound from blood," *IEEE Transactions on Biomedical Engineering*, vol. 27, pp. 754–767, 1980.

[14] C. F. Hottinger and J. D. Meindl, "Blood flow measurement using the attenuation-compensated volume flowmeter," *Ultrasonic Imaging*, vol. 1, pp. 1–15, January 1979.

[15] T. Buck, R. A. Mucci, J. L. Guerrero, G. Holmvang, M. D. Handschumacher, and R. A. Levine, "The power-velocity integral at the vena contracta, a new method for direct quantification of regurgitant volume flow," *Circulation*, vol. 102, pp. 1053–1061, 2000.

[16] T. Hergum, T. R. skaug, K. Matre, and H. Torp, "Quantification of valvular regurgitation area and geometry using hprf 3-d doppler," *IEEE Transactions on Ultrasonics, Ferroelectrics and Frequency Control*, vol. 56, pp. 975–82, May 2009.

[17] E. V. Gelfand, S. Hughes, T. H. Hauser, S. B. Yeon, L. Goepfert, K. V. Kissinger, N. M. Rofsky, and W. J. Manning, "Severity of mitral and aortic regurgitation as assessed by cardiovascular magnetic resonance: optimizing correlation with doppler echocardiography," *Journal of Cardiovascular Magnetic Resonance*, vol. 8, no. 3, pp. 503–507, 2006.

[18] W. G. Hundley, H. F. Li, J. E. Willard, C. Landau, R. A. Lange, B. M. Meshack, L. D. Hillis, and R. M. Peshock, "Magnetic resonance imaging assessment of the severity of mitral regurgitation comparison with invasive techniques," *Circulation*, vol. 92, no. 5, pp. 1151–1158, 1995.

[19] E. Heiberg, K. Markenroth, and H. Arheden, "Validation of free software for automated vessel delineation and mri flow analysis," *Journal of Cardiovascular Magnetic Resonance*, vol. 9, no. 2, pp. 375–376, 2007.

[20] J. M. Bland and D. G. Altman, "Statistical methods for assessing agreement between two methods of clinical measurement," *Lancet*, vol. 1, no. 8476, pp. 307–310, 1986.

[21] T. Buck, B. Plicht, P. Hunold, R. A. Mucci, R. Erbel, and R. A. Levine, "Broad-beam spectral doppler sonification of the vena contracta using matrix-array technology," *Journal of the American College of Cardiology*, vol. 45, 2005.

[22] A. M. Kizilbash, D. L. Willett, M. E. Brickner, S. K. Heinle, and P. A. Grayburn, "Effects of afterload reduction on vena contracta width in mitral regurgitation," *Journal of the American College of Cardiology*, vol. 32, pp. 427–431, Aug. 1998.

[23] C. Yosefy, R. Levine, J. Solis, M. Vaturi, M. Handschumacher, and J. Hung, "Proximal flow convergence region as assessed by real-time 3-dimensional echocardiography: Challenging the hemispheric assumption," *Journal of the American Society of Echocardiography*, vol. 20, no. 4, pp. 389–96, 2007.

[24] K. Iwakura, H. Ito, S. Kawano, A. Okamura, T. Kurotobi, M. Date, K. Inoue, and K. Fujii, "Comparison of orifice area by transthoracic three-dimensional doppler echocardiography versus proximal isovelocity surface area (PISA) method for assessment of mitral regurgitation," *The American journal of cardiology*, vol. 97, no. 11, pp. 1630–1637, 2006.